Microfluidics for Particle Manipulation: New Simulation Techniques for Novel Devices and Applications

Chao Wang

Hertford College

Department of Engineering Science

University of Oxford

Thesis submitted for the degree of

Doctor of Philosophy

Hilary Term, 2013

"**Microfluidics for Particle Manipulation: New Simulation Techniques for Novel Devices and Applications**"

Thesis submitted for the degree of Doctor of Philosophy

Chao Wang
Hertford College, University of Oxford

Hilary Term, 2013

Abstract

This thesis focuses on fundamental aspects of microfluidic systems and applies relevant findings to innovative designs for advanced particle manipulation applications.

Computational Fluid Dynamics (CFD) is adopted for fluid modeling, based on the Finite Volume method. The accuracy of the solutions obtained is confirmed by grid sensitivity analysis and by comparisons with experimental work. Curved microchannel features and the induced Dean flow are studied through a parametric space exploration and simulations. The Lagrange-Euler coupling method – Surface Marker Point methodology – is applied to simulate large-size particles (of comparable size to the channel). Through this simulation approach, all the forces on such particles are directly derived through solving the governing equations and the influence of these particles on the flow is considered in a fully coupled manner. A new approach – the Frozen Flow & Flow Correction Coefficient method – is developed, making trans-relaxation-time simulations possible and improving computational efficiency significantly, for 3D simulations of arbitrary shape and size microparticles in complicated microfluidic channels. Detailed comparisons between simulation results and experiments involving particle sedimentation and particle equilibrium position have been conducted for methodology validation.

Mechanisms of hydrodynamic particle manipulation are then studied, including hydrodynamic focusing and separation. It is found that the Tubular Pinch effect, Dean flow and the Radial Pressure Gradient effect interact to yield two distinct particle separation mechanisms. For advanced applications, particle focusing, non-magnetic and magnetic separation for neutrally buoyant particles are proposed, based on newly gained insight on the above-mentioned mechanisms. Appropriate channel designs have been proposed both for particle focusing and size-based particle separation, while the vertical-magnetic-Dean separation scheme is highlighted for magnetic separation.

Finally, a new integrated system is proposed, that combines the above novel designs into a device-like ensemble. It promises to offer functionality for biomaterial separation and detection, including different types of cells, antigens and biomarkers.

Acknowledgements

This thesis owes a great deal to the support and encouragement of many people, without whom it would never have materialized.

In particular, I would like to express my gratitude to my supervisor Prof. Yiannis Ventikos for accepting me as a research student and for three and a half years of inspiring discussions. His guidance helped me in all the time of research and writing of this thesis. I could not have imagined having a better advisor and mentor for my doctoral work with such patience, motivation, enthusiasm, and immense knowledge.

I would like to thank all members of the Fluidics and Biocomplexity Group and the colleagues I worked with in the Department of Engineering Science, University of Oxford. Special mentions go to Dean Chou, Dr. Nicholas Hawker, Dr. Steve Sheard, Tim Grob, Himanshu, Alisa Selimovic, Dr Brett Tully, Dr Emilie Holland, John Vardakis and Dr Giuliana Trippa for their support, inspiration and helpful suggestions.

China Scholarship Council is acknowledged for the scholarship which has supported me financially in the past three years.

Finally, I wish to express sincerely gratitude to my beloved family for their understanding and endless love and to my dear friends for their help and warm encouragement.

Contents

Appendix I

Appendix I: this appendix (both the hard and digital copies) is not available for public consultation until 1st May 2033.

List of Figures

1. Introduction and Motivation

In this chapter we shall provide some important definitions and terminology clarifications and will outline the main objectives behind this research. The challenges connected with the utilization of microparticles in medical diagnostics, especially regarding their separation and purification using traditional techniques, will be summarized and the rationale and structure of the rest of the thesis will be described.

Microparticles (MPs) are membrane-structured vesicles secreted by cells, with sizes ranging from 100 nm to 1000 nm. They are intensely investigated due to their physiological meaning and diagnostic potential, since they are very promising as biomarkers for physiology and pathology, as well as for diagnosis and treatment applications. Purification of microparticles through separation is a necessary step, both for microparticle detection and subsequent processing. However, microparticle samples are usually complex mixtures containing various other biological materials. The traditional techniques for microparticle separation are far from effective or efficient, a fact that has become the major obstacle for microparticle counting, analysis and practical overall utilization, to date. Therefore, innovative approaches are needed, capable of succeeding where traditional approaches fail. Such approaches promise to offer solutions not only for the separation of microparticles but also for the manipulation of other biomarkers, and thus would be promoting a wider range of diagnostic applications.

Microfluidics is the discipline that explores the mechanisms and devices controlling and manipulating small amounts of fluid, in channels with dimensions from tens to hundreds of μm. With progress in miniaturization and microfabrication, microfluidic technologies have been rigorously investigated and offer many advantages in terms of applications: high resolution and sensitivity; low priming volumes; low sample consumption; short process and analysis time; small size and low cost. Based on this, *Lab-on-a-Chip* (LOC) (or *Micro Total Analysis Systems* (μTAS)) technology adopts the concept of microfluidics and focuses on the

integration of multiple laboratory functions on a sub-millimeter chip, which can perform separation, detection and analysis simultaneously. So, microfluidic systems are an ideal solution for biomarker manipulation, including mixing, transport, separation and reaction/measurement.

Due to the small dominant characteristic length scale, the flows in microfluidic systems are laminar. However distinctive phenomena have been observed in fluids of such scales, which make microfluidics an area of substantial research interest. At the same time, these phenomena offer ways to manipulate particles, directly through emergent flow features. An example for this approach, which we shall describe in detail later on is the appearance of vortical structures. The complexity of microchannels lies in their curved (occasionally highly curved) 3D geometries: in order to utilize the limited space on the microfluidic devices, microchannels have to be built in a compact pattern, with considerable curvature. Importantly, as we shall show, this curved pattern is of particular relevance to particle manipulation in our research. In fact, the flows in curved channels present with very interesting flow features, for example pairs of longitudinal vortices, or secondary flow. Dean etc. [1] provided insight for such flows in curved pipes, demonstrating the existence of vortices, thus this type of flow is called Dean flow.

"Complicated three-dimensional geometries, and the possibility that suspended particles have dimensions comparable to the microchannels" have been listed among "the most important new themes introduced by the small length scales of microfluidic devices" [2]. This work precisely focuses on these concepts, individually and

integrally, most crucial to the transport phenomena within microfluidics and particle-related applications.

Suspended particles, especially when their size is considerable when compared with the conduit, have unexpected characteristics in their transport. Although efforts have been made to elucidate these mechanisms [3, 4], theoretical investigations on large-scale particle movement inside complicated 3D microchannels are very rare. In this work, a new numerical approach is developed to address such motion of particles whose dimensions are comparable to the channel (these are defined as 'large-scale' particles in this work). After confirming our results through comparison with experiments, this approach is proved to be not only sufficiently accurate but also very efficient computationally – of great importance when attempting to utilize simulation for practical design and optimization purposes. The ability to simulate these large-scale particles is extremely important and promising because it benefits our understanding and thus results in improved manipulation of pathogenic biomarker particles, human cells and industrial particles for various applications.

It is often found, that for these processes to take place in a repeatable and controlled manner and to enable applications, adopting purely hydrodynamic forces to achieve manipulation may not lead to adequate performance (for separation of difficultly discriminated particles for example – of main interest to our study). That's why external force fields are often considered, to aid and enhance manipulation.

Based on the type of external forces employed, particle separation techniques can be divided into different categories: acoustic, optical, electrical, magnetic, etc. In the

current research, the fluidic approach is supplemented using external magnetic fields. This approach is simple to implement and preferable for bio-particle manipulation: Firstly, it's been proven that cells with different magnetic properties can be separated easily by external magnetic fields without cell damage. Second, state-of-the-art magnetic separation technology can dramatically enhance the efficacy and efficiency of bio-particle manipulation.

Magnetic separation (also called immunomagnetic separation) uses biocompatible magnetic micro (nano) particles. It is implemented by a two-step process [5]: (1) the tagging or labeling of the desired biological entity with magnetic particles; (2) the separation of these tagged entities via a fluidic-based magnetic (or sometimes purely magnetic) separation device. By using this method, the targeted bioparticles (microparticles or biomarkers) can be manipulated and enriched for further analysis. By adopting suitable particle detection devices, the level of specific bioparticles or biomarkers can be quantified. In our research we shall show how these processes and functions can be integrated in a microfluidic substrate with optimal design as a medical diagnostic system, which can become an ideal point-of-care (POC) testing device. It is accepted that high-specificity microfluidic diagnostic technologies are paramount for global public health [6, 7]. In summary, we aspire to combine advanced understanding (accessed via validated simulations) of complex flow features, together with external magnetic fields (also evaluated using appropriate multiphysics simulation techniques) to design, evaluate and optimize a new class of microfluidic separation and purification devices.

The overview of this research is shown in Fig. 1-1.

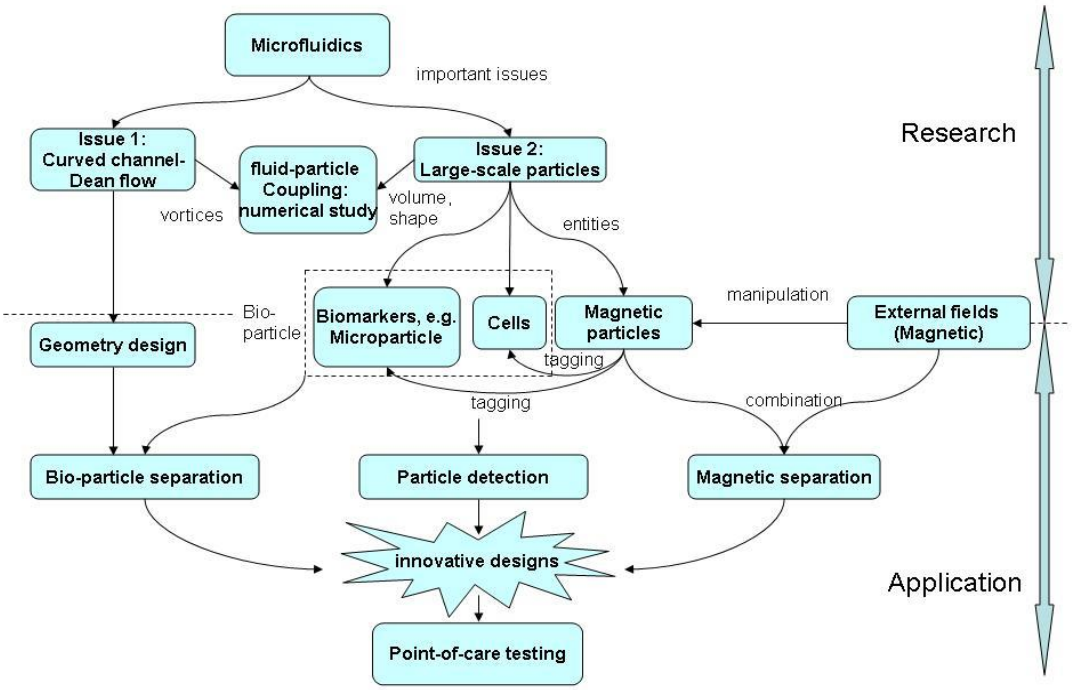

Fig. 1-1 Schematic of the elements and logical flow of the research presented in this thesis

Before we close this section with a brief description of the content of the subsequent chapters of the thesis, it is important to emphasize a distinction regarding development and utilization of appropriate computational techniques; a comment that will inform and guide the rest of the thesis. As Fig. 1-2 shows, biological elements, candidates for separation, fractionation and purification (to be used primarily for diagnostic purposes), span 4-5 orders of magnitude in size. More relevant, microparticles present us with sizes in the 0.1-1 μm range, whereas bigger cells are in the 5-40 μm range. A successful separation device must be able to handle (either using the same, unified, separation technique or different techniques) the entire range of particle sizes, since they are all found in, say, blood samples. For Point Of Care

microfluidics-based devices, there is strong preference that a *single* separation technique, that is of appropriate scales (i.e., can fit on a lab-on-a-chip device), operating either as a single pass or as a series of consecutive separation passes, handles the entire spectrum of particle sizes. Therefore, the design objective is to avoid any preprocessing (and thus additional cumbersome equipment) and to use a separation technique that can process and remove/fractionate in steps all the components that span the ranges discussed above, while ultimately purifying the target microparticles.

The main challenge in this thesis has been the development, establishment and validation of *computational techniques* for *design*, capable of handling the complex particle-flow interactions entailed in the diagnostic processes mentioned. As such, and as we shall see in the chapters that follow, we have surveyed the literature in order to examine whether appropriate techniques for studying the various sized particles are available. What this review revealed was that while very small sized particles, at relevant volume fractions, exhibit weak if any coupling with the flow, bigger particles actually affect the flow very substantially. Thus, whereas a variety of very efficient techniques exist for the small particles[1] and the weak coupling case (directly applicable to the typical microparticle range), substantial challenges were identified in retrieving and establishing computationally efficient and accurate techniques capable of handling the bigger particles and their strong coupling/interaction with flow.

Since the overarching objective of this thesis has been the verification and

[1] Such techniques, often referred to as *spray* techniques, assume that very small particles occupy negligible volume, and couple with the flow as point momentum sources/sinks.

validation of computational techniques for the *practical and integrative design* of microfluidics particle separation, it became apparent early in the process that very substantial effort would be dedicated in the front of numerical methods for strongly coupled larger particle-flow situations. We cover the easier small particle – flow situations as well (see Chapter 4 for relevant discussion and results) but we believe that the numerical innovations introduced address first and foremost the case of larger particles that interact strongly with the flow: this is where we recognized a gap in available computational techniques existed and where a contribution was needed.

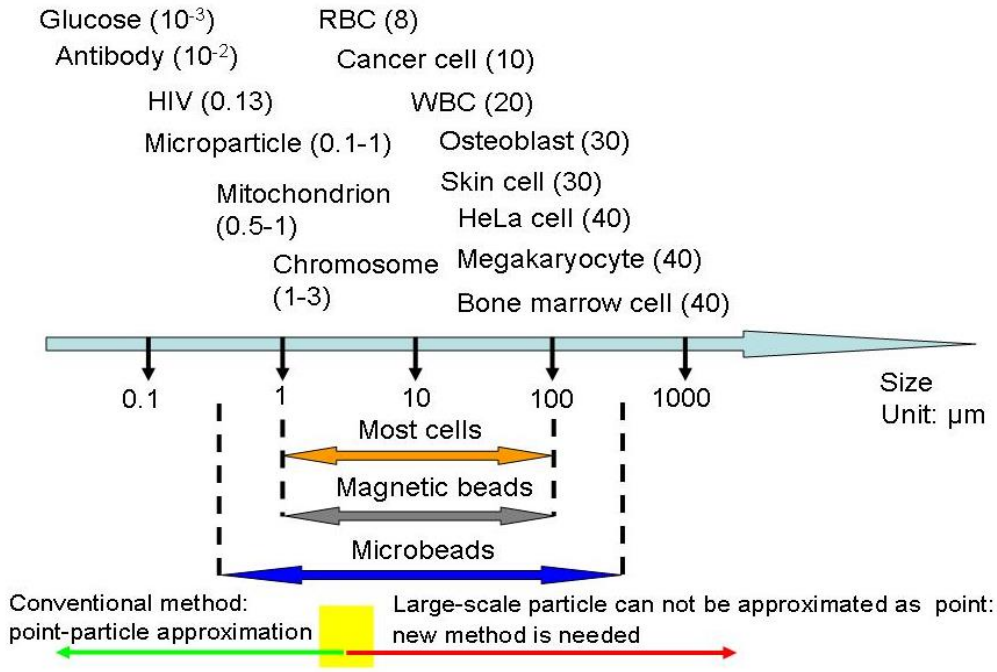

Fig. 1-2 Schematic of biologically relevant candidates for separation techniques and range of application of computational techniques capable of handling the size ranges

The rest of this thesis is organized as follows:

- Chapter 2 reviews the literature regarding microparticles, microfluidics and

particle separation, particles in straight channel, particles in curved channels & Dean flow, large-scale particle simulation techniques and magnetic separation.

- Chapter 3 outlines the numerical methods developed and used; - *Computational Fluid Dynamics* (CFD) for fluid modeling (based on the finite volume method), the *Surface Marker Point* method for large-scale particle trajectory evaluation as well as our newly developed approaches for efficient fluid-particle coupling.
- Chapter 4 is dedicated to validation. The accuracy of the numerical methods used and/or developed are demonstrated, including grid and time step independence, verification through 3 cases of particles' transport in Dean flow, particle rotation and particle sedimentation. Lift force on particles is also investigated and the results are compared with a point-particle approximation - discrete particle method.
- In Chapter 5, results of pure fluid-particle transport are presented, including hydrodynamic focusing, size-based separation in curved channels, particle focusing and particle separation in multi-inlet curved channels.
- Results regarding external force fields and original designs are presented in Chapter 6, including magnetic separation of magnetic particles, the innovative Magnetic-Dean flow separation and a new design proposed for diagnostic POC system.
- Conclusions and findings are summarized in Chapter 7.

2. Literature Review

Biomarkers are a group of biological indicators of diseases, including molecules, vesicles, cells, tissues etc. Recently, much importance and promise has been placed on a class of biomarkers called microparticles, of high physiological and pathological significance. However, their separation is so challenging that we have to exploit state-of-the-art technologies based on microfluidic to benefit from the diagnostic potential they offer. To reveal the relevant latest findings and related computer modeling techniques, this chapter reviews the literature regarding microparticles, microfluidics and particle separation, particle flows in straight channels, particle flows in curved channel and Dean flow, as well as large-scale particle simulation and magnetic separation.

Microparticles as an important *bioparticle* group, among others, are in great demand for biomedical research, but they are hard to separate directly. Since the human cells needing to be precluded (or to be gathered for other purposes) range in the 5-40 μm range, mentioned in Chapter 1, and the smaller bioparticles (such as microparticles) can be captured by the specially coated beads (magnetic beads or polymer beads) which are normally above 1μm, the particle size of 5-40 μm is the focus in this research for particle manipulation applications.

2.1 Microparticles

Microparticles are cell-derived membrane-structured vesicles. Their size ranges from 100 nm to 1000 nm. They are gaining more and more attention for a wide-range of applications, of vital diagnostic and prognostic significance.

Microparticles (MPs) are encapsulated by a phospholipid membrane, equipped with certain membrane receptors and proteins. A precise definition of MPs is still lacking – however, they are generally regarded as a population of small phospholipid vesicles which are released by most cell types during apoptosis and/or activation [8, 9].

For a long time, MPs were thought as inert cell debris – the metabolic waste released by cells. However, there is increasing evidence that MPs actually have sophisticated release mechanisms which have great physiological and pathophysiologic research value. They serve as an important species of biomarkers for various biological and pathological processes. Moreover, it is demonstrated that MPs can interact with neighboring or remote cells, thus build up an intercellular

communication system for the whole body [8].

MPs are heterogeneous, both in terms of size and origin. They are derived from platelets, endothelial cells, blood cells and other cell types. MPs release is connected with the membrane-remodeling process in which the asymmetric distribution of constitutive phospholipids between the two membrane layers is broken [8]. MPs released from cells were demonstrated firstly to be shed from platelets and called *platelet dust* [9]. For the past several decades the term *cell membrane microparticles* is also used, while other terms are also adopted, like endothelial microparticles, or microvesicles. Through this document, we utilize the most common term microparticles (MPs).

Fig. 2-1 [10] shows heterogeneous MPs which have different origins as well as varying size, shape and density. It is obtained through electron microscopy analysis of microparticle preparation obtained from a suspension of washed platelets (free of white cells and red cells) after stimulation by thrombin [10], also containing the platelet body, organelle and non-membrane structure.

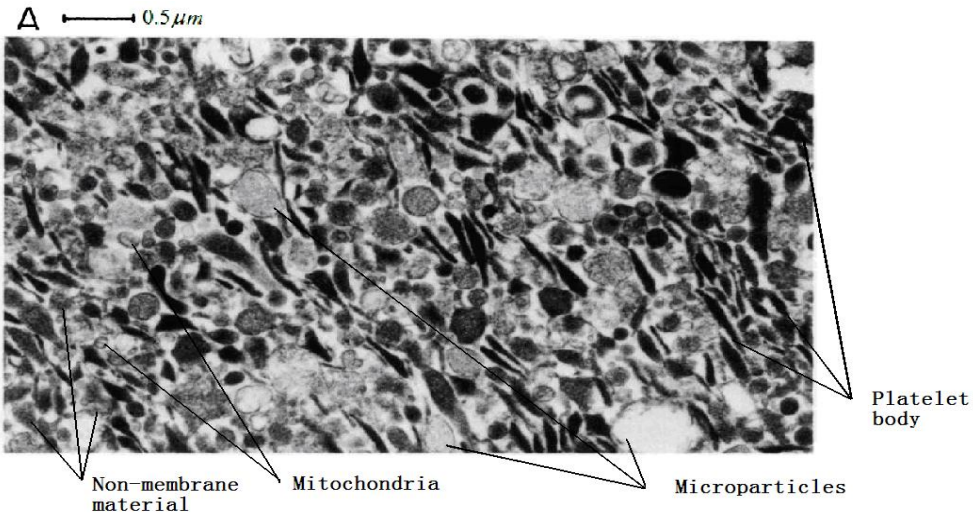

Fig. 2-1 Ultrastructural appearance of MPs [10]

Nowadays MPs have gained significant attention within the fields of biology, physiology, diagnostics, medicine and beyond. They are of great importance for transfusion medicine because MPs are present in both plasma and cellular blood products [11], but more importantly, they play a key role in a wide range of physiological and pathological activities as a significant biomarker.

2.1.1 Formation mechanism and composition of MPs

The exact mechanism of MP formation has not been fully described yet, especially when the diversity of MP origins is taken into account. However, there is consensus about the characteristics of MPs release, which is not a random process like degradation of the plasma membrane of dying cells but a highly controlled process, triggered by specific types of cell stimulation. Another kind of smaller vesicles, *exosomes*, are a particular type of microparticles generally ranging between 30-100nm [12]. Exosomes have a different origin, which is related to endocytosis and exocytosis[2]. This similarity in both density and morphology leads to profound difficulties in distinguishing and separating exosomes from MPs. Fig. 2-2 shows the morphology of MPs and exosomes.

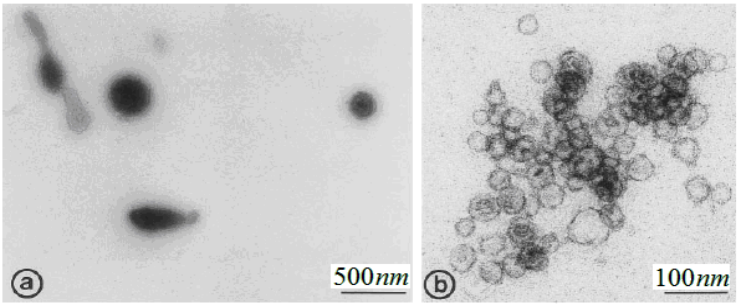

[2] Endocytosis is the process in which cells absorb molecules, like proteins, from outside the cell by engulfing them with the cell membrane. Exocytosis is the reverse process in which the secretory vesicles are transported out of the cell membrane.

Fig. 2-2 Electron micrographs of MPs and Exosomes [13]: (a) Plasma membrane-derived microvesicles (b) Exosomes

For MPs, a 'reverse budding' is mainly responsible for their formation mechanism. Normally, most eukaryotic[3] cells have a special asymmetric distribution of plasma membrane phospholipics: The constitutive phosphatidylserine (PS) and phosphatidylethanolamine (PE) are mainly sequestered in the inner cytoplasmic layer of the plasma membrane, while choline sphingomyelin (SM) and phosphatidylcholine (PC) are located at the outer layer. This balance is mainly maintained by the cooperative function of the enzymes *flippase* and *floppase*. This asymmetric distribution is known as the barrier keeping ions, proteins and other molecules to prevent them from diffusing outside. Also it can pump ions to regulate salt concentrations and pH inside the cells. Interestingly, it plays a key role in the MPs release. Two particularly relevant factors are involved in this process [14]: the increase of intracellular Ca^{2+} concentration and the reorganization of the cytoskeleton. Through cell stimulation, the intracellular Ca^{2+} increases, inhibiting the function of flippase for moving another molecule across the membrane layers. Under the effect of a particular flippase, *scramblase*, the phospholipids are allowed to move randomly between membrane layers, leading to the collapse of lipid asymmetry within minutes. Thus the PS and PE cannot be transported to the inner side of the membrane, displaying large amount of PS on the outer surface of the membrane. This change of the shape and mechanical stability may lead to membrane budding. The

[3] Almost all species of large organisms are eukaryotes, which have a double lipid bilayer that encloses the genetic material-nucleus, including animals, plants and fungi.

reorganization of the cytoskeleton results in the deformation and detachment of the plasma membrane for the PS^{+}MPs release. These phenomena are considered the main causes of the shedding of MPs into the extracellular environment.

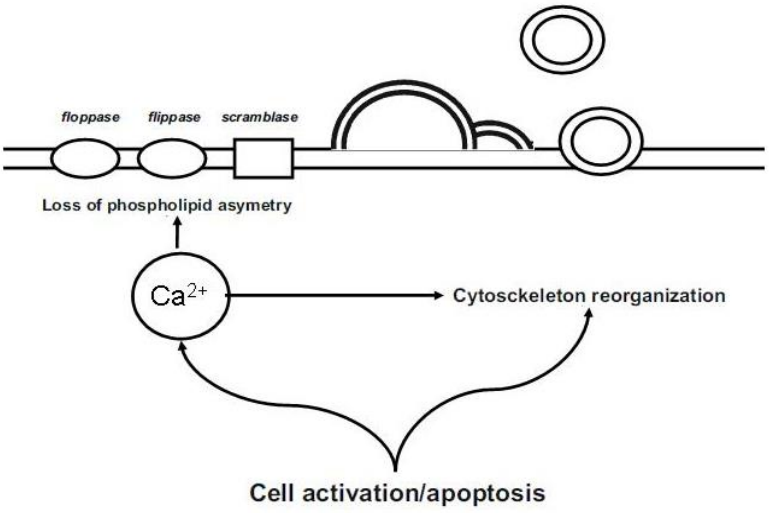

Fig. 2-3 Schematic of the mechanism of MPs formation

The membrane of the MPs, which is derived from the cell membrane of the parental cell, consists of lipids and proteins, displaying the distinct markers of the origin. Analysis of blood of healthy donors indicates that phosphatidylcholine comprises almost 60% of the lipids [15]. Other lipids as sphingomyelin and phosphatidylethanolamine constitute 30% of the lipids. Phosphatidylserine, phosphatidylinositol, lysophosphatidylcholine, lysophosphatidylserine, and lysophosphatidylethanolamine account for a small proportion. In the blood of healthy donors, about 75% of the microparticles are platelet-derived [9, 10]. The membrane molecular pattern and the internal content of MPs both vary by different original cell types and mechanisms of MPs release[16].

2.1.2 Importance of MPs

The circulation MPs may be of great importance in many physiological and pathological processes, including hemostasis, thrombosis, inflammation, modulation of vascular tone, angiogenesis, stem cell engraftment, immunity, cancer metastasis etc. [11].

As an example, we can describe the role MPs play in one of the most important biochemical cascades in human physiology; that of thrombosis. *Tissue factor* (TF) is a type of membrane glycoprotein which can act as a trigger of the blood coagulation system, while PS is an essential phospholipid for surface thrombin generation [17]. MPs can expose both of them as well as bind with other plasma coagulation factors. The coagulation system is activated both in disease states and in healthy individuals with the effect of MPs [18]. For example, cardiopulmonary bypass (CPB) is an important surgical technique that temporarily replaces the function of heart and lungs during operations, maintaining the circulation of blood and its oxygen content, through the use of an extracorporeal circulation/oxygenation machine (the *heart-lung* machine). It is showed that pericardial blood from cardiopulmonary bypass patients has a much higher level of platelet derived MPs (PDMP), monocyte-derived MP (MDMP) and other MPs of different origin. These MPs can stimulate severe coagulation [19]. It is demonstrated that isolated MPs from pericardial blood of cardiac surgery patients and venous blood of healthy individuals were strongly procoagulant in rat [20]. There is also evidence that MPs in blood from healthy individuals support thrombin generation via some special pathways [21].

MPs released from human T-lymphocytes [22] and endothelial cells [23] can also impair the relaxation and NO production in aortic rings. On the same theme, the vasoconstricting effect by platelet MPs has also been demonstrated. It is demonstrated that circulating MPs would take part in prothrombotic and proinflammatory activities by stimulating platelets, endothelial cells and leukocytes. For example, Platelet MPs can bind, activate and aggregate neutrophils in vitro [24]. Platelet MPs also can increase the adhesion of monocytes to endothelial cells in vitro.

There is evidence suggesting that circulating MPs play a role in angiogenesis activities. The lipid component of the PDMP may be a major active factor for a potent angiogenic stimulator [25]. A dose-dependent pro-angiogenic effect of PDMP was observed in the rat aortic ring model[26]. Some proangiogenic activities of endothelial microparticles (EMPs) are also reported.

MPs containing a type of protein, C-C chemokine receptor type 5 (CCR5), can transfer the receptor of human immunodeficiency virus (HIV)-1 [27]. This intercellular pathway may lead to exceeding infection of tissues. Furthermore, it is suggested that PDMPs may play an important role in tumor progression/metastasis and angiogenesis in cancer [28].

Experimental data also suggest that the released MPs have other effects in organ defense systems. PS can take effect as a sign for identifying injured cells which are ready for removal. In reverse, decrease of PS can be a stimulation factor triggering cell repair. Thus there is opportunity to find a way for repairing the cells rather than inviting phagocytes to remove the cells, a process which when widely adopted is

detrimental for organ function. There are 2 ways for removing PS [11]: to hide the PS back to the inner layer of cell membrane or to release PS^{+}MPs. Clearly there is no more need for the metabolic energy required for MP release and also this release process could be faster than the translocation of PS back into the cell membrane.

The discussion above highlights the high relevance of MPs to a multitude of diseases such as coronary disease, diabetes, hematologic diseases, antiphospholipid syndrome, infectious diseases, pregnancy-related disease, neurologic diseases, inflammatory diseases and cancer etc. [11]

2.1.3 Conventional methods for MPs detection and collection

Regarding techniques for MPs analysis, several approaches have been proposed and tested. However, two of them are most widely used [11]: microplate affinity assay and flow cytometry. There are 2 types of microplate affinity assays. One is the enzyme-linked immunosorbent assay (ELISA), which uses antibodies corresponding to specific types of MP antigens for detection and enrichment. In ELISA [29], an unknown amount of antigen is affixed to a surface. Then a specific antibody, which links to an enzyme, is made to come in contact with the surface so that it can bind to the antigen. The final step is that the enzyme can be converted to a detectable signal by some biochemical substance added in, which is defined as substrate. For example, the signal could be fluorescence triggered by fluorescent antigen/antibody complexes. The amount of antigen in the sample can be inferred through the magnitude of the fluorescence. The whole process is demonstrated schematically in Fig. 2-4. For

microparticles, assays use annexin V [11] in the presence of Ca^{2+} to detect or capture PS^{+}MPs. Annexin V is a phospholipids-binding protein which has a high affinity for PS with the presence of Ca^{2+}. PS+MPs could be detected using a chromophore-conjugated annexin V or captured using immobilized annexin V. Microplate affinity assay's main advantage is that it could be suitable and accurate for a wide range of MPs types, sizes and other parameters. Also it is comparatively easier to operate and cheaper than the alternative, discussed below. However the disadvantages include lack of direct quantification of MPs, MP size and a complex non-continuous (batch) process, sensitive to a large number of often difficult to control parameters.

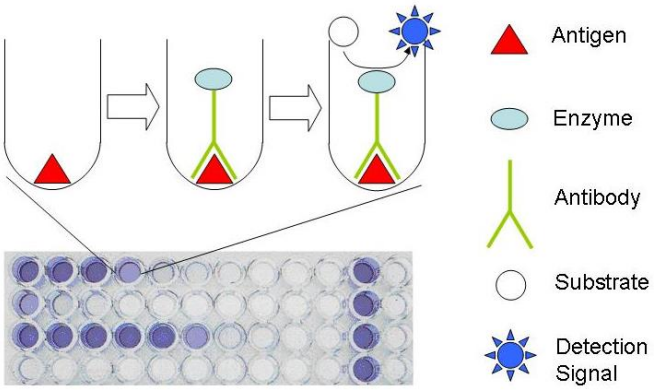

Fig. 2-4 Schematic of ELISA

On the other hand, flow cytometry is the most commonly used and basic method for MP analysis. Flow cytometry is a technique for examining and analyzing microscopic particles, such as cells, MPs and chromosomes. The technique can be briefly outlined as follows: Firstly suspend MPs in a stream of fluid and then let them pass through a very narrow nozzle which is surrounded by a concentric larger nozzle. A different fluid component is infused into the space between the two nozzles which forms the outer fluid layer, called *sheath fluid*. Sheath fluid has the specific effect of

focusing the fluid ejected from the inner nozzle by fluid surface forces when the flow is laminar. This technique is called hydrodynamic focusing. If the two fluids differ enough in their velocity or density, they do not mix but rather form a two-layer stable flow. The sample is injected into the middle or central fluid layer which is restricted by the outer sheath fluid to a narrow band small enough to just let single particles pass, which makes the MPs pass through a *detection* region one at a time. Then, a beam of light (usually laser light) of a single wavelength is directed onto the stream of MPs suspension. A number of detectors are fixed around the space where the stream passes through the light beam: one in front of the light beam (Forward Scatter or FSC), several perpendicular to it (Side Scatter or SSC) and one or more fluorescent detectors.

Fig. 2-5 shows the schematic structure of a flow cytometry device. Each suspended particle passing through the beam scatters the light, and fluorescent biochemicals attached to the particle may be excited to emit light at a specific wavelength different from the light source. This combination of scattered and fluorescent light is captured by the detectors. By analyzing fluctuations in brightness at each detector, various types of information about the amount of particles and the structure of each individual particle are derived. The simultaneous analysis of the physical and chemical characteristics of thousands of particles per second can be achieved using this technique. Advantages of flow cytometry involve that large numbers of MPs can be analyzed in a single sample continuously. However, the disadvantages are that it's expensive, the process of sample preparation and operation is quite complicated and

even today the success of a particular experiment depends on the efficacy and experience of the operator. Especially the size of MPs is often at the resolution limit of this device.

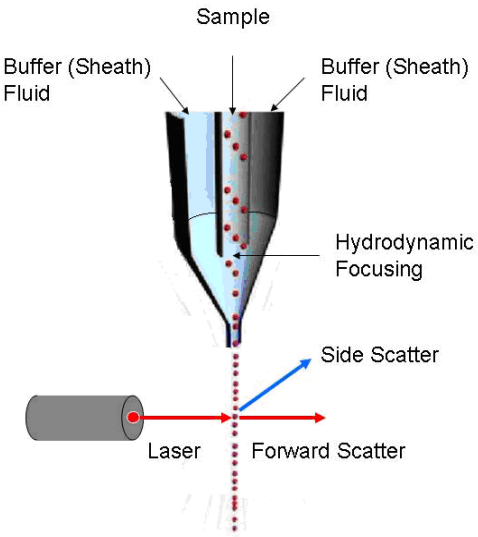

Fig. 2-5 Schematic of flow cytometry

Beyond the techniques discussed above, it is of course commonplace to utilize centrifugation and ultracentrifugation for suspension clarification. In microbiology and cytology these methods are used, for example, to accelerate the sedimentation of whole cells or to separate certain organelles from whole cells. In such a process, a tissue sample is first homogenised to break the cell membranes and mix up the cell contents and then subjected to rapid spinning, i.e., centrifugation. The equilibrium sedimentation for separation is achieved according to differences in density. However for MP samples, the very small differences in density make this technique impractical. It requires considerably high centrifugal acceleration (100,000g), is very time-consuming (often 24h) and is operated in complex and discontinuous settings by trained technicians [30]. Centrifugation also presents with further limitations, in that

centrifuges are hardly compatible with in-line systems and incapable of dealing with small sample volumes [6]. Finally, filtration, another technique used for separation, suffers from blockage of filters, and serious difficulties with such small target particle sizes, rendering it unsuitable for this application.

In summary, there was no generally applicable and adequately robust method available for detection of all MPs in blood (or other samples) to get a total MP count [11]. The inconsistency of different analyzing methods leads to discrepancies in results on the same sample, something that is not acceptable. Many of the difficulties lie in the complexity and richness of the blood environment and in differences of samples.

To further emphasize the challenges connected with this type of diagnostic, we can mention that MPs of equal size are difficult to distinguish from platelets or other aggregates. Different states of health and different types of diseases will lead to different composition for the MPs. Thus effective MPs separation techniques can play a vital role in their accurate quantification and characterization, which are essential for further analysis. Any technique capable of achieving reliable and repeatable separation holds great promise for investigating the relationship between the special types of MPs and clinical risk factors [31].

2.2 Microfluidics for particle separation

2.2.1 Microfluidics

To manipulate bioparticles at micro or sub-micro scales, microscale channels are

emerging as a technique/device of choice. Microfluidics and lab-on-a-chip (LOC) devices are intensely investigated and in high demand along with further developments of miniaturization and microfabrication. They have shown dramatic advantages over more traditional techniques like centrifugation and filtration [6]. Firstly their small size renders minimum need for samples or reagents, which means microfluidics can perform with high resolution and sensitivity, short analysis times as well as low cost. Second, due to the scale down, microchannels operate at laminar flow conditions, i.e., without turbulence, which is beneficial in many situations, especially for particle and sample manipulation. Thus microfluidic devices are widely adopted in molecular analysis [32], biological analysis [33], single cell manipulation [34] and drug development [35] etc. They are also adopted in applications of multiphase flows control, for example, the generation and manipulation of bubbles [36], droplets [37] of dispersed phase in another continuous liquid.

Among the potential applications, recent techniques of micro-scale particle separation through microsystems have gained significant attention in the fields of biology [38], chemistry [39], microchemical processing and microsystems engineering [40]. Particularly particle separation is recognized as a necessary preparation step in most biochemical analysis thus plays a key role in diagnosis, because, as mentioned above, separation techniques are vital to biochemical analysis because the isolation of cells and particular biomarkers is essential. They can lead to versatile applications in biochemical analysis, such as DNA analysis (nucleic acid sequence analysis), proteomics analysis (proteins and peptides), clinical analysis

(blood tests), immunoassays, toxicity monitoring etc. [41]. One promising application comes up with the concept of point-of-care test (POCT), which is highly suitable for monitoring patient response to therapy and diagnosing the early stage of diseases [42].

Microparticles become a representative example where laboratory measurement of biological substances can reflect the activity and/or stage of disease processes, i.e., act as biomarkers. By detecting different types of biomarkers, an easy and noninvasive way of early diagnostic methods for corresponding diseases is possible. Particularly, in order to achieve early detection of the top killers of the world, cardiovascular diseases [43] and cancer [44], biomarkers have been intensely investigated. However, biomarker detection relies on bioparticle separation from complex samples, like whole blood, saliva or urine etc., which increases the difficulty for separation.

In comparison with microplate affinity assay and flow cytometry, the technology of bioparticle separation we intend to pursue is a further application which has a broader meaning and broader relevance in therapeutics, but also requires more in-depth study as well as more complex integrative approach. In the biomedical field, when the isolation of pure cells and/or biomarker types is essential, separation techniques are vital to apply. Importantly, separation is also a key activity of diagnostic and analysis tools. The separation of specific human T-lymphocytes from whole blood for the HIV diagnostic and control is a typical example. Bioparticle separation techniques would also bring benefit to the detection of cancer cells or cancer cell communication, as discussed above.

2.2.2 Particle separation approaches

According to the different kinds of external forces, microparticle separation can be divided into five different categories: fluidic, optical, electrical, magnetic and acoustic methods [45].

In fluidic separation methods, centrifugation and ultracentrifugation are traditional procedures in microbiology and cytology, used to separate cells, or certain organelles from whole cells. In the process, a tissue sample is first homogenised to break the cell membranes and mix up the cell contents and then subjected to centrifugation. The equilibrium sedimentation for separation is achieved according to differences in density. However for MPs samples, the very small differences in density make this technique inappropriate for MPs separation. Field-flow fractionation (FFF), introduced by Giddings [46], is a separation technique where a particle suspension is driven through a channel, thus particles are separated perpendicular to the direction of flow based on different mobilities corresponding to the intrinsic characteristics of different components. For instance, based on various diffusion rates, smaller particles diffuse more quickly, while larger particles diffuse more slowly; therefore larger particles can be enriched and smaller particles diffuse to other region [47]. Split-flow thin (SPLITT) fractionation channels have further adopted one inlet and one outlet splitter [48]. Typically, separation in SPLITT is carried out in a thin H-shape filter. FFF and SPLITT are reviewed and related simulations have been accomplished [49]. New approaches, that we shall explore further on, that attempt separation by taking advantage of fluid mechanics features and fractionate based on size also fall under

this category. Fluidic separation has the advantage of not requiring any external fields.

Optical method would use optical tweezers which is a manipulation tool creating a focused single laser beam to trap a single particle. This method is very flexible to new environments and shows very high specificity. However, it applies to single particles only, and in the vast majority of case is interactive (i.e., requires a human user). Also the optical data need to be converted to electronic results [50]. Therefore it is inappropriate for complex clinical samples.

The acoustic method [51] applies an ultrasonic standing wave field generating a primary radiation force to move particles. Whether the particles move toward or away of the pressure nodes depends on the acoustic contrast factor, a function of density and compressibility of the particles and the solution. Particles with different acoustic properties can move together in a laminar flow and be collected through appropriate collector ports. The acoustic method can have very high separation efficiency – to the best of our knowledge it has not been used for MP separation to date.

There are two main types of electric field-based methods: Electrophoresis [52] adopts a uniform electric field to transport and separate different kinds of charged particles; Dielectrophoresis [53] transports and separates neutral materials caused by polarisation effects in a nonuniform electric field. The electric method for bioparticle separation is a relatively established technique because electric-field manipulation is well-studied and potent at the microscale. Dielectrophoresis has been applied to separate cells according to their size or dielectric properties. However, the integration of electrodes which is to generate the electric filed in the microsystem often involves

complex and challenging manufacturing and needs careful design.

In the magnetic separation method [54] the particles to be separated have either intrinsic magnetic properties or are labeled with magnetic beads. Magnetic fields are completely benign to biological entities, even are relatively high field strengths, and therefore quite suitable for sorting cells and microparticles.

Considering which method is to be adopted should be based on the needs of the application, including particle physical characteristics, separation criteria, throughput, efficiency, physiological effects etc. However, most separation techniques are using user-defined mixtures or biological samples, which do not necessarily deliver favourable properties. The micro-scale manufacturing and related miniaturization challenges are another challenge [55]. Among different kinds of separation methods, an external magnetic field is the easiest to set up. Furthermore, magnetic separation can use small magnetic particles to attach targeted bioparticles, so the separation processes do not depend on bioparticle intrinsic physical or chemical properties, such as size, density, surface charges etc., and they are not affected by ambient conditions, like fluid pH, ionic concentration, temperature etc [29]. Suitable combinations of fluidic-magnetic forces [56] appear to offer great promise for highly specific and efficient separation of complex mixtures of microparticles or other biomarkers. Thus, in this study, our focus shall be the fluidic and magnetic separation.

2.2.3 Magnetic separation

Magnetic separation (immunomagnetic separation, IMS) uses biocompatible

magnetic micro- or nano- particles that facilitate the purification and detection of biomolecules in a wide range of samples, including nucleic acids, proteins and cells [57, 58]. Commercial magnetic particles (MPs) used in magnetic separation are normally paramagnetic or superparamagnetic at the micro scale [57]. To make MPs biocompatible and to improve surface attachment characteristic, a polymeric layer is usually coated on the outside of a MPs core.

Magnetic separation consists of two steps: (1) labeling or tagging the desired biological materials with magnetic particles; (2) separating the tagged entities by external magnetic field through a fluid-based separation device [59]. Fig. 2-6 shows the procedures of standard methods for magnetic separation: (a) magnet is fixed beside the channel and the magnetically labeled bio-entities are attracted to move to the side wall while the unlabeled materials can be washed away; (b) strong magnetic field gradient set at a region of the channel can capture the magnetically labeled targets.

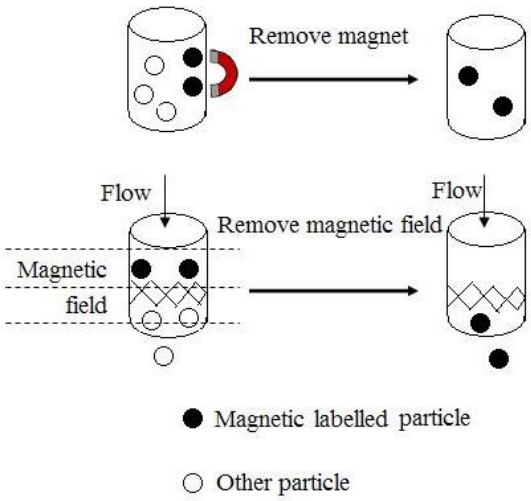

Fig. 2-6 Common methods of magnetic separation adapted from [59]

By using such techniques, the targeted bioparticles (microparticles or biomarkers) can be manipulated and enriched for further analyzing and diagnostic purpose [60-62]. The separation and detection procedure of the captured magnetic particles is shown in Fig. 2-7 [63]. Through the processes of miniaturization, magnetic separation has already been integrated into existing microfluidic systems [64, 65].

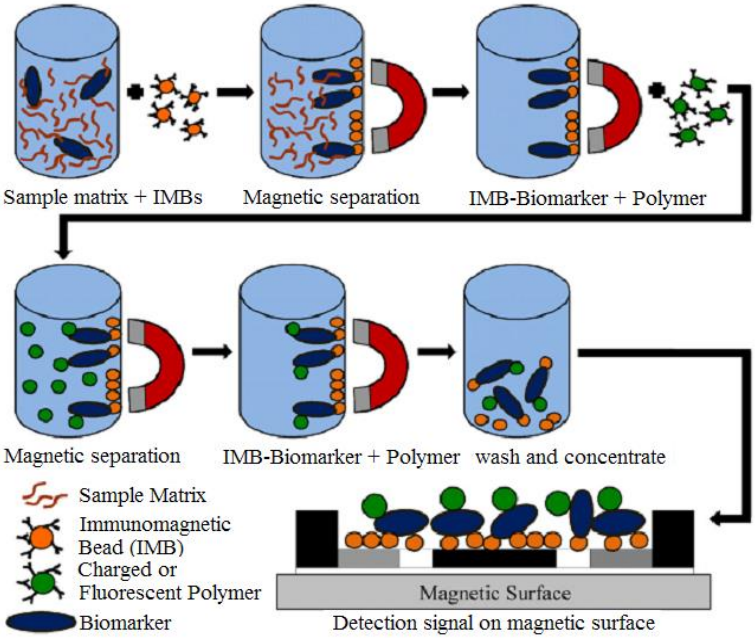

Fig. 2-7 Integrated magnetic separation and detection procedure [63]

2.3 Towards fluidic separation: Single particle dynamics

Generally, 3 categories of forces are controlling the movement of a particle in a fluid: (1) forces through the interface between fluid and particles, (2) forces due to the interactions between particles, and (3) forces imposed by external fields [66], e.g. electric field or magnetic field. Type (3) forces depend on the external field applied. (2) can be ignored here given the evidence that in microchannels, microparticles with

dimensions comparable to the channel would follow longitudinal alignment due to hydrodynamic repulsion. Such phenomena can be explained as that when two particles are moving close to each other, the fluid between them would be extruded out of the space, which will in turn impose a force on both of the particles and deter further approaching. Especially when the dimension of the particles is comparable to that of the channel, the fluid between the particles is more difficult to be squeezed or stretched without influencing the overall velocity distribution dramatically. In fact, the interparticle spacing of neutrally buoyant suspension has been observed in millimetre scale pipe flow as single particle trains aligned in the flow direction [67]. In high or low aspect ratio rectangular straight microchannels, two evenly-spaced streams were also reported [68, 69]. This effect is also suggested to be related to the particle Reynolds number $\mathrm{Re}_{\mathrm{P}} = \frac{\rho U_m d_{\mathrm{P}}^{\,2}}{\mu W}$, where ρ and μ are the fluid density and viscosity, U_m is the maximum channel velocity, d_{P} is the particle diameter, W is the channel width. When reducing the dimension down to microscales, particles flowing in straight or curved microchannels align in the direction of flow with a preferred interparticle spacing, which manifests as uniform spacing, when the particle Reynolds number is of order 1 [70]. This effect is capable of reducing particle colliding and clogging, which is important for flow cytometry applications [71, 72]. Apart from this, the separation process is usually pursued at a lower particle concentration (i.e., with properly diluted samples), under which circumstances the interactions between particles are rare.

Thus, the key factor, forces through the interface between fluid and particles, should be carefully studied. Firstly is the drag force on the sphere particle, $F_D = \frac{1}{2}\rho v^2 C_d A$, where v is the particle speed relative to the flow, C_d is the drag coefficient and A is the reference area (πr^2 for spheres). In Stokes flow, the drag force on a sphere can be shown to be $F_D = 6\pi\mu r v$. Apart from the drag force due to the relative velocity between the particle and flow, there are also virtual mass effects, which relate to inertia added to a object when accelerating or decelerating because the object must move some volume of surrounding fluid with it; the Basset force, due to the temporary delay in local boundary layer development; the Saffman force introduced by the velocity gradient and the force triggered by the pressure gradient; as well as the Magnus effect by the force due to rotation of a particle [73]. The Saffman force and the Magnus force are both confusingly called “lift force” in various articles, for these forces are both perpendicular to the oncoming flow direction and induce a lateral migration. Throughout the discussion that follows, we define the lift force as equivalent to the Saffman force. Each one of the effects and forces listed above should be considered one by one for importance and eventually inclusion in the modelling effort. Firstly, the virtual mass effect accounted for a sphere particle is $F_{vm} = \frac{M_f}{2}\frac{dU}{dt}$, where M_f is the mass of fluid displaced by the sphere. It only should be considered in bubble flows or when the particle acceleration is the most important [74]. Since in most of the processes the particle is traveling at near-settling velocities, we don’t undertake effort to analyze virtual mass effects in detail, but we integrated this effect into the simulation. For the Basset force, at such a micro scale, the typical time for a

particle response in a flow, the Stokes relaxation time ($\tau_S = \frac{\rho_P d_P^{\,2}}{18\mu}$), is extremely small, so in most studies Basset force is assumed to be small and can be neglected. In particularly long and thin microchannels, the force on a sphere due to pressure gradient is mainly longitudinal, expressed as $F_p = -\frac{\partial p}{\partial z}\frac{\pi d_p^{\,3}}{6}$, where $\frac{\partial p}{\partial z}$ is the pressure gradient along the direction this force is imposed to. However because in an equal cross section channel this gradient is mainly longitudinal, the force due to pressure gradient is less important. In very thin microchannels, the main velocity component is the one in the axial direction, restricting the particle from rotating. In fact the ratio of the Magnus force to the Stokes drag is expressed as $R_{MS} = \frac{d_P^{\,2}}{24}\frac{\rho}{\mu}\Omega$, where Ω is the angular velocity of the particle [66]. The microparticle diameter d_p decreases this ratio dramatically, thus the Magnus force can also be neglected. For a 10-μm particle rotating at 2π rad/s perpendicular to the flow direction with the relative velocity of 0.1m/s, the Magnus force is merely 0.25e-12 N. So, there are just 2 forces left to be analyzed in detail: drag force and lift force (i.e. Saffman force).

When considering a curved channel, a turning frame of reference attached to the centre line of the curved channel can be adopted. In such a non-inertial reference frame, we have to consider the centrifugal force, which is caused by inertia. It's also an essential factor for the fluid phase to form Dean vortices.

2.4 Particle in a straight microchannel

To investigate drag force and lift force effects in straight channels, we begin with

the simplest case, straight channels of circular cross-section. As the most idealized geometry of a pipe, this topology has been studied intensively. However the principles of particles drifting in pipe flow have not been fully understood. In 1960s, Segre and Silberberg [75] surprisingly found that neutrally buoyant rigid spheres focus to an annulus when drifting in a tube. Namely, the fully developed particle distribution is non-uniform, but with maximum concentration at a radial position 0.6 of the pipe radius from the centerline. This effect is termed 'tubular pinch', because of the tube-like shape of the annular region to which particles migrate, shown in Fig. 2-8, which is an experimental observation [76].

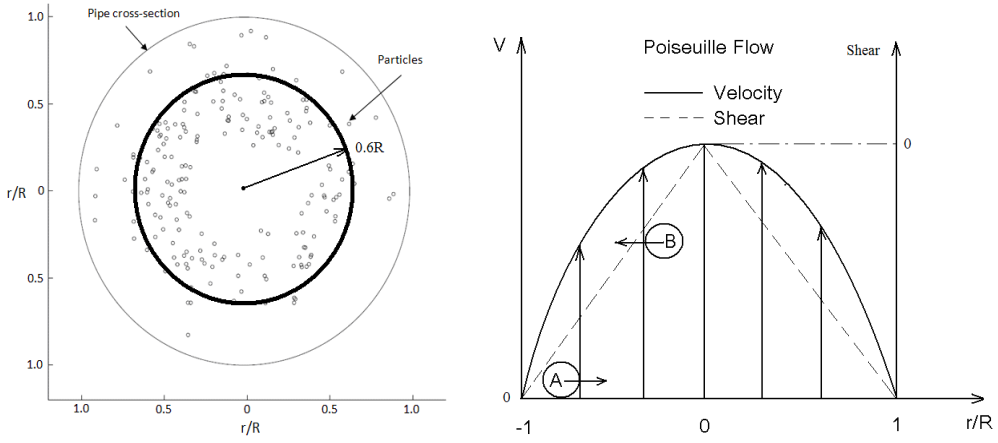

Fig. 2-8 Tubular pinch effect in a pipe [76] and schematic of ideal velocity and shear distribution in Poiseuille flow

This non-intuitive phenomenon is explained by the fact that particles moving at a relative velocity in comparison to the surrounding flow will be subjected to a corresponding lift force due to the velocity gradient. Saffman investigated the lift effect on a sphere in a slow uniform shear flow [77]. The Saffman force is considered to be the key factor leading to the microparticle transverse displacement due to velocity gradient. Saffman derived an expression for the lift force acting on the sphere

particle moving in a constant shear flow at low particle Reynolds number $\mathrm{Re}_P \ll 1$:

$$\mathbf{F}_S = \frac{K\mu}{4} d_P^{\,2} \sqrt{\frac{1}{\nu}\left|\frac{1}{\nabla \times \mathbf{U}}\right|}((\mathbf{U}-\mathbf{U}_P)\times(\nabla\times\mathbf{U}))$$

where the constant K was 6.46 through a numerical integration for creeping flows at low shear rates; ν is the kinematic viscosity of the fluid; $\mathbf{U}$ and $\mathbf{U}_p$ are respectively the velocity vectors of the flow and of the particle. Thus this force depends on particle diameter and velocity gradient. In the region where a velocity gradient exists, for instance, near a wall or in a high shear region, this lift force would be considerable. The ratio of Saffman force to the Stokes drag, R_{SS}, is given [66]

$$R_{SS} = \frac{K}{12\pi}\sqrt{\mathrm{Re}_P}$$

If Re_P equals to 1, R_{SS} will be 0.17. Saffman force thus is not negligible because this value will be in the same order of the ratio of the velocity of secondary flow to the mainstream velocity.

However when applying this approach to the real problem of the tubular pinch effect shown in Fig. 2-8, Saffman theory still doesn't provide satisfactory results because when taking account the real parabolic velocity distribution and the wall effects in channel flows, the assumptions of Saffman force analysis discussed above are not satisfied. If the relative velocity is positive (as the particle A in Fig. 2-8), a Saffman force toward the higher velocity region will act on the particle. However the Saffman lift model doesn't explain the drift of particle B, where it should also point to the central area while in reality the lift force propels the particle away from central zone towards the lower velocity surrounding area of $r=0.6R$. This is because

Saffman's analysis is based on uniform simple shear flow, and on the assumption that both the Reynolds number defined by the relative velocity and the shear Reynolds number are much less than unity, and the former is much smaller than the latter: $\mathrm{Re}_r \ll \sqrt{\mathrm{Re}_G}$, where $\mathrm{Re}_G = \frac{d_P^2}{\nu}\frac{du}{dy}$. Particle A is in the near-wall region of Poiseuille flow where the assumption is easier to be satisfied whereas particle B is in the channel-centre region, where the assumption tends to be violated.

To explain fully the tubular pinch effect, several theoretical efforts have been reported. Correct prediction of the equilibrium radial position for a small sphere in a Poiseuille flow has been made for channel Reynolds number order of unity [78]. In the near-wall area, the flow field can be regarded as Stokes flow and the viscous effects are dominant. In the largest portion of the flow field, wall effects can be neglected, and the flow past the sphere can be treated as unbounded parabolic shear flow. The problem has been solved by addressing the governing equations adopting a perturbation method. For the case that the distance of the particle from the wall is small compared to the characteristic length, the regular perturbation technique can be used. However considering the region where the distance between the particle and the wall is of the order of particle dimension, the basic asymptotic parameter relating to particle Reynolds number Re_P or channel Reynolds number Re_C cannot be treated as a small parameter approaching to zero. It's a singular perturbation problem in which the high order perturbation terms in the problem are not negligible, thus the matched asymptotic expansion should be adopted. Briefly, this methodology can be outlined as

follows: the whole domain is divided into two subdomains. The first is the wall-bound area, where the distance of the particle from the wall is small compared with the length scale of the outer region. When the particle is located in this region, approximations are made and the problem degrades to be an *inner problem*. To solve the inner problem, the *inner solution* is approximated by an asymptotic series through standard perturbation techniques. By solving the governing equations of Stokes flow, the first-order inner solution and the expression of particle lateral velocity could be derived. The second subdomain is the area far from the wall, namely the outer region in which both viscosity and inertia are important. When the particle lies in this area, suitable approximations are also made to form the *outer problem*. By solving this outer problem, an *outer solution* is derived based on the equations governing the disturbance flow past a particle at small particle Reynolds numbers. Then the outer and inner solutions are combined through a matching process, in which the inner and outer solutions meet at the matching condition, so that an approximate solution for the whole domain is obtained. Asmolov [79] and McLaughlin [80, 81] respectively extended Saffman's analysis to a particle moving in a linear shear flow unbounded or bounded by a single wall. Corrections of the original Saffman force also have been made to allow the relative Reynolds number to exceed the shear Reynolds number. The lift force on the particle can be derived through considering the relation between the lateral migration velocity and the lateral drag force through Stokes' law. Following a similar routine of combining the inner solution of boundary layer flow and the outer solution of far region flow, Asmolov [82] obtained the theoretical solution of lift on

both neutrally and non-neutrally buoyant particles in a Poiseuille flow using the method of matched asymptotic expansions at small particle Reynolds number. The lift force on a neutrally buoyant particle along the radial direction of a tube under different Re_C is shown in Fig. 2-9. The lift force for neutrally buoyant is expressed as $\mathbf{F}_Z = G^2 r^4 c_{nb} \mathbf{e}_Z$, where G is the local shear rate; r the particle radius; $\mathbf{e}_Z$ is the radial unit vector; c_{nb} is a non-dimensional lift coefficient that is dependent on radial position Z and the channel Reynolds number Re_C. As c_{nb} would flip sign from positive to negative along the position as the particle changes from the wall to the centre of the channel, there is a position where $\mathbf{F}_Z = 0$. This reveals the particle balance position away from the centre. Along with the decrease of Re_C, the balance position converges to 0.6 of the radius of the channel away from the centre, which is exactly consistent with the Segre and Silberberg experiments.

These analyses offer an improved explanation for the Segre and Silberberg observations, because they not only can predict that particles near the wall will be repulsed from the wall but also explain why the particles at the central part are dispersed from the centre line. It's suggested that excluding the lift coefficient which is the function of particle position, the lift force is proportional to r^6 in the near-wall region in comparison to r^3 in the main flow [83]. In contrast, the original Saffman force model based on the linear shear flow assumption couldn't explain this because just a single equilibrium position, which is at the centre of the channel, could be predicted. This work also found in the thin layers near the walls the lift is close to that calculated for linear shear flow bounded by a single wall. With the increase of channel

Reynolds number, the equilibrium position is approaching the wall, shown in Fig. 2-9, where $\varepsilon = R_p^{\frac{1}{2}}$ is the main asymptotic parameter. The results suggest the curvature effect of the velocity profile is significant. The actual lift differs from the values corresponding to a linear shear flow bounded by a single wall for which there is no equilibrium position, shown in Fig. 2-10, where ζ_W is the dimensionless distance from the wall. Actually in this situation, the lift is positive for all positions, i.e. the particle always migrates away from the wall. Thus there is no equilibrium position for a particle in a linear shear flow bounded by a single wall.

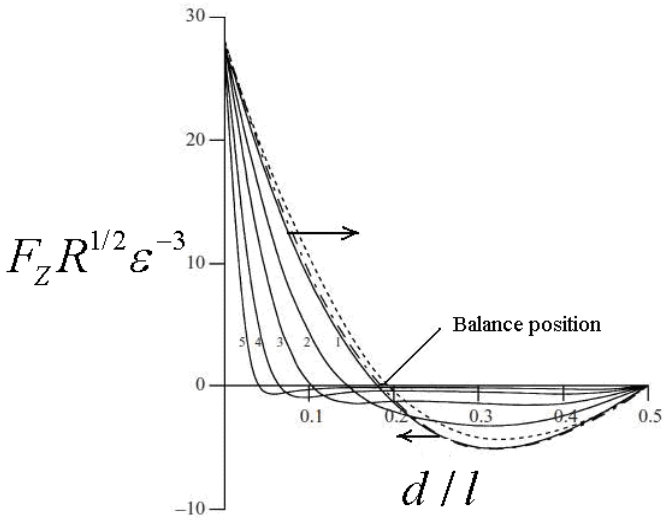

Fig. 2-9 Lift on a neutrally buoyant particle for Re_C=15, 100, 300, 1000, 3000 (curves 1-5) [82]

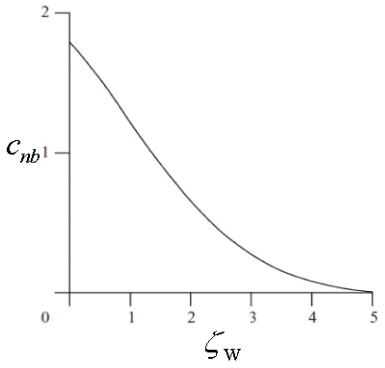

Fig. 2-10 Lift coefficient for a neutrally buoyant particle in a linear shear flow bounded by a single wall [82]

The theoretical analyses discussed above hold for a straight pipe (Poiseuille flow), is essentially an axisymmetric problem. For more complex geometries, like curved channels, the nonaxisymmetric walls may induce distinct phenomena. However before we address the problem of a curved channel, it's important to point out that the aforementioned analyses are based on the assumption that the particles are considerably smaller than the dimension of the channel, namely the "point-particle" or "point-force" approximation [78]. Particles with dimensions comparable to the flow length scales can no longer be treated as point particles. This can explain why in a 3-D rectangular cross-section microchannel, the tubular pinch effect remains but is transformed to another form. Di Carlo etc. [70] experimentally demonstrated 4 balance positions in a straight rectangular channel due to this lift force, shown in Fig. 2-11. Afterwards the majority of related research has been experimental or semi-empirical because the complexity of this problem does not lend to theoretical analysis. Only few computational approaches have been conducted, more recently. Di Carlo etc. [83] conducted steady simulations of particles located at different positions in a straight rectangular channel. However this study hasn't revealed the dynamic migration characteristics of microparticles. Lacking a validated lift force model for a finite sized particle, and a dynamic multiphase coupling technique, we need to develop a direct transient simulation approach solving the real velocity field coupled with the particle movement to unveil the effect of the lift force and discover the dynamic particle separation mechanism.

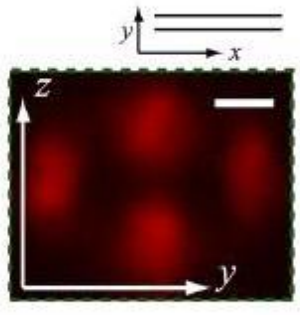

Fig. 2-11 Four particle balance poisons of a rectangular microchannel [70]

Particularly in narrow channels with low (or high) aspect ratio, the longer walls are taking a role of confinement which will impact much more intensively on the bigger particles and are more prominent to confine the bigger particles within two thin layers near and parallel to these longer walls [84], which is demonstrated in Fig. 2-12 (the widening of the microchannels is to improve visualization).

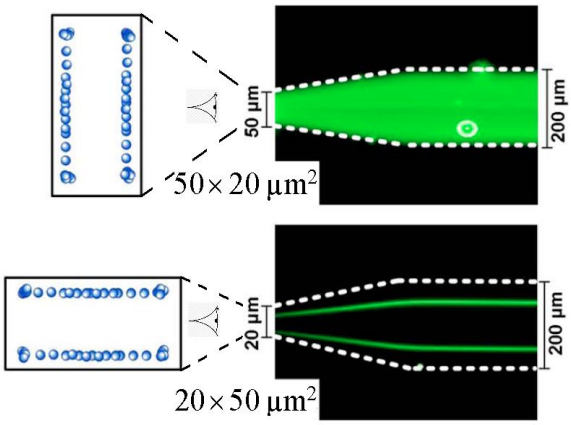

Fig. 2-12 Particles align along the longer walls in low and high aspect ratio microchannels due to the geometry's impact on the equilibrium position [84]

2.5 Particle in curved microchannels and Dean flow

2.5.1 Curved microchannel for particle manipulation

Curved channels are present in many practical industrial applications and in nature: turbomachinery blade passages, heat exchangers, aircraft intakes, meandering rivers,

blood vessels etc. Compared to straight channels, curved channels provide compactness, high mass and heat transfer efficiency as well as a broader regime for laminar flow. In biomedical engineering, curved channels also plays a crucial role, especially in blood flow and blood cellular component analysis [85]. Along with the development of microfabrication, microfluidics and lab-on-a-chip (LOC) devices are in high demand and investigated very intensely. This technology points out a promising way for detecting and separating of microparticles. Previous research demonstrated that particles could be focused at a single equilibrium outlet position by adopting a microchannel system consisting of curved channels, which is evidence for the potential first-step application in high-throughput cytometry, and continuous bioparticle separation. Although there isn't convincing theory to explain why the particles would focus at the balance positions through a straight rectangular channel, further experiments of particles in curved channels have been conducted, which lead to more surprising outcomes. It is demonstrated that the symmetric curved channel and the asymmetric curved system focus the micro particles into single or double equilibrium positions under different particle Reynolds numbers [70], shown in Fig. 2-13. After flowing through a channel of a particular symmetry, precise ordering of initially scattered particles is observed to line longitudinally along the direction of flow and focus laterally across the channel, which is shown in Fig. 2-13 a and c. The streams of particles will focus to a single position through drifting. For an asymmetric curving system, as Dean number[4] increases, the particles would firstly focus to a

[4] A parameter we shall define and discuss extensively in the sequel.

single stream and then again diverge to two, shown in Fig. 2-13 d.

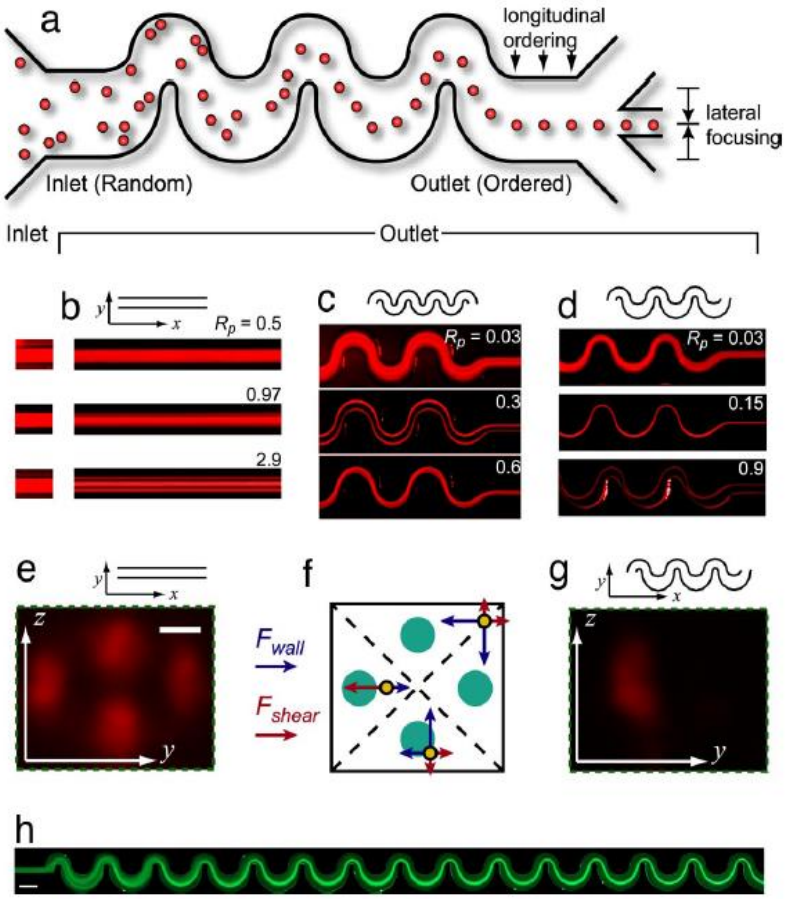

Fig. 2-13 Inertial focusing in rectangular micro channels [86]

Yoon *et al.* [87] fabricated a 180° curved rectangular microchannel and showed the size-selective separation and sorting of micro beads. The fabricated microchannel is shown in Fig. 2-14. Various curved micro-channels have been proposed for particle separation [88-90].

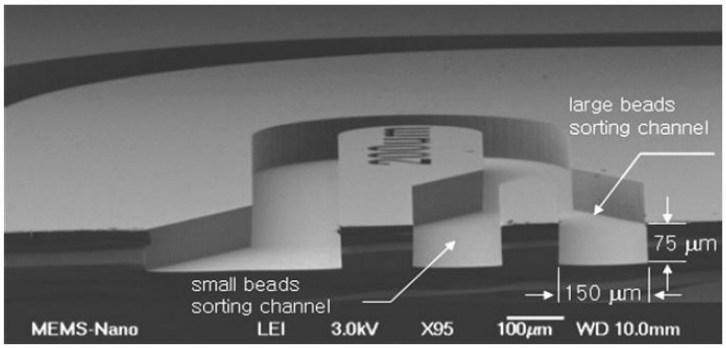

Fig. 2-14 SEM image of the fabricated curved rectangular microchannel [87]

Bhagat *et al.* [91] adopted a spiral microfluidic design to achieve particle focusing, shown in Fig. 2-15 (A) with fluorescent imaging. Other works [92-94] adopted spiral microchannels for size-dependant particle separation and showed that different-sized micro particles have distinct equilibrium positions, which could be collected in separate outputs.

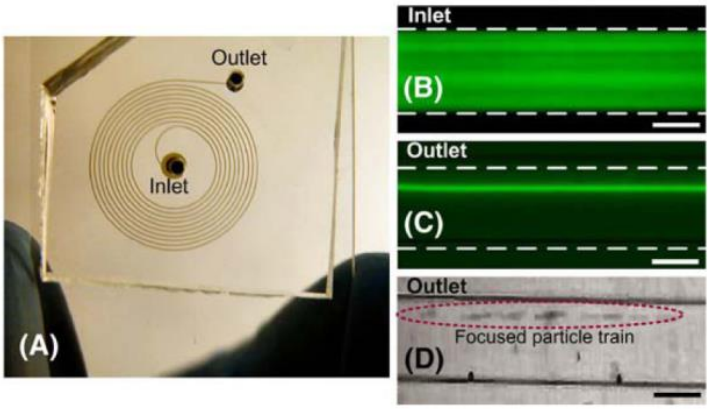

Fig. 2-15 Spiral microchannel for miroparticle focusing [91]

It is known that the flow inside curved channels is usually characterized by a pair of counter-rotating symmetric vortices dominating the secondary flow. Fig. 2-16 (a) shows the general form of the secondary flow in curved rectangular channels from computational work [95] , where only the lower half section is shown since the solution is symmetric. Dean [1] first gave the solution of the flow in curved pipes, demonstrating the existence of secondary flow. He also adopted perturbation analysis for the viscous Newtonian pressure-driven flow in curved channels [96], with the assumption of infinitesimal curvature ratio, $r = a / R_1$, where a is the width of the channel cross-section and R_1 the radius of inner curved wall. In the same paper, it is

demonstrated that if a non-dimensional number, the Dean number, exceeds a specific value of 36 for this infinitesimal curvature ratio channel, an instability in the solution emerges. This type of threshold value points to a minimum Dean number for secondary flow to occur. This kind of instability problem is called Dean instability and the flow through a curved channel with secondary flow is called Dean flow. Several studies have looked at developed laminar Newtonian flow in curved pipes (i.e. conduits with circular cross-section) [97, 98]. Typical results of such studies are shown in Fig. 2-16 (b), where the secondary streamlines and contours of axial velocity for the curved pipe are evident. In that figure, 'I' denotes inner bend, 'O' refers to outer bend and 'D' is Dean number. However, in terms of fabrication efficiency and geometry flexibility, curved channels with rectangular cross-section are superior – much easier to build and with much better size and precision control. Hence this type of geometry constitutes the focus of this work.

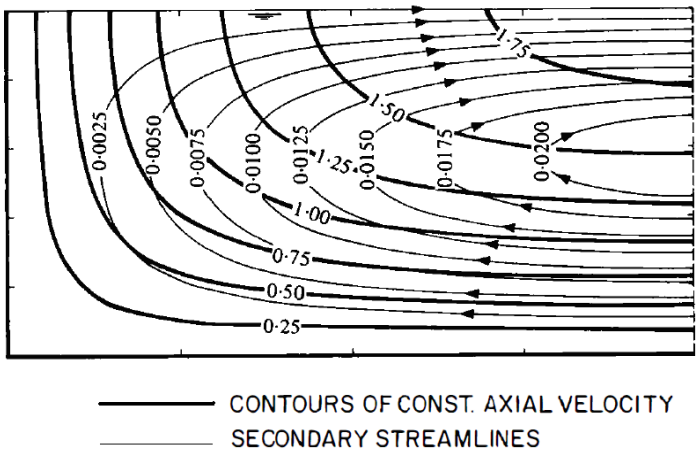

(a) rectangular channel [95]

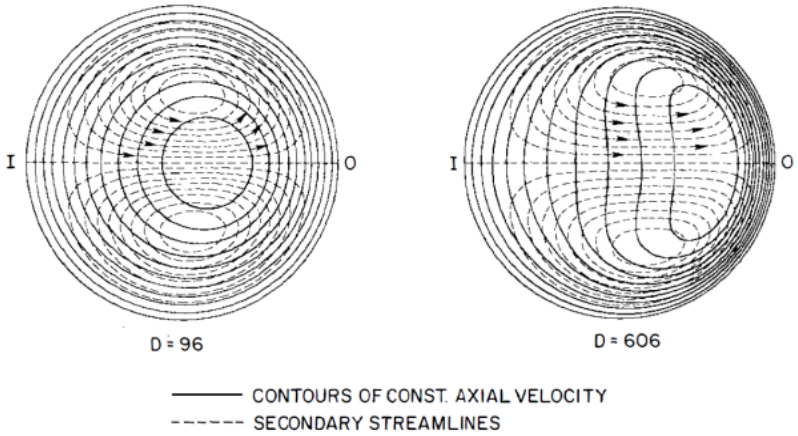

(b) circular pipe [98]

Fig. 2-16 Secondary streamlines and axial-velocity of flows in curved channel.

Research to date about curved conduits can be mainly divided into 3 categories: analytical [96, 99, 100], experimental [101-104] and computational [104-108] studies. Before discussing of characteristics of Dean flow and the scientific problems in the area, the important definition of Dean number should be introduced.

2.5.2 Dean number

There are several different expressions suggested regarding this important quantity, that often cause misunderstanding and confusion in interpretation [98]. The original definition adopted in Dean's work [96] is $De = (\frac{a}{R_1})^{\frac{1}{2}} \mathrm{Re}$, where a is the distance between the two cylindrical wall sections (the two walls, i.e. the "width" of the passage), R_1 is the radius of inner curved wall and Re denotes the Reynolds number, which is an important dimensionless number that represents the ratio of inertial forces to viscous forces – $\mathrm{Re} = \frac{VL}{\nu}$, V is the mean fluid velocity; L is the characteristic dimension; ν is the kinematic viscosity. But since then, numerous works adopted variants of this expression. Berger *et al.* [98] suggested $De = (\frac{a}{R})^{\frac{1}{2}} (\frac{2a\nu}{\nu})$, where a is

the radius of the circular cross-section, R denotes the radius of the curved pipe's centre line. Other definitions are presented here: $De = (\frac{D}{R})^{\frac{1}{2}} \mathrm{Re}$, where D represents the inner diameter of the micro-tube and R is the radius of curvature [103] ; $De = (\frac{D_h}{2R})^{0.5} \mathrm{Re}$, where D_h is the hydraulic diameter of microchannel with rectangular cross-section [92]. $D_h = \frac{4A}{P}$. For a rectangular duct, $D_h = \frac{2ab}{a+b}$. In the present work, the more generally accepted form [87, 104, 109, 110] of the Dean number for rectangular curved channels is adopted, as $De = (\frac{D_h}{R_c})^{0.5} \mathrm{Re}$, where R_c is the mean curvature radius. Dean number has a significant physical meaning ,which is the ratio of square root of the product of inertia and centrifugal forces to viscous forces [98]. Because the secondary flow is generated by interaction of centrifugal force and viscous force, Dean number is regarded as a measure of magnitude of the secondary flow. For a channel with fixed cross-sectional shape (radius for a circular pipe; aspect ratio for a rectangular channel), Dean number takes account of both flow velocity and the curvature ratio of the channel, thus it offers a more insightful description of the curved channel induced flows.

The threshold Dean number for secondary flow to occur is zero for the curved rectangular channel with finite aspect ratio [111], which indicates that inside a curved channel of this type, there are always vortices. As the Dean number increases, related research has followed three different tracks [98]. For small Dean numbers, the perturbation method has been applied and demonstrated to be valid for this problem. For intermediate Dean numbers and large Dean numbers, the boundary layer concept

is applicable and the assumption is made that the viscous effect is concentrated in thin layers and the flow outside the boundary layers is inviscid. These assumptions put limits on the validity of such analytical investigation. Along with the improvement in the field of computational fluids dynamics (CFD), more numerical solutions for developed laminar flow in curved rectangular channels have been conducted and predicted the secondary flow and detailed flow field.

1. The stability problem

The inertia of the flow and the curvature of the channel induce a centrifugal force outward from the inner wall (convex wall) to the outer wall (concave wall). However, there is a positive pressure gradient in the same direction, thus the pressure near the outer wall is higher than the inner wall. The imbalance between the centrifugal force and the pressure gradient becomes the cause of the secondary flow which results in a pair of counter-rotating symmetrical vortices. Beyond a critical value of Dean number, $D_{e-critical}$, another pair of vortices shows up near the outer wall of the channel, which is called Dean vortices. The first and second pair of vortices seem similar in the terms of their formation with the increase of D_e. However, their mechanisms are distinct. The first pair of vortices are caused by the imbalance between the centrifugal force, pressure gradient and viscous force. They are always near the upper and lower end walls. But the Dean vortices are due to the Dean instability mechanism. They appear near the centre of the outer wall. The Dean instability is just one kind of centrifugal instability, which also includes the instability of Taylor-Couette flow [104]. With Dean number increasing, the radial positive pressure gradient and the

centrifugal force increase dramatically. The flow system approaches a point where the imbalance of the radial pressure gradient and the centrifugal force becomes unstable. At that critical point, the second pair of vortices emerges [112]. Fig. 2-17 demonstrates the development of these structures with increasing Dean number [101].

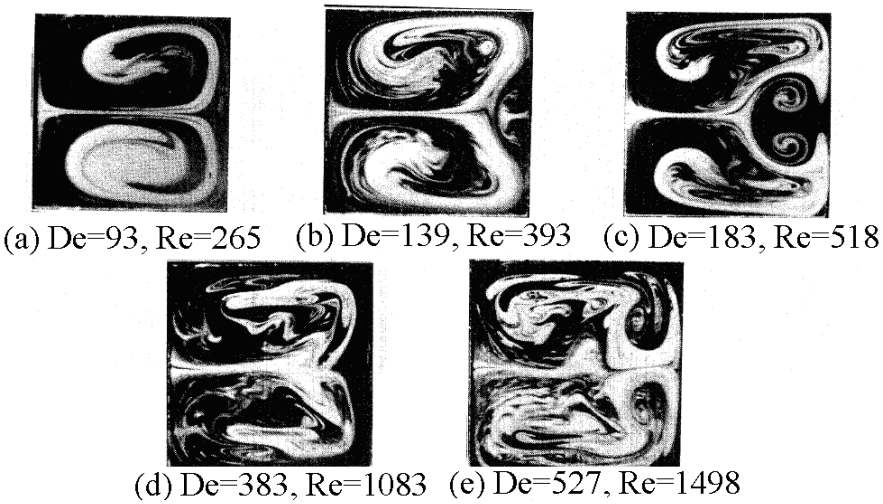

Fig. 2-17 The generation of Dean vortices in a curved channel with square cross-section [101]

Numerous works have demonstrated the second vortex pair and intensively investigated the instability problem. Reid [99] took two methods of approximation solutions to confirm the critical Dean number (about 36) suggested by Dean [96]. Brewster *et al.* [100] analytically investigated more extended cases. Balis [113], Mori *et al.* [114] and Humphrey *et al.* [115] gave experimental results of the flow through curved square ducts and described the structure of the secondary flow. Hille *et al.* [116] investigated the development of laminar flow in a 180° section of a curved square duct by laser-Doppler anemometry (LDA). Ligrani *et al.* [117] showed the results of Dean vortex over a range of Dean number from 40 to 220, using a transparent channel with curvature ratio 40. Joseph [118] gave numerical solutions of

steady laminar flow in curved channels of square cross section and reported that above Dean number of 100, a new secondary flow appears. Thangam *et al.* [119] adopted a finite volume method to study the secondary flow in a curved duct and showed 'roll cells', namely the Dean vortices. It was suggested that for curved channels with high curvature the Dean instability depends on the Dean number and the curvature ratio, while for small curvature channels the onset of the Dean instability is only decided by the Dean number. Fellouah *et al.* [104, 109] systematically investigated the criterion for onset of the Dean instability in Newtonian fluids and provided a criterion based on the radial gradient of the axial velocity which was suggested to be more accurate than the visualization criterion. That work also showed that other factors, like curvature ratio and aspect ratio of the curved channel, play a considerable role on the Dean instability. Targett *et al.* [120] adopted a numerical method for large and infinite aspect ratio with small radius ratio of 0.05. The results showed that for infinite aspect ratio channels, the critical Dean number is 37.31, above which pairs of counter rotating vortices would occur. For large but finite aspect ratios a weak secondary motion is found to occur below the critical Dean number.

For the criterion of detection of the onset of Dean instability, most published papers use the visualization of the second pair of vortices which is a qualitative criterion. The visualization technique depends strongly on the accuracy and sensitivity of the equipment in the experimental investigation; also, as far as numerical work is concerned, it relates considerably to the grid density or the iso-value contour lines

selected. Fellouah *et al.* [104, 109] suggested a quantitative criterion of measuring the radial gradient of the axial velocity which is claimed to be more accurate and reliable. The method is firstly locating the centre of the Dean vortices for a Dean number large enough and then decreasing the Dean number gradually until the Dean vortices disappear. It is found that for low Dean numbers (only with the first pair of corner vortices) a double-peak of the radial gradient of the axial velocity occurs, namely the slope of the gradient turns three times; for high Dean numbers (with the Dean vortices appearing) a triple-peak radial gradient of the axial velocity shows up, where the slope turns five times. The radial gradient of the axial velocity is shown in Fig. 2-18 [104]. Other measurements, like the shear stress on the concave wall, are limited for the stress could only be detectable when the Dean vortices have developed sufficiently.

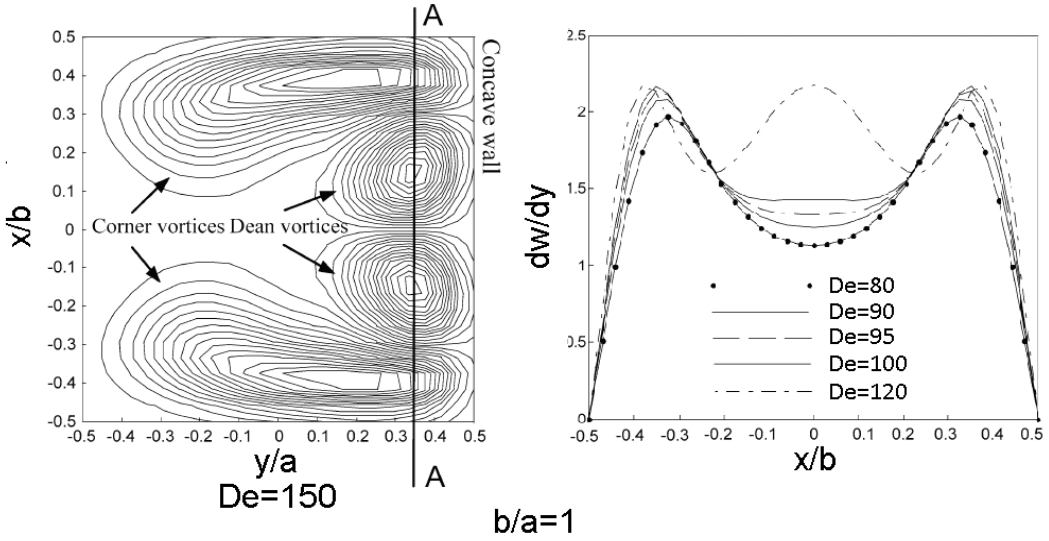

Fig. 2-18 Radial gradient of axial velocity along the centres of Dean vortices [104]

At the early state of the research on Dean flow, the Dean number was regarded as the primary control parameter. But this hypothesis is not necessarily valid. More and more studies suggested there are several factors influencing the Dean instability, in

which the important ones are curvature ratio, aspect ratio and the characteristics of the fluids, etc. They are discussed as follows.

(1) Curvature ratio

Although the curvature effects are contained in the Dean number, with the increasing of the channel curvature, it is found that the instability in channels with high curvature is controlled by the Dean number as well as the curvature ratio itself [104, 109, 119]. The results of these studies are summarized in Fig. 2-19 (a) [104]. Here, the curvature ratio is $r = R_c / D_h$, where D_h is the hydraulic diameter and R_c indicates the mean curvature radius. With the curvature ratio increasing to about 10, the critical Dean number decreases dramatically and then approaches a constant value. In other words, if we increase the curvature of the channel, the critical Dean number will increase, indicating that the instability is more difficult to emerge in highly-bending channels. The explanation for this is that the axial curved length is shorter at the same axial angular position for the channels with higher curvature than that of channels with lower curvature. For the smaller axial curved length, a higher centrifugal force is needed to form Dean vortices. The secondary velocity component profile is also reported, showing with the curvature of the channel increasing, both the maximum peak value of the secondary velocity component and the width of peak increases, as in Fig. 2-19 (b) [104]. This indicates that the increasing of the curvature of the curved channel will lead to strengthening and enlargement of the span of the corner vortices.

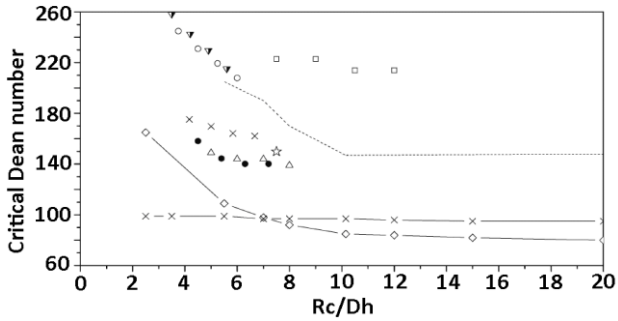

Fig. 2-19 (a) Effect of curvature ratio of curved channel with different aspect ratio on the Dean instability [104]

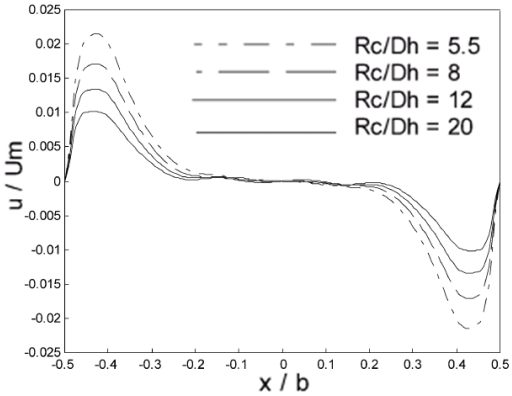

(b) Effect of curvature ratio on secondary velocity component distribution on mid-curve plane [104]

(2) Aspect ratio

For a curved channel with infinite aspect ratio and gap-to-inner radius ratio of 0.05, Targett *et al.* [120] found the threshold Dean number for vortices to appear is 37.31, under which no obvious secondary motion was shown. For large but finite aspect ratios, they also reported critical Dean numbers for different aspect ratios. In a more general framework, both experimental work [101] and numerical work [104, 109] have summarized the effect of aspect ratio on the Dean instability, which is shown in Fig. 2-20 (a). There is a local minimum of the critical Dean number at about aspect ratio $n = b/a = 1$, where b is the channel height and a is the channel width, namely the square cross section. In a general view, for n ranging from 1 to 4, the critical

Dean number increases to a local maximum. Beyond $n = 4$, the critical Dean number decreases and reaches a constant value at around $n = 8$. These results could be explained by the interaction between the secondary flow strength and the channel confinement effect. Increasing the aspect ratio will decrease the relative transverse flow length, which makes the Dean instability harder to appear. But increasing the aspect ratio will also decrease the vertical confinement effect because the Dean vortices have more space and find it easier to expand. These two opposite sides lead to a behaviour where the critical Dean number vs aspect ratio is not monotonical for the same channel. For the shallow channel ($n < 1$), the confinement effect dominates hence the secondary flow is harder to appear, leading to the increasing of the critical number. For the intermediate channel ($1 < n < 8$), both effects are working: for $1 < n < 4$ the secondary flow effects dominates thus the critical Dean number increases with aspect ratio; for $4 < n < 8$, the confinement effects dominate hence the critical Dean number decreases. For the deep channel ($n > 8$), the influence of the upper and lower walls is relatively small, so the critical Dean number decreases smoothly and approaches a constant, which indicates that it does not dependent on aspect ratio any more [104].

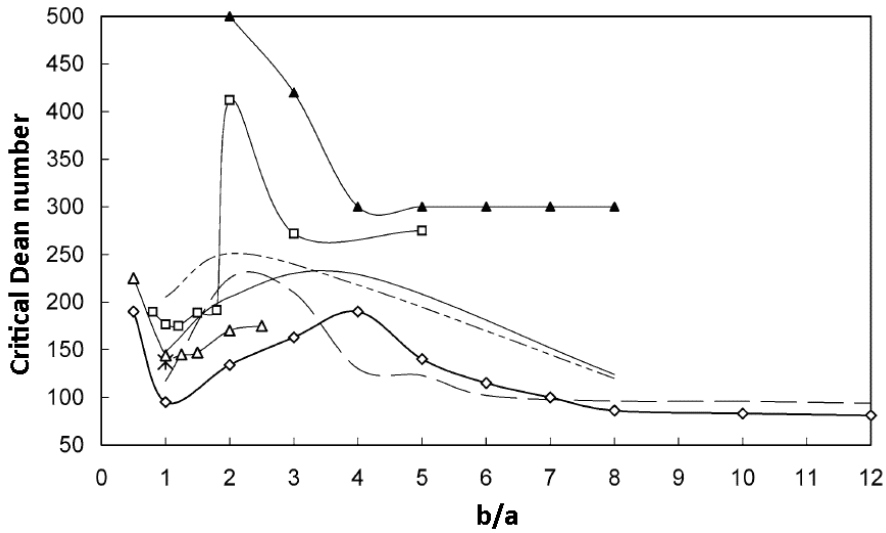

Fig. 2-20 (a) Effect of aspect ratio on Dean instability [104]

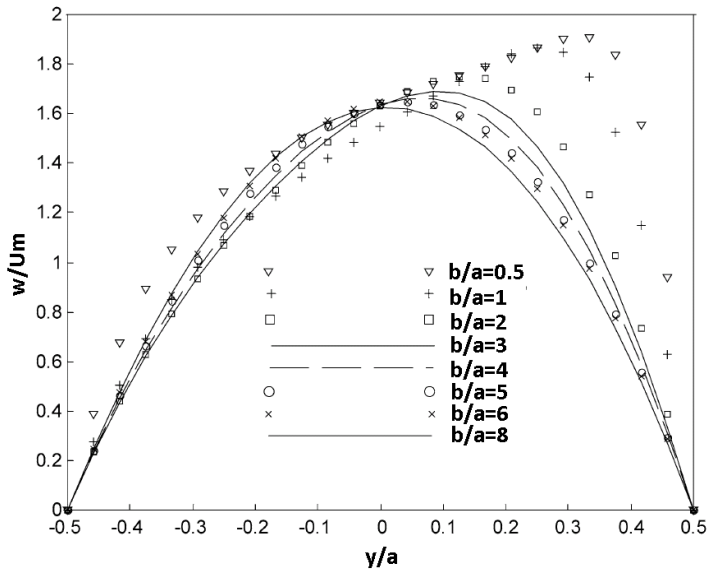

(b) Effect of aspect ratio on axial velocity profiles on the horizontal mid plane [104]

Fig. 2-20 (b) shows the different axial velocity profiles on the horizontal mid-plane at the exit of a 180° curved channel with $D_e = 55$. It shows that with the aspect ratio increasing, the peak of the axial velocity is moving from the position near the outer wall to the vertical centre line of channel cross section. In the meanwhile the maximum velocity is decreasing, which clearly demonstrates the confinement effect.

(3) Fluid properties

The fluid characteristics are also reported to have a considerable influence on Dean flow [107, 109]. Fellouah [109] presented the numerical solutions of the Dean flow for a power-law fluid and for a Bingham fluid. It shows that the critical Dean number decreases with increasing of power-law index, while the critical Dean number increases with the increasing of Bingham number. The results are shown in Fig. 2-21 (a) and (b).

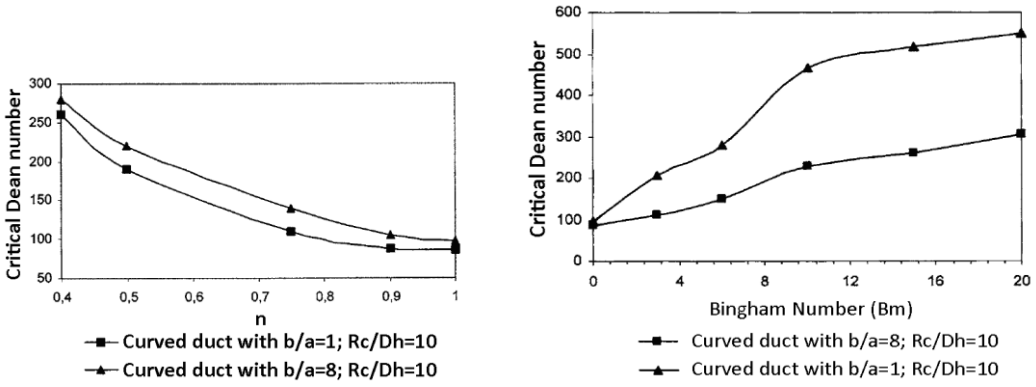

(a) (b)

Fig. 2-21 (a) Effect of power-law index on the onset of instability [109] (b) Effect of Bingham number on the onset of instability [109]

A power-law fluid is a type of non-Newtonian fluid of which the shear stress is given by $\tau = K(\frac{\partial u}{\partial y})^n$, where K is the flow consistency index, $\frac{\partial u}{\partial y}$ is the shear rate or the velocity gradient perpendicular to the plane of shear, and n is the flow behaviour index which is dimensionless. A Bingham fluid has the characteristic of Bingham plastic which behaves as a solid body at low stresses but flows as a viscous fluid at high stress and the Bingham number denotes the ratio of yield stress to viscous stress.

(4) Angular position

Along with the angular position downstream the centerline, the Dean flow develops

gradually to reach the criterion of instability [104]. The trend is shown in Fig. 2-22.

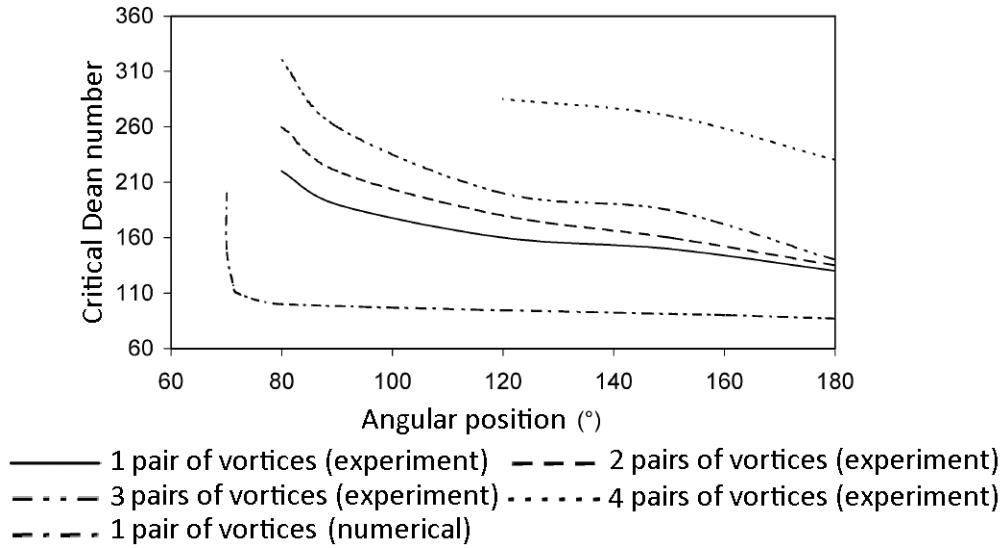

Fig. 2-22 The angular position on the detection of critical Dean number [104]

With Reynolds number further increasing, the Dean flow could become time-dependent and two distinct types of travelling wave flows arise: undulating and twisting Dean vortex flow [121], which are unstable and non-symmetric, shown in the Fig. 2-23 (a) and Fig. 2-23 (b). We would focus on steady state flows in this study, therefore we shall not expand as far as time-dependent flows are concerned.

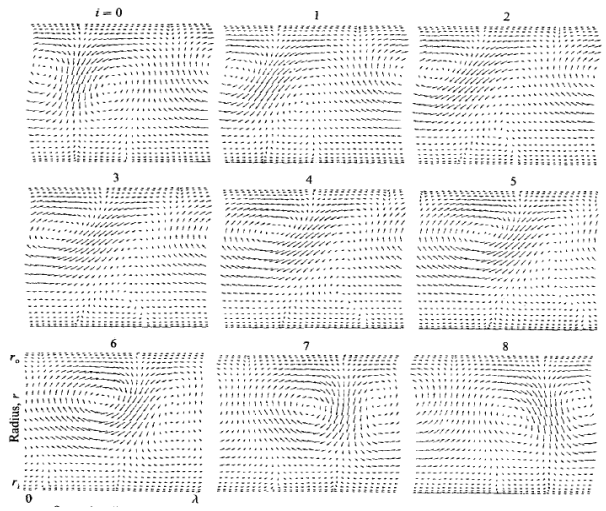

(a) Undulating Dean vortices

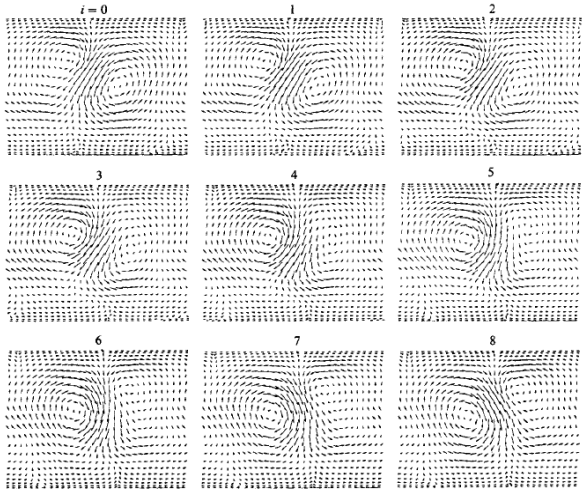

(b) Twisting Dean vortices

Fig. 2-23 Travelling wave flows [121]

2.5.3 The flow field and velocity distribution in Dean flow

The Dean instability problem presents the Dean vortices structure which is necessary for us to understand the whole flow field and the velocity distribution. Generally, the flow field of the Dean flow depends on several factors: the Dean number, the curvature ratio, the aspect ratio, the fluid characteristics as well as the velocity profile at the inlet boundary. Among them, the Dean number is the characteristic number, playing a key role in controlling the flow field. Fig. 2-24 (a) and Fig. 2-24 (b) represent the axial velocity profile on the horizontal mid-plane and the vertical mid-plane of curved square channels for the Dean number ranging from 0-100 and 60-350 respectively [104, 111]. With the increase of Dean number, the peak of the axial velocity profile firstly moves toward the outer wall, namely the concave wall, indicating a transfer of axial momentum from the centre of the channel to the concave wall, which is shown in Fig. 2-24 (a). Thus the centrifugal force takes the effect of shifting the location of the maximum axial velocity toward the outer wall and

decreasing the maximum value, as the Dean number increases. As the transfer becomes stronger, the imbalance of the centrifugal force and the pressure gradient causes the Dean instability, inducing the formation of the Dean vortices. The Dean vortices transport fluid from the inner wall to the outer wall which will obviously lead to a shift of the velocity peak value from the convex wall to the concave wall, until $De = 300$, which is demonstrated in Fig. 2-24. However the peak value of the axial velocity is continuously decreasing, indicating that the mainstream is transferring more and more momentum of fluid to the secondary flow. The axial velocity profile on a vertical line is turning from parabolic to double-peak type, which corresponds to formation of the first pair of vortices. The two peaks correspond to the centres of the two corner vortices and move toward the upper or lower walls. For $De \geq 300$, the peak shifts to the inner wall again since the appearance of the second pair of vortices push the first pair away from the outer wall. The vertical velocity profile becomes three-peak and then decreases to be flat, indicating the formation of the second pair of vortices and its mixing with the rest flow, shown in Fig. 2-24 (b). Here, $De = 300$ is not a critical number but case-dependent.

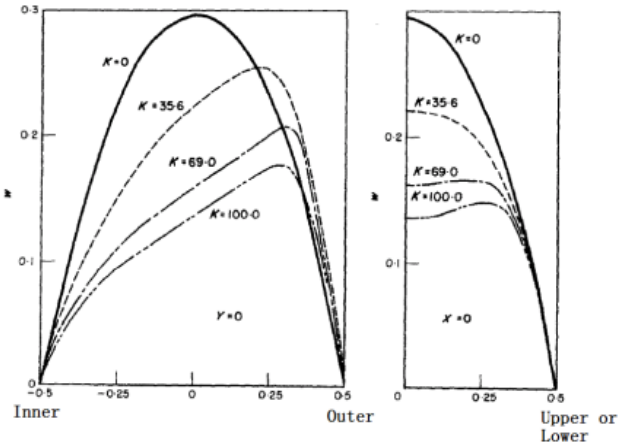

(a) [111]

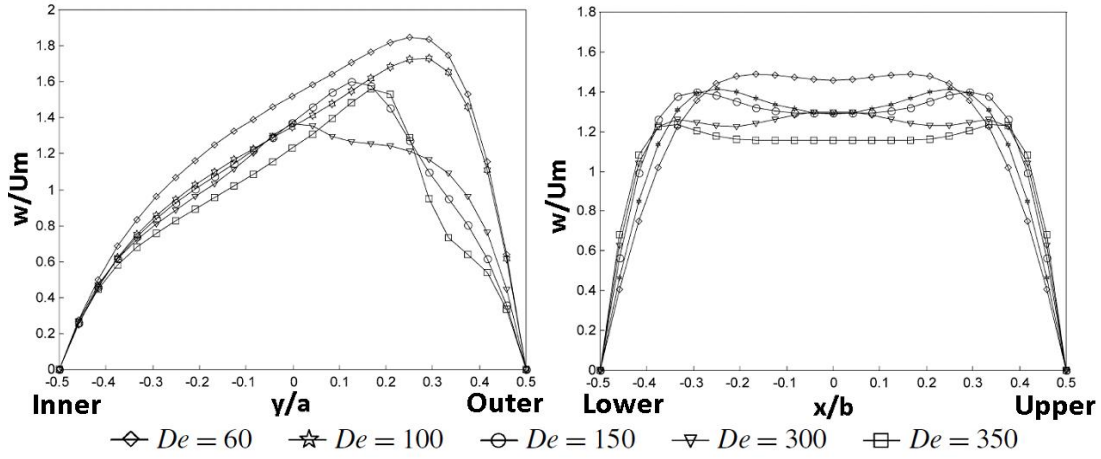

(b) [104]

Fig. 2-24 Axial velocity profile on the horizontal mid-plane and the vertical mid-plane of a square cross section channel

Fig. 2-25 shows the secondary velocity components on the vertical mid-plane with Dean number increasing for a square cross section channel [104]. For the Dean number from 60 to 100, the two peaks move towards the flat walls indicating the centres of the corner vortices move apart from the centre of the channel. In the same range of Dean number, the horizontal velocity component only has one positive peak. When $D_e \geq 150$ two additional peaks appear in the vertical velocity profile and the number of positive peaks increase to two due to the onset of the Dean instability.

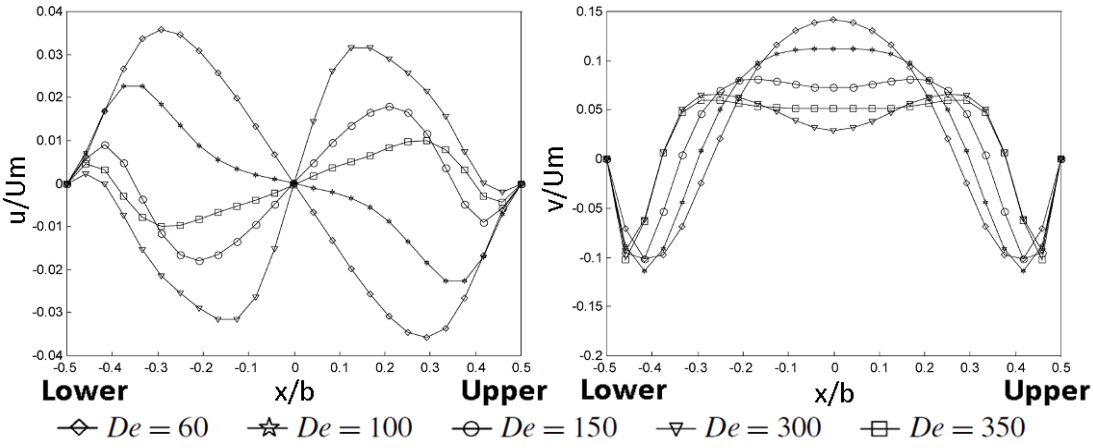

Fig. 2-25 The secondary velocity components on vertical mid-plane in a square - section channel [104], *v* is vertical component, *u* is horizontal component

The location of the centre of circulation along with De increasing is also studied in the interest of investigating the secondary flow pattern [111]. Fig. 2-26 (a) shows that the centre of circulation moves from the centre to the outer wall firstly and then moves back to the centre line of the channel in the horizontal direction. The centre of circulation in the vertical direction moves toward the upper or lower wall continuously indicating that the Dean vortices compress and "crush" the corner vortices to the flat walls and increase the intensity of secondary flow near the upper or lower walls. This is in good agreement with Fig. 2-24.

It should be noticed that the aspect ratio also plays a key role for the Dean flow velocity distribution. Fig. 2-26 (b) shows a different axial velocity distribution for the aspect ratio $n = b/a = 8$ when comparing to Fig. 2-24 (a) and (b) where $n = 1$. The peak of the profile is firstly moving toward the inner wall gradually but then shifted to the outer wall at higher Dean number.

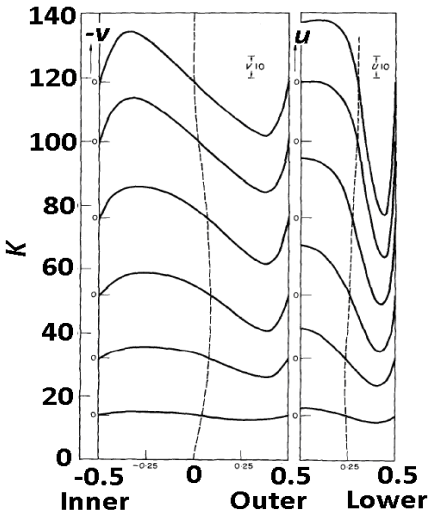

(a)

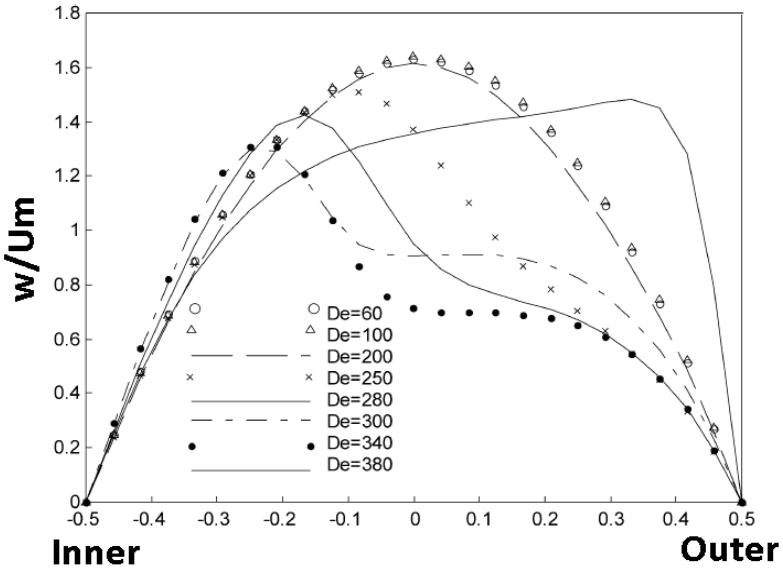

(b)

Fig. 2-26 (a) Distribution of secondary velocity components in two directions at the centre of vortex in a square cross section channel [111]
(b) Axial velocity profile on the horizontal mid-plane of a square cross section channel with the aspect ratio b/a=8 [104]

To summarize, both the flow pattern and the flow velocity distribution of the Dean flow vary evidently with different Dean numbers, the curvature ratio and aspect ratio. As discussed before, we intend to use these emergent fluidic patterns to induce and control separation of particles, via particle size-dependent loading, originating from local shear. This complexity offers significant potential for control and design options, but also poses substantial problems and grounds for research.

2.6 Simulation of particle-flow coupling

Due to the small dominant characteristic length scale, the flows in microfluidic systems are mostly laminar. However distinctive phenomena have been observed in fluids of such scales, which make microfluidics an area of great importance for research. Complicated three-dimensional geometries and large particles with

dimensions comparable to those of the microchannels are the most important issues of microfluidic devices [2].

With Computational Fluid Dynamics (CFD), the flows in various microchannels can be solved numerically. However further research is needed for movement of large-scale particles inside such microchannels. Generally, 2 categories of forces are controlling the movement of a particle in a fluid: (1) forces through the interface between fluid and particles, e.g. drag force, pressure force, lift force etc.; (2) forces imposed by external fields, e.g. gravity, electric field or magnetic field.

To study numerically particle-fluid interactions, there are two major approaches: the two fluid (Eulerian) approach [122] and the trajectory (Lagrangian) approach [73]. The two fluid [123] approach is suitable for problems in which the particle phase is evenly distributed, and the particles are numerous and very small. In our case, particle sizes can – in certain cases – be comparable to the channel dimension (see discussion in Chapter 1) so obviously the particles phase is not evenly distributed. On the other hand, traditional trajectory approach [124] is based on the point-particle approximation, including: volume-averaged models [125] and discrete element methods (or discrete particle methods) [126]. However for big particles, point-particle models cannot take the volume or shape of large-scale particle into account. In recent years, for large-scale particle simulations multi-domain and single domain methods have been proposed. In the multi-domain method, also called overset mesh or *chimera* method [127, 128], a sub-mesh domain is built covering an individual particle and the grid of background domain is overlapping with the particle mesh domain. The

information is exchanged between these two sets of meshes, shown in Fig. 2-27. However when the particles migrate close to each other or to the boundary walls, the overset mesh scheme is fraught with problems. Single domain methods, including body fitted methods, fictitious domain methods and Immersed Boundary methods etc., have shown potential for simulation of large-scale particle-fluid coupling. In body fitted methods, Hu et al. [129] developed the arbitrary Lagrangian–Eulerian (ALE) moving unstructured finite-element mesh technique for direct simulations of fluid-solid systems. Unstructured meshes are easier to generate to conform to complex geometries, but it has to be generated iteratively and involve the projection/interpolation of information from the previous grid to the new grid, which can have adverse effects on computational robustness and cost. The grid quality cannot be guaranteed as well with the increasing complexity of geometries. Fictitious domain methods [130] and the immersed boundary methods [131, 132] can both adopt structured grids. However, particular extra treatments are needed in these approaches. The fictitious domain method requires substantial mathematical efforts to convert the domain to a simple one, while in immersed boundary methods a forcing function that represent the effect of the solid particle to the flow is adopted. Other techniques involve adopting body-force terms to implement constraints acting on the fluid, such as the Eulerian-Lagrangian method [133] and the force coupling method [134].

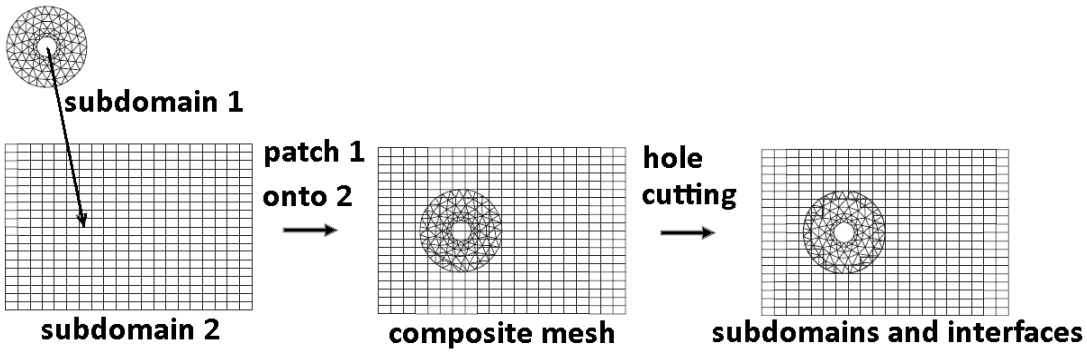

Fig. 2-27 Chimera method [135]

It is decided not to describe, to any extend, the numerous computational methods that form the background of any particle-flow coupling technique, i.e. the core methodologies for solving the governing equations of continuous transport phenomena (momentum, mass, species and energy), since this literature is now very mature and there are numerous excellent volumes that outline both the various techniques, but also describe specific techniques to a great detail. The reader is referred to [136] for a description that is of substantial breadth, but also presents the *control volume approach* specifics utilized in this study. The next chapter is dedicated to a description of the methodology used, together with a detailed presentation of the new contributions this study has made to challenging numerical facets of the particle-flow coupling aspects of the method.

3. Numerical methods

To investigate particle movement and separation mechanisms in microfluidic channels, the computational simulation approach offers cost and turnaround time benefits, since it allows to explore and possibly eliminate numerous preliminary designs. In result, the manufacturing and testing of a host of competing microchannels or processes can be partially replaced with modeling. Moreover, the detail and specificity that simulation offers can help explore complicated physical mechanisms and reveal features of scientific and practical interest. We pursue an approach which, beyond known point-particle coupling approximations, allows us to probe the physics and interaction dynamics of this system to a very high degree of specificity, accuracy and resolution. This chapter introduces the numerical method - CFD (based on the finite volume method), Surface Marker Point method and our approaches for fluid-particle coupling.

3.1 Governing Equations

After experimental and theoretical fluid dynamics, Computational Fluid Dynamics (CFD) emerged as the 'third approach' in the study and research of the whole discipline of fluid mechanics [137]. With the development of high-speed computers as well as advances in numerical algorithms, CFD turns out to be a new mighty tool for solving problems involving fluid flow. From oceanography to aeronautics, from modern vehicle design to turbomachinery, a wide range of disciplines and engineering applications are promoted by CFD to a degree that it is nowadays regarded as an equal to pure theory and pure experiment in the solution and analysis of fluid dynamic problems. In fact, CFD is playing an ever-increasing role as a research and design tool, as well as helping to interpret and understand the results of theory and experiment, and vice versa.

In comparison with the experimental approach, CFD could break through the limitation of reality, saving huge amount of resources, like the wind tunnels for aerospace research, the models for turbomachinery experiments, etc. Comparing with the theoretical approach, it overcomes the well-known issue of lack of analytical solutions for many (most) practical interest cases, which are often too complex geometrically. CFD also gives us more detailed features of the flow field, in a more direct way. For the present work, to investigate the complex Dean flow, which is dependent on the Dean number, the curvature ratio and aspect ratio, CFD is no doubt a valuable tool, providing a systematic view without the need to manufacture endless experimental apparatuses. Moreover, given that the target of this study is to

investigate separation of particles in microchannels, an additional strength of computational investigation is brought forward for complex systems, since miniaturization gives rise to numerous problems as far as experimental investigation is concerned (resolution, manipulation, field of view etc.). Small scale computational models can be set-up with no more difficulty than macroscopic ones and can provide detail of information that is difficult, if not impossible, to match in an experiment.

However, to work with CFD, a solid background in both fluid mechanics and numerical analysis is needed [138]. Similar to the theoretical approach, CFD analysis firstly represents the fluid flow problems by physical models. Then these physical models should be interpreted as mathematical models by establishing the governing equations as well as the boundary and initial conditions. To analyze these equations is to deliver the solutions of the independent variables, like the velocity components and the pressure throughout the flow field. Different from theoretical analysis, to obtain an approximate solution numerically, CFD adopts a discretization method which substitutes the differential governing equations by a series of algebraic equations which can be then solved on the computer. In general, for mesh-based methods, the discretization process divides the whole domain into small sub-domains in space and time, so the solution derived above is actually a numerical solution which applies to discrete locations [138]. The accuracy of the solution thus is dependent on the quality and fineness of discretization, amongst other things.

The fundamental equations of fluid flow are derived from the basic physical principles:

a. Mass is conserved

b. Newton's second law: $\mathbf{F} = m\mathbf{a}$ which implies that momentum is conserved

c. Energy is conserved

Thus the system of equations includes continuity, momentum and energy equations respectively.

3.1.1 The Continuity Equation

Continuity follows the physical principle of mass conversation. The derivation of this equation considers the mass flowing into and out of a control volume (CV) element. In Cartesian coordinate system, the equation is expressed as:

$$\frac{\partial \rho}{\partial t} + \frac{\partial (\rho u)}{\partial x} + \frac{\partial (\rho v)}{\partial y} + \frac{\partial (\rho w)}{\partial z} = 0 \tag{3.1}$$

where ρ is the local density; u, v, w are the velocity components.

For steady flow, the solution should be independent of time, which means $\frac{\partial \rho}{\partial t} = 0$. Thus the equation for steady flow is expressed as:

$$\frac{\partial (\rho u)}{\partial x} + \frac{\partial (\rho v)}{\partial y} + \frac{\partial (\rho w)}{\partial z} = 0 \tag{3.2}$$

For incompressible fluid, ρ =constant, which means

$\frac{d\rho}{dt} = \frac{\partial \rho}{\partial t} + u\frac{\partial \rho}{\partial x} + v\frac{\partial \rho}{\partial y} + w\frac{\partial \rho}{\partial z} = 0$. So we can derive the simplified continuity equation for incompressible liquid:

$$\frac{\partial u}{\partial x} + \frac{\partial v}{\partial y} + \frac{\partial w}{\partial z} = 0 \tag{3.3}$$

3.1.2 The Momentum Equation

Another fundamental physical principle involves the conservation of momentum and Newton's second law, $\mathbf{F} = m\mathbf{a}$.

By considering the relation between the forces (body forces and surface forces) and the acceleration of the fluid element, the equations are derived as:

$$-\frac{\partial P}{\partial x}+\frac{\partial \tau_{xx}}{\partial x}+\frac{\partial \tau_{yx}}{\partial y}+\frac{\partial \tau_{zx}}{\partial z}+\rho f_x=\rho(\frac{\partial u}{\partial t}+u\frac{\partial u}{\partial x}+v\frac{\partial u}{\partial y}+w\frac{\partial u}{\partial z}) \tag{3.4a}$$

$$-\frac{\partial P}{\partial y}+\frac{\partial \tau_{xy}}{\partial x}+\frac{\partial \tau_{yy}}{\partial y}+\frac{\partial \tau_{zy}}{\partial z}+\rho f_y=\rho(\frac{\partial v}{\partial t}+u\frac{\partial v}{\partial x}+v\frac{\partial v}{\partial y}+w\frac{\partial v}{\partial z}) \tag{3.4b}$$

$$-\frac{\partial P}{\partial z}+\frac{\partial \tau_{xz}}{\partial x}+\frac{\partial \tau_{yz}}{\partial y}+\frac{\partial \tau_{zz}}{\partial z}+\rho f_z=\rho(\frac{\partial w}{\partial t}+u\frac{\partial w}{\partial x}+v\frac{\partial w}{\partial y}+w\frac{\partial w}{\partial z}) \tag{3.4c}$$

where f_x, f_y and f_z denote the 3 components of body force per unit mass acting on the fluid element, when they are present; P is the pressure and τ_{ij} $(i \neq j)$ is the shear stress in a fluid element relating to the time rate of change of the deformation of the fluid element; whereas the normal stress τ_{ii} (when $i = j$) relates to the time rate of change of volume of the fluid element.

$$\tau_{xx}=\lambda(\nabla\cdot\mathbf{V})+2\mu\frac{\partial u}{\partial x} \tag{3.5a}$$

$$\tau_{yy}=\lambda(\nabla\cdot\mathbf{V})+2\mu\frac{\partial v}{\partial y} \tag{3.5b}$$

$$\tau_{zz}=\lambda(\nabla\cdot\mathbf{V})+2\mu\frac{\partial w}{\partial z} \tag{3.5c}$$

$$\tau_{xy}=\tau_{yx}=\mu(\frac{\partial v}{\partial x}+\frac{\partial u}{\partial y}) \tag{3.5d}$$

$$\tau_{xz}=\tau_{zx}=\mu(\frac{\partial w}{\partial x}+\frac{\partial u}{\partial z}) \tag{3.5e}$$

$$\tau_{yz} = \tau_{zy} = \mu(\frac{\partial w}{\partial y} + \frac{\partial v}{\partial z}) \tag{3.5f}$$

where μ is the molecular viscosity coefficient and λ is the second (or bulk) viscosity coefficient, $\mathbf{V} = u\mathbf{i} + v\mathbf{j} + w\mathbf{k}$ is the velocity vector.

Stokes made the hypothesis:

$$\lambda = -\frac{2}{3}\mu \tag{3.6}$$

Substituting the equations 3.5 (a-f) and 3.6 into 3.4(a-c), we can obtain the well-known Navier-Stokes (N-S) equations:

$$\frac{\partial(\rho u)}{\partial t} + \frac{\partial(\rho u^2)}{\partial x} + \frac{\partial(\rho uv)}{\partial y} + \frac{\partial(\rho uw)}{\partial z} =$$

$$-\frac{\partial P}{\partial x} + \frac{\partial}{\partial x}\left[\mu(-\frac{2}{3}\nabla\cdot\mathbf{V} + 2\frac{\partial u}{\partial x})\right] + \frac{\partial}{\partial y}\left[\mu(\frac{\partial v}{\partial x} + \frac{\partial u}{\partial y})\right] + \frac{\partial}{\partial z}\left[\mu(\frac{\partial w}{\partial x} + \frac{\partial u}{\partial z})\right] + \rho f_x \tag{3.7a}$$

$$\frac{\partial(\rho v)}{\partial t} + \frac{\partial(\rho uv)}{\partial x} + \frac{\partial(\rho v^2)}{\partial y} + \frac{\partial(\rho vw)}{\partial z} =$$

$$-\frac{\partial P}{\partial y} + \frac{\partial}{\partial x}\left[\mu(\frac{\partial v}{\partial x} + \frac{\partial u}{\partial y})\right] + \frac{\partial}{\partial y}\left[\mu(-\frac{2}{3}\nabla\cdot\mathbf{V} + 2\frac{\partial v}{\partial y})\right] + \frac{\partial}{\partial z}\left[\mu(\frac{\partial w}{\partial y} + \frac{\partial v}{\partial z})\right] + \rho f_y \tag{3.7b}$$

$$\frac{\partial(\rho w)}{\partial t} + \frac{\partial(\rho uw)}{\partial x} + \frac{\partial(\rho vw)}{\partial y} + \frac{\partial(\rho w^2)}{\partial z} =$$

$$-\frac{\partial P}{\partial z} + \frac{\partial}{\partial x}\left[\mu(\frac{\partial w}{\partial x} + \frac{\partial u}{\partial z})\right] + \frac{\partial}{\partial y}\left[\mu(\frac{\partial w}{\partial y} + \frac{\partial v}{\partial z})\right] + \frac{\partial}{\partial z}\left[\mu(-\frac{2}{3}\nabla\cdot\mathbf{V} + 2\frac{\partial w}{\partial z})\right] + \rho f_z \tag{3.7c}$$

They are called the Navier-Stokes equations in honour of two men, M. Navier and G. Stokes, who independently obtained the equations in the first half of the nineteenth century [137].

It is essential we simplify the complete Navier-Stokes equations according to the problems we are solving. In many applications the fluid density could be assumed as

constant. The compressibility is generally neglected even for gases when the Mach number is below 0.3. For such incompressible flows (or flows with constant density) the equations are expressed as:

$$\rho(\frac{\partial u}{\partial t}+u\frac{\partial u}{\partial x}+v\frac{\partial u}{\partial y}+w\frac{\partial u}{\partial z})=-\frac{\partial \rho}{\partial x}+\mu(u\frac{\partial^2 u}{\partial x^2}+v\frac{\partial^2 u}{\partial y^2}+w\frac{\partial^2 u}{\partial z^2})+\rho f_x \tag{3.8a}$$

$$\rho(\frac{\partial v}{\partial t}+u\frac{\partial v}{\partial x}+v\frac{\partial v}{\partial y}+w\frac{\partial v}{\partial z})=-\frac{\partial P}{\partial y}+\mu(u\frac{\partial^2 v}{\partial x^2}+v\frac{\partial^2 v}{\partial y^2}+w\frac{\partial^2 v}{\partial z^2})+\rho f_y \tag{3.8b}$$

$$\rho(\frac{\partial w}{\partial t}+u\frac{\partial w}{\partial x}+v\frac{\partial w}{\partial y}+w\frac{\partial w}{\partial z})=-\frac{\partial P}{\partial z}+\mu(u\frac{\partial^2 w}{\partial x^2}+v\frac{\partial^2 w}{\partial y^2}+w\frac{\partial^2 w}{\partial z^2})+\rho f_z \tag{3.8c}$$

Furthermore, they can be simplified in form by adopting vector operators:

$$\rho(\frac{\partial \mathbf{V}}{\partial t}+\mathbf{V}\cdot\nabla\mathbf{V})=-\nabla p+\mu\nabla^2\mathbf{V}+\rho\mathbf{f} \tag{3.9}$$

The left of the equation is demonstrating the inertial change per volume of fluid while the right is the sum of the forces acting on the fluid (i.e. Newton's second law). The first term on the left is unsteady acceleration, relating to the acceleration at a fixed location; the second term is convective acceleration, namely the effect of time independent acceleration of a fluid element with respect to space. On the right, the first term is the pressure gradient; the second term is viscosity interpreted as diffusion of momentum or as shear stress; the third term is body force, usually gravity, centrifugal forces, electromagnetic forces etc.

3.2 Discretization Approaches

A suitable discretization method must be chosen for the differential equations to be substituted by a series of algebraic equations to deliver the solutions at the selected discrete locations in space and time. The 3 most important and commonplace

approaches are: finite difference (FD), finite volume (FV) and finite element (FE) methods. Other methods exist, such as boundary element methods and particle methods, but the prevalence of the first three in CFD is such that we shall briefly present those and then focus on the finite volume method, which is the technique used in this study.

3.2.1 Finite Difference Methods

This is the oldest method for solving partial differential equations (PDEs). It is applied on the domain of interest after it has been covered, or discretized, by a grid. The differential equation is approximated by replacing the partial derivatives by difference quotients of the nodal values. For doing this, Taylor series expansion is normally used to obtain the approximation of the first, second or higher order derivatives at the desired degree of accuracy. Eventually the PDEs are replaced by a system of algebraic equations per grid node. Fig. 3-1 shows an exemplar for a 2D grid which FD methods adopt.

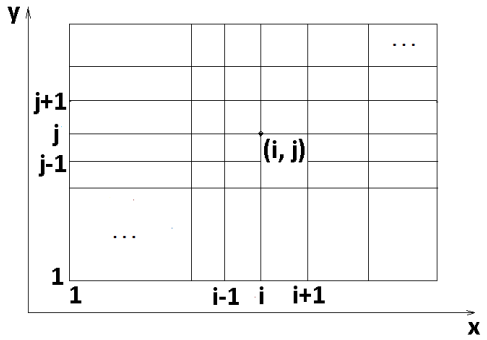

Fig. 3-1 2D Cartesian grid for FD methods

By ignoring the higher order terms in Taylor series expansion, the approximation of the first derivative can be expressed as:

$$\left(\frac{\partial \phi}{\partial x}\right)_{i,j} = \frac{\phi_{i+1,j} - \phi_{i,j}}{x_{i+1,j} - x_{i,j}} \tag{3.10a}$$

$$\left(\frac{\partial \phi}{\partial x}\right)_{i,j} = \frac{\phi_{i,j} - \phi_{i-1,j}}{x_{i,j} - x_{i-1,j}} \tag{3.10b}$$

$$\left(\frac{\partial \phi}{\partial x}\right)_{i,j} = \frac{\phi_{i+1,j} - \phi_{i-1,j}}{x_{i+1,j} - x_{i-1,j}} \tag{3.10c}$$

where ϕ is the local generic quantity, x is the coordinate.

These are the forward difference, backward difference and central difference schemes respectively. In fact, in these equations we have deleted the higher order terms which constitute the truncation errors on the right hand side. This indicates the accuracy of the approximation.

The numerical solution is influenced by two sources of error:

1. Discretization error: This is the difference between the exact analytical solution of the partial differential equation and the exact solution of the corresponding difference equation. The discretization error equals to the truncation error plus any errors introduced by the numerical treatment of the boundary conditions. It is related to the fineness of the grid applied as well as the chosen discretization scheme.

2. Round-off error: Round-off error arises for calculations can only be performed to a finite number of significant figures on the computer.

In the FD method, the stability behaviour of the numerical solutions must also be raised. If the numerical solution is converging consistently to the exact solution, the numerical approach is stable. If the numerical error is amplified from one step to the next, the calculation will be unstable. Thus the stability should be discussed before

any numerical error analysis.

On simple grids topologies, the FD method is simple and effective. The disadvantage of FD methods is the basic conservation laws are not identically satisfied, unless special treatment is taken [138].

3.2.2 Finite element Method

The FE method is mostly popular for structural analysis of solids but it is also used for fluids problems. It is similar to the FV methods to some extent for the domain is also broken into a set of discrete volumes or finite elements. However FE method adopts a weight function and then integrates the governing equations over the entire domain. Then the flow variables within each element can be calculated, given applied restrictions on the continuity of functions over element interfaces [138].

The advantage of FE method is it can deal with varied geometries, the grids are conveniently refined and the element could be adaptably divided. It is significantly more involved in implementing than the other methodologies however.

3.2.3 Finite Volume Method

The FV method adopts the integral form of the conservation equations on a finite number of contiguous control volumes which are divided from and define the domain. Consider the generic conservation equation for a quantity ϕ:

$$\frac{\partial(\rho\phi)}{\partial t}+\nabla\cdot(\rho\mathbf{V}\phi)=\nabla\cdot(\Gamma\nabla\phi)+S_{\phi} \tag{3.11}$$

where Γ is the diffusion coefficient, S_{ϕ} is the source term for ϕ.

The four terms in the above equation are the unsteady term, the convection term, the diffusion term and the source term. To illustrate the FV method, we just simplify the equation by assuming it is one dimensional steady non-convective problem. Thus it could be denoted as:

$$\frac{\partial}{\partial x}\left(D\frac{\partial \phi}{\partial x}\right)+S_{\phi}=0 \tag{3.12}$$

where D is set to be a constant diffusion coefficient.

Fig. 3-2 shows the one-dimensional local domain. P, E and W are the neighboring nodes. The control volume is between e and w[5].

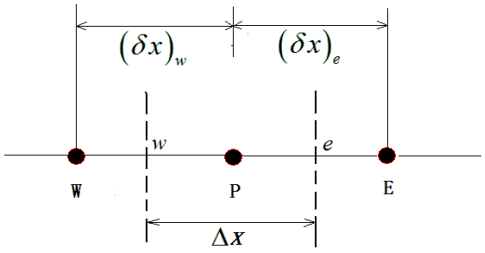

Fig. 3-2 One dimensional domain for FV method

A finite integration is applied over the control volume:

$$\int_w^e \frac{\partial}{\partial x}\left(D\frac{\partial \phi}{\partial x}\right)dx+\int_w^e S_{\phi}dx=0 \tag{3.13}$$

By applying the grad theorem, we can rewrite the first term:

$$\left(D\frac{\partial \phi}{\partial x}\right)_e-\left(D\frac{\partial \phi}{\partial x}\right)_w+\int_w^e S_{\phi}dx=0 \tag{3.14}$$

For the derivatives we can apply the difference quotient approach using the nodal variable value. For the source term, the simplest approximation for integration is

[5] Traditionally, in control volume analyses, the symbols e,w,n,s,u,d are used to indicate nodes or elements "east" (to the right), "west" (to the left) etc. of the central node/element p. Smallcase indicates interfaces, capital case indicates nodes.

finding the average value $\overline{S_\phi}$, satisfying $\overline{S_\phi}\Delta x = \int_w^e S_\phi dx$.

Thus the equation could be rewritten as:

$$\frac{D_e(\phi_E - \phi_P)}{(\delta x)_e} - \frac{D_w(\phi_P - \phi_W)}{(\delta x)_w} + \overline{S_\phi}\Delta x = 0 \tag{3.15}$$

By rearranging the terms, we can cast this equation in a common (and amenable to matrix manipulation) "pseudo"-linear system form:

$$a_P\phi_P = a_E\phi_E + a_W\phi_W + b \tag{3.16}$$

where $a_E = \frac{D_e}{(\delta x)_e}$; $a_W = \frac{D_w}{(\delta x)_w}$; $a_P = a_E + a_W$; $b = \overline{S_\phi}\Delta x$

The FV method is capable of utilizing any type of discretisation and thus any type of grid: it is suitable for complex geometries. Moreover, this method is inherently conservative, since the equations of conservation are satisfied, through the integration process mentioned above even for coarse resolutions. Also the terms needed to be approximated have clear physical meaning - fluxes.

In the more general case, of multidimensional arbitrary meshes, consider a 2D control volume as shown in Fig. 3-3. For the convection term $\nabla\cdot(\rho\mathbf{V}\phi)$ in generic conservation equation, in the finite volume method it is discretized by integrating as:

$$\int_\vartheta \nabla\cdot(\rho\mathbf{V}\phi)\,d\vartheta = \oint_A \rho\phi\mathbf{V}\cdot\mathbf{n}dA = \sum_e C_e\phi_e \tag{3.17}$$

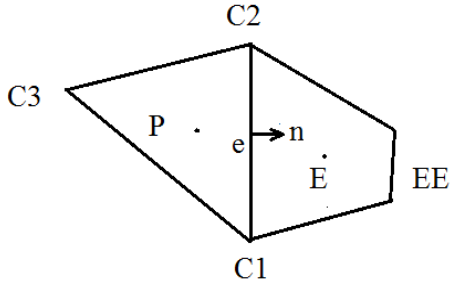

Fig. 3-3 2D cell for finite volume discretization adapted from [139]

Hence, detailed discretization techniques should be applied because generally all dependent variables and material properties are stored at the cell centre P but the expression includes the variables at the cell face which need to be interpolated. There are several schemes employed for this step: first-order upwind scheme, central difference scheme, second-order upwind scheme etc. In the first-order scheme, ϕ_e is taken to be the value of ϕ at the upstream cell centre:

$$\phi_e^{UP} = \begin{cases} \phi_P, \ if \ V^n{}_e > 0 \\ \phi_E, \ if \ V^n{}_e < 0 \end{cases} \tag{3.18}$$

This scheme has first-order accuracy and is one of the most stable schemes.

In the central difference scheme,

$$\phi_e^{CD} = \gamma_e \phi_P + (1-\gamma_e)\phi_E \tag{3.19}$$

where γ_e is the geometrical weighting function at face e. It is known that conventional central difference scheme may give rise to non-physical oscillations in the numerical solution. Thus central difference scheme with damping is sometimes used:

$$\phi_e = \alpha \phi_e^{UP} + (1-\alpha)\phi_e^{CD} \tag{3.20}$$

where α is the blending factor. This scheme has an order of accuracy between 1 and 2.

In the second-order upwind scheme:

$$\phi_e^{SUD} = \begin{cases} f\left(\phi_{C3}, \phi_P\right), \ if \ V^n{}_e > 0 \\ g\left(\phi_{EE}, \phi_E\right), \ if \ V^n{}_e < 0 \end{cases} \tag{3.21}$$

where ϕ_{C3} and ϕ_{EE} represent the value at the positions noted in Fig. 3-3. We utilize exclusively 2nd order central differencing in this study, with a negligible amount of

artificial damping, resulting to a scheme that is almost purely second order in space.

Iterative solvers for the discretized equations are more economical because they have less memory requirements than direct solvers. Here we introduce the Conjugate Gradient Squared (CGS) approach and the Algebraic MultiGrid (AMG) approach [139]. The conjugate gradient method is one of the most effective methods for the solution of symmetric, positive definite matrices. However, the matrices from discretization of the Navier-Stokes equation are asymmetric and so the CGS method is adopted by converting the asymmetric problem to a symmetric one. AMG method applies a multi-grid approach. The basic idea of a multi-grid solution is to use different grids for the same domain, from fine to coarse, to solve a set of equations. It firstly operates on the original grid to obtain the residual, then iterates on the coarse grid to get corrections taking the previous original grid residual as a source term, finally interpolates the corrections to the original grid and updates the original grid solution. By repeating the entire procedure the residual is reduced to the desired level. This method is effective because one grid can remove the errors of characteristic mesh spacing for the other. Further AMG offers two major advantages over other iterative methods including the CGS solvers: (a) the CPU time only increases in proportion to the number of variables in the equations; (b) faster convergence particularly for fully-unstructured meshes. Thus we adopt the AMG solver.

Pressure correction describes a series of methods in computational fluid dynamics for solving the Navier-Stokes equations for incompressible flows. They address the issue that in *segregated solvers* (i.e., solvers where the individual direction

momentum equations and continuity are solved individually, and then iterated) continuity does not involve pressure as a variable. The general idea is firstly to compute the provisional velocity field by solving the momentum equations with the current pressure (the estimate from the previous iteration). Then, the pressure-correction equation, which is derived from continuity, should be solved to gain a pressure-correcting value. The next step is to obtain the velocity correcting values through the relation between the velocity and pressure corrections. The new pressure and velocity value could be obtained by adding the correction to the starting pressure and velocities respectively. Then the new pressure will be the starting pressure for the next iteration. According to the different techniques for pressure correction proposed, different approaches can be found in the literature: SIMPLE, SIMPLER, SIMPLEC and PISO being the most well-known ones.

In this study we utilize the SIMPLEC method, which stands for Semi-Implicit Method for Pressure-Linked Equations Consistent. Cast on FVs as demonstrated in section 3.2.3, the incompressible fluid momentum equation 3-9 is discretized. After a transformation for simplification, the equation can take a form:

$$a_P u_P = \sum_{nb} a_{nb} u_{nb} + S - \sum_{e} P_e A_e n_{xe} \tag{3-22}$$

where nb refers to neighboring nodes; S is momentum source term; e denotes one of the faces of the cell.

To solve this equation to get velocity components, the pressure field should be known. However, at the start of iteration the pressure field is unknown. Thus a pressure which should be evaluated for the initial value P^* is adopted to derive by

equation:

$$a_P u_P^* = \sum_{nb} a_{nb} u_{nb}^* + S - \sum_e P_e^* A_e n_{xe} \tag{3-23}$$

We assume u' and P' stand for the corrections, where $u = u_P^* + u'$; $P = P^* + P'$. Subtract equation 3-23 from equation 3-22 and merge items:

$$u_P' = \sum_e P' A_e n_{xe} D_P \tag{3-24}$$

where $D_P = \dfrac{-1}{a_P - \sum_{nb} a_{nb}}$.

Considering mass conservation equation:

$$\sum_e \rho_e v_e A_e = 0 \tag{3-25}$$

It can be formulated as:

$$\frac{\rho' V}{Vt} + \sum_e (\rho_e v_e A_e)' = 0 - \sum_e (\rho_e v_e A_e)^* = S_m \tag{3-26}$$

where S_m is defined as mass correction (deficit). Thus the pressure correction equation is cast as:

$$a_P P_P' = \sum_{nb} a_{nb} P_{nb}' + S_m \tag{3-27}$$

To summarize, firstly from the evaluated pressure P^*, u_P^* is obtained through equation 3-23. Then the mass correction S_m can be calculated by equation 3-26, which is followed by solving for pressure correction P_P' in equation 3-27. In this way velocity correction u_P' can also be computed using equation 3-24. By assigning $u = u_P^* + u'$ and $P = P^* + P'$ to be the new evaluated velocities and pressure, a convergent solution can be obtained through iteration.

CFD ACE, developed by ESI Group, Paris France, is a set of computer codes and applications for computational fluid flow analysis. Among a number of commercial CFD packages, ACE is chosen for the transparency of its calculations [140]. It adopts

the finite-volume discretization approach and SIMPLEC pressure correction method.

3.3 Macro Particle and Surface Marker Point Approach

Multiphase flows are encountered in a variety of scientific and engineering fields as well as application areas such as biotechnology, microfluidics, chemical processing, environmental research, etc. The present work involves particles flowing in microchannels, which is a multiphase flow problem. We shall describe here a technique – the *Surface Marker Point* approach – capable of modeling arbitrary size and shape particles in fluids, especially relevant when the particle dimensions become comparable to the flow length scales. In this case, the particles can no longer be treated as point particles, mainly because the influence of particles on the surrounding fluid is not negligible and must be accounted for.

In this method, an individual particle is represented by a centre of mass location and a number of marker points (distributed on the particle's surface), indicating its extent. The solution for the trajectory of the particle follows a Lagrangian-Eulerian route. The particle holds tangential no-slip and zero normal flux boundary conditions. The accuracy of this approach depends on the resolution of the particle, which in turn depends on the computational grids being used in the simulations. Thus the grids for the flow domains should not be much larger than the particle. Fig. 3-4 shows the grids in the domain and the marker points on the surface of the particle in this method.

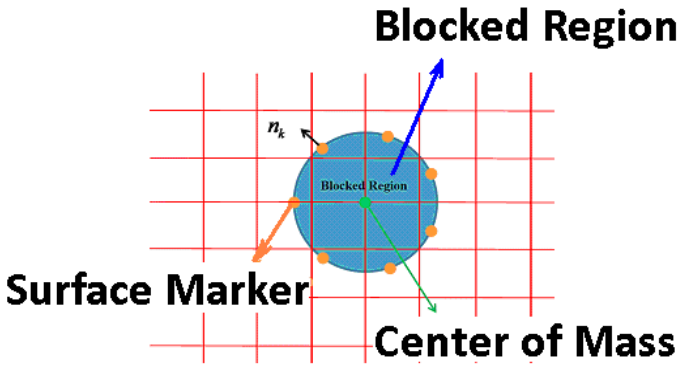

Fig. 3-4 Surface Marker Point Approach

For the fluid flow around the particle, the incompressible governing equations are presented:

$$\nabla \cdot \alpha_c \mathbf{V} = 0 \tag{3.22}$$

$$\frac{\partial \alpha_c \rho_c \mathbf{V}}{\partial t} + \mathbf{V} \cdot \nabla \alpha_c \rho_c \mathbf{V} = -\alpha_c \nabla P + \nabla \cdot \alpha_c \boldsymbol{\tau} + \alpha_c \rho_c \mathbf{f} \tag{3.23}$$

They are comparable to the standard conservation equations except for the presence of α_c, which is the local fluid volume fraction. $\boldsymbol{\tau}$ is the fluid stresses; $\mathbf{f}$ indicates any body force.

For the whole particle, the basic governing equations are the 6 degrees of freedom equations of motion in classical mechanics:

$$m\frac{d\mathbf{V}}{dt} = \mathbf{F} \tag{3.24}$$

$$\frac{d\mathbf{h}}{dt} = \mathbf{M} \tag{3.25}$$

where $\mathbf{h}$ is the angular momentum; $\mathbf{M}$ is the moment vector about the particle centroid.

The forces acting on the particle include hydrodynamic and other body forces. Hydrodynamic forces on the particle can be computed at the surface:

$$\mathbf{F}_{Hyd} = \sum_{k=1}^{N} (-p_k \mathbf{n}_k + \boldsymbol{\tau}_k \cdot \mathbf{n}_k) \Delta S_k \tag{3.26}$$

where N denotes the total number of marker points; p_k is the pressure imposed on the marker point k; $\boldsymbol{\tau}_k$ is the stress tensor at the marker point k; $\mathbf{n}_k$ is the outward normal vector at the marker point k; ΔS_k is the surface area attached to marker point k.

The moment vector $\mathbf{M}$ could be calculated by the similar way of summing up the product of single moment vectors and the surface area attached to the each marker point.

Thus, the movement of the particle, including translation and rotation, is explicitly computed. The blockage of the fluid domain by the particle and the corresponding transfer of momentum from one to the other are directly taken into account, thus the fluid moves the particle but it is also affected by its presence and its motion. For diluted samples focused on in this research, interactions between particles are rare, while lubrication effects also add barriers. Thus inter-particle collisions are not considered in this research, though both hard collision and soft collision approaches have been developed and can be conveniently integrated into current platform.

Time integration of this coupled system is achieved by time marching techniques. Traditional time marching however results in certain challenges that we outline and address here. Time and space coordinates have a major difference: direction of influence [136], since force at a position can influence the flow anywhere while change at a moment can only influence the future. Thus error can also accumulate in

the coupled problem of flow-particle trajectory, which is sensitive to the initial conditions and time step. An obvious approach to address this is to reduce the time step, resulting in reducing the error, but it's also not possible to decrease time step infinitely due to computational affordability. The time independence of the simulation results should at least meet two conditions. The first is a Courant–Friedrichs–Lewy (CFL) condition $\frac{u\Delta T}{\Delta x} \leq 1$. In our cases grid length Δx is normally at μm scale – 10^{-6}m, while for a particle with the velocity of 0.001m/s for example, thus the simulation time step should be $\Delta T \leq 0.001$s. This condition is easy to implement. However, the other condition is the simulation time step should be much smaller than the particle relaxation time to allow particles in simulation to have enough time to sense and respond to the changes of local flows. For a microparticle with diameter of, say, 10 μm, its relaxation time is 5.6×10^{-6} s; relaxation time for a 20 μm particle is 2.2×10^{-5} s; for a 40 μm particle it's 8.9×10^{-5} s. The simulation time step should be at least a couple of orders smaller than these values, rendering the simulations very costly: the main cost stems from the fact that although integrating the particles paths is economical (even for very fine time steps), the coupled particle-flow solution implies that the flow field, in its entirety, has to be recomputed for every particle time step. In effect, for fine resolution 3D flows, this implies a need to solve for the flow field billions or trillions of times, whereas it is only hundreds or thousands of times that such a solution is possible. This raises the necessity to make the computation not only reliable but also efficient, for which a novel approach is developed.

3.4 Frozen Flow and Flow Correction Coefficient (FCC) approach

Firstly the concept of 'Frozen Flow' is described. We define two different time stepping cycles: the *external* where the flow is advanced in time and the *internal* where the particle motion is integrated. The proposed technique assumes that during each simulation time step, the flow field around the particle is in a quasi-steady situation. Inside the external time step, an internal sub-time-step Δt_{Sub} is introduced to compute the particle trajectory based on the equivalent surrounding flow velocity and its induced equivalent drag force. According to Stokes' law, $F_{\mathrm{D}} = 6\pi\mu r v$ for a 3D sphere or $F_{\mathrm{D}} = 12\mu v$ (of unit length) for a 2D infinitely long cylinder. For more general situations, there are corrections of this drag force form which lead to $F_D = \frac{3\pi\mu d_p V_p}{C_c}\chi$.

The first correction is shape factor χ. For sphere χ=1, where χ>1 when the object is non-spherical. There is another correction for when the particle-flow no-slip condition cannot met at high Knudsen numbers, $Kn = \frac{\lambda}{L}$ (where λ is the liquid molecule mean free path; L is characteristic length), Cunningham correction factor C_{C} would be introduced as $C_{\mathrm{C}} = 1 + 2.52\frac{\lambda}{d}$. However the mean free path for a water molecule is at angstrom scale (10^{-10} m), which is much smaller than the particle diameter. Thus it can still be regarded as continuum fluid without slip and C_{C} converges to 1.

In reality, flows of interest are different from Stokes flow with finite velocity, thus

the drag is actually gained from the drag equation $F_D = \frac{1}{2}\rho v^2 C_d A$, which is a practical formula considering the above factors.

By doing so, all the surface forces on the particle are summarized as the equivalent drag force. The schematic of this approach is shown in Fig. 3-5.

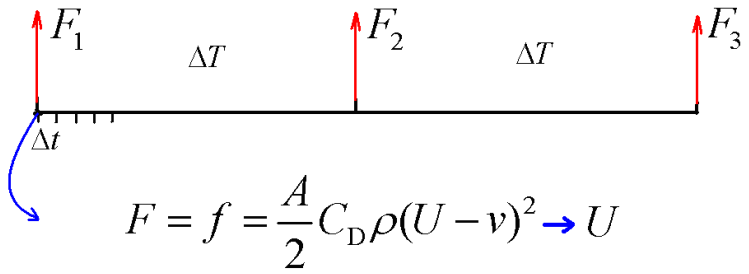

Fig. 3-5 Schematic of Frozen Flow approach

where F is the force during large (external) intervals ΔT computed directly using the Surface Marker Point approach, as (GFX, GFY, GFZ), f is the drag force, $A = \pi r^2$ is reference area, C_D is the drag coefficient which depends on local Reynolds number $\mathrm{Re} = \frac{\rho_P |U - v| d}{\mu}$, ρ is the density of fluid, U is the velocity of the local flow, v is the velocity of particle.

In our case, $\mathrm{Re} = \frac{\rho_P |U - v| d}{\mu} \approx 2 > 1$. In this transitional drag scheme, C_D cannot be treated as a constant, but a function of Re, where we choose $C_D = \frac{24}{\mathrm{Re}}(1 + 0.15\,\mathrm{Re}^{0.687})$ [141]. So far, during ΔT intervals only local flow velocity U is unknown, therefore U can be computed. In the implementation of the algorithm, the particle velocity v can be iteratively computed through time marching. Higher order schemes, like *Verlet integration* etc. can be applied on the sub-time-step Δt_{Sub}. Verlet integration is a method for calculating the movement of objects,

frequently used in Molecular Dynamics. The position of the object at the next time step is projected as $\mathbf{x}(t+\Delta t)=2\mathbf{x}(t)-\mathbf{x}(t-\Delta t)+\mathbf{a}(t)\Delta t^2$, while its velocity at the next time step is computed as $\mathbf{v}(t+\Delta t)=\dfrac{\mathbf{x}(t+\Delta t)-\mathbf{x}(t-\Delta t)}{2\Delta t}$, where $\mathbf{a}$ represents acceleration.

However U cannot be used explicitly because during the external time step ΔT, the particle is continuously accelerated by flow and in the meanwhile the flow is gradually decelerated by the particle, rendering $U \to v$. Thus we introduce the Flow Correction Coefficient (FCC) to measure the real influence of the changing flow field upon the particles. The purpose of FCC is to take the time average (which evaluates hydrodynamic forces due to the real flow) and space average (which is equivalent to virtual mass) effect into account.

Consider a particle (initial particle velocity is v_{P0}) which is purely accelerated by fluid (local flow velocity v_f), its velocity develops as $v_{\mathrm{P}}=v_{\mathrm{P0}}+v_f(1-e^{-\frac{t}{\tau_{\mathrm{S}}}})$, where t denotes time, $\tau_{\mathrm{S}}=\dfrac{\rho_{\mathrm{P}}d_{\mathrm{P}}{}^2}{18\mu}$ is particle relaxation time.

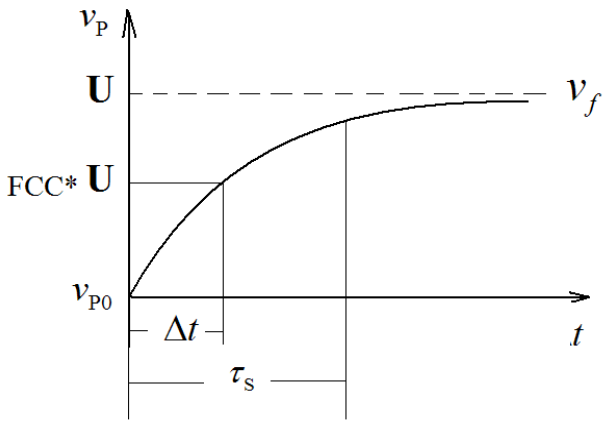

Fig. 3-6 Schematic of FCC approach

To measure the real flow effect, two weighting steps of the relative flow velocity,

time-average and space-average, are considered. The first one is time-averaging: $\overline{\Delta U} = \frac{\int_0^{\Delta t} \Delta U dt}{\Delta t} = \frac{\int_0^{\Delta t} (v_f - v_p) dt}{\Delta t} = v_f \frac{\tau_S}{\Delta t}(1 - e^{-\frac{\Delta t}{\tau_S}})$. However this can underestimate the real flow when Δt □ τ_S. Thus we take another form which has the same magnitude and trend when $\Delta t \to 0$ and is a constant when $\Delta t \geq \tau_S$. According to L'Hôpital's rule, $\lim_{\Delta t \to 0} \frac{\tau_S}{\Delta t}(1 - e^{-\frac{\Delta t}{\tau_S}}) = \frac{(1 - e^{-\frac{\Delta t}{\tau_S}})'}{(\frac{\Delta t}{\tau_S})'} = e^{-\frac{\Delta t}{\tau_S}}$. When $\Delta t \geq \tau_S$, the constant should be $e^{-\frac{\Delta t}{\tau_S}}\Big|_{\Delta t = \tau_S}$ to guarantee this function is continuous. Thus FCC should take the form FCC_{Time}= $e^{-\frac{\Delta t}{\tau_S}}$ if $\Delta t \leq \tau_S$; e^{-1} if $\Delta t > \tau_S$ (3.27)

From another perspective, $\Delta U = v_f e^{-\frac{\Delta t}{\tau_S}}$, and beyond the relaxation time, this equivalent relative flow velocity will have a fixed value due to the particle having fully responded to the flow influence and the system approaching an equilibrium state.

The second one is space-averaging. Similar to a trapezoid rule, a weighting coefficient 0.5 is adopted. The particle acceleration due to flow of current time step has a weighing coefficient of 0.5, while the next time step also takes another half to account for its influence. In the physical perspective, forces due to the particle acceleration, virtual mass effect (virtual mass of a sphere is $m_v = \frac{2}{3}\pi r^3 \rho_f$; for a neutrally buoyant particle, the virtual mass is equivalent to half of its own mass $m_v = \frac{1}{2} m_P$) and Basset force (normally neglected if the particle relaxation time is much smaller than the acceleration time), should be considered by introducing this coefficient. Otherwise, it can cause unstable solutions [142]. So FCC_{Space}=0.5.

Thus $\mathrm{FCC} = \mathrm{FCC_{Time}}\mathrm{FCC_{Space}} = \begin{cases} \Delta t \le \tau_S, \frac{1}{2}e^{-\frac{\Delta t}{\tau_S}} \\ \Delta t > \tau_S, \frac{1}{2}e^{-1} \end{cases}$. The effective particle-flow velocity difference is accounted as

$$\Delta U^*([t, t+\Delta t]) = \Delta U(t) \square \mathrm{FCC} \tag{3.28}$$

Rotation is a secondary factor for the cases of particle drifting in microfluidics. This is because the ratio of the Magnus force, caused by rotation, to drag force is $\mathrm{R_{MS}} = \frac{d_p^2}{24}\frac{\rho}{\mu}\Omega$ [143], where Ω is the angular velocity of the particle. This ratio becomes very small at microscales, especially in microfluidics where particles normally are aligned by and do not collide with walls. However, for the purpose of direct simulation, particle rotation is still considered. Similarly, a concept of rotational $\mathrm{FCC_{Rotation}}$ is introduced. Considering a spherical particle rotated by its surrounding flow with an equivalent rotational speed v_{RF}, the particle rotational speed should follow: $I\alpha = rF_{\mathrm{Rf}}$, where I is the moment of inertia, α is the angular acceleration, F_{Rf} is the equivalent flow force perpendicular to the particle radius. For a sphere, $I = \frac{2}{5}mr^2$; $\alpha = \frac{d\omega}{dt} = \frac{dv_{\mathrm{Rp}}}{rdt} = -\frac{d(v_{\mathrm{Rf}} - v_{\mathrm{Rp}})}{rdt} = -\frac{d\Delta v_{\mathrm{R}}}{rdt}$. It is assumed that the tangential force F_{Rf} agrees with the form of drag force $F_{\mathrm{Rf}} = \frac{1}{2}\rho\Delta v_{\mathrm{R}}{}^2 C_{\mathrm{D}} A$. In this way the relative rotational speed is derived as

$$\Delta v_{\mathrm{R}} = \frac{v_{\mathrm{Rf}}}{\frac{15}{16}C_{\mathrm{D}}\frac{v_{\mathrm{Rf}}}{r}t+1} = v_{\mathrm{Rf}}\frac{1}{\frac{15}{16}C_{\mathrm{D}}\omega_{\mathrm{Rf}}t+1} = v_{\mathrm{Rf}}(t) \square \mathrm{FCC}\frac{1}{\frac{15}{16}C_{\mathrm{D}}\omega_{\mathrm{Rf}}t+1} \tag{3.29}$$

Thus rotation FCC and effective particle-flow angular velocity difference are:

$$\mathrm{FCC_{Rotation}} = \frac{\mathrm{FCC}}{\frac{15}{16}C_{\mathrm{D}}\omega_{\mathrm{Rf}}t+1} \tag{3.30}$$

and

$$\Delta\omega^{*}\left(\left[t,t+\Delta t\right]\right)=\Delta\omega\left(t\right)\sqcup \mathrm{FCC}_{\mathrm{Rotation}} \tag{3.31}$$

The techniques described above have been implemented in the CFD-ACE (ESI Group, Paris, France) mutliphysics suite, with the use of user subroutines. These in-house implemented algorithms are first tested for self-consistency and resolution dependence, and are subsequently validated against available theoretical and mainly experimental data – this work is presented in the next chapter.

4. Method validation

As we have discussed in the last chapter, the computational simulation platform that we intend to use should be cross-checked and shown to allow interrogating the salient features of flow-particle interaction with accuracy, specificity and resolution. To achieve this, validation is demonstrated in this chapter, including grid- and time step-independence verification, along with comparison with available experimental data. The results show that our simulation platform performs with high accuracy and efficiency and it is capable of replicating and elucidating phenomena observed in experiments.

4.1 Grid independence

Under the same discretization scheme, a significant portion of computational error, the discretization error, is related to the fineness of the grid applied. If the grid is fine enough so that the solution cannot be improved markedly by refining the grid any more, the solution is said to achieve grid independence. To guarantee that the computational solution is reliable and invariant to refinement of the grid, a grid independence study is conducted. The schematic of the model used for this study is shown in Fig. 4-1. The height (third dimension, Z) of the channel is 75 μm. Thus the channel aspect ratio is $b/a = \frac{75}{150} = 0.5$; curvature ratio is $a/R_c = \frac{150}{200} = 0.75$. This channel is one of the actual microchannel geometries to be explored in the next chapter and thus conducting a grid independence analysis for this design has an application value. The complex Dean flow features can also be revealed and compared with previous findings.

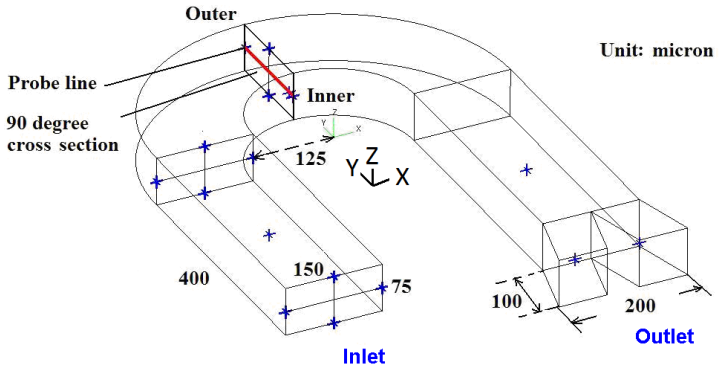

Fig. 4-1 Schematic of the investigated microchannel

Detailed grid independence analysis has been conducted to verify that the meshes utilized accurately resolve the flow. In this study, 3 sets of structured grids with multi-block are established and tested, shown in Fig. 4-2.

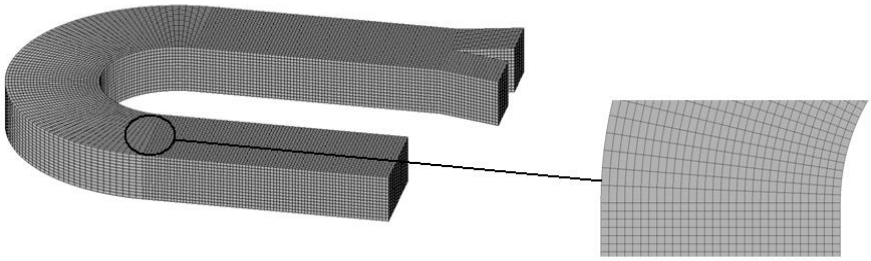

(a) The first set of grids. Nodes: 121200, Cells: 107520

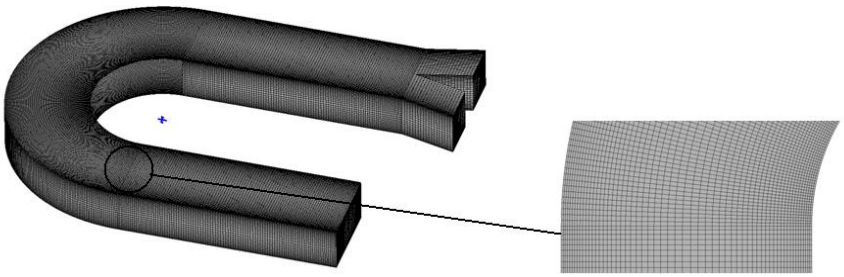

(b) The second set of grids. Nodes: 846600, Cells: 797326

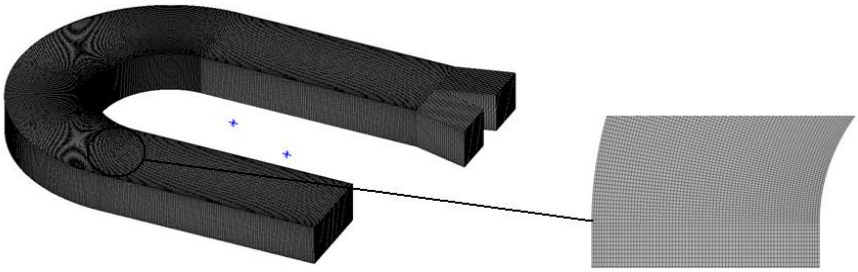

(c) The third set of grids. Nodes: 1690050, Cells: 1611794

Fig. 4-2 Three sets of structured multiblock grids

The first and second sets of grids are solved on a single core (Intel Core2 Quad) PC. Due to memory and speed limitations, the third set is computed on a multi-core platform in parallel.

To check the solutions, 6 lines at representative positions are defined, shown in Fig. 4-3. The velocity sampling direction is from bottom to top and from outer wall to inner wall.

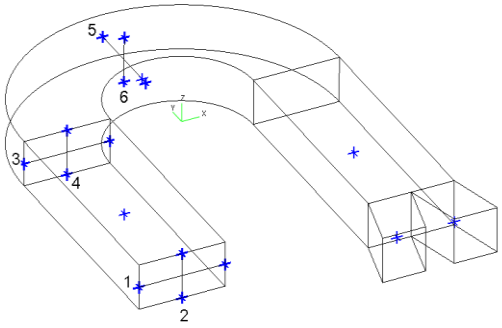

Fig. 4-3 The positions of the probe lines

The solutions of flow field are calculated for the 3 sets of grids with the same inlet velocities U =1 m/s, 5 m/s and 10 m/s. The velocity components U, V and W on the 6 probe lines have been shown in Fig. 4-4. In the figure, 'coarse' stands for the first set of grid; 'medium' refers to the second set; 'fine' represents the third one. $D_h = 100$ μm; $\mathrm{Re} = \frac{U_m D_h}{\nu} = 100[U_m]$; $De = (\frac{D_h}{R_c})^{0.5}\,\mathrm{Re} = 70.7[U_m]$; $[U_m]$ is the relevant dimensionless number as a function of the mean velocity. Thus, when $\mathrm{v} = 1\mathrm{m/s}$, $\mathrm{Re} = 100$, $De = 70.7$; when $\mathrm{v} = 5\mathrm{m/s}$, $\mathrm{Re} = 500$, $De = 353.5$; when $\mathrm{v} = 10\mathrm{m/s}$, $\mathrm{Re} = 1000$, $De = 707$.

Through the results, it can be observed that the second (medium) and third (fine) sets of grids lead to practically identical results and thus confirm grid independence for the solution. The only cases where these two meshes do not produce near-identical results correspond to velocity values that are very close to zero (cross-flow components sampled on regions of parallel-only flow) and thus represent only noise.

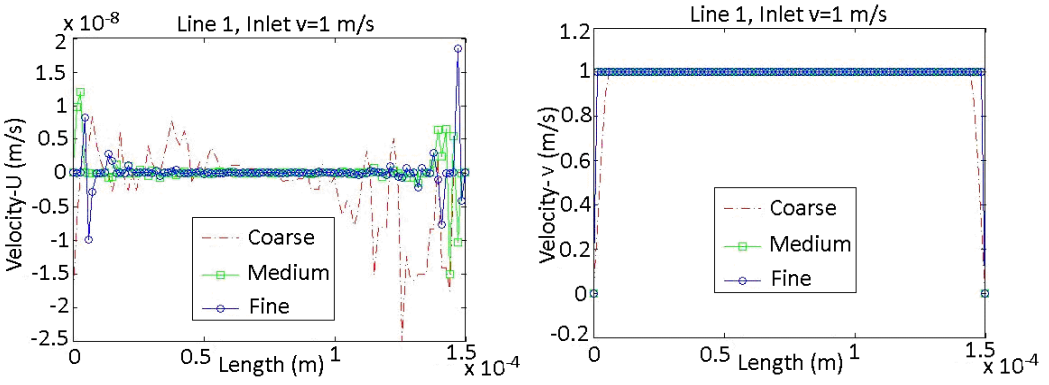

v=1m/s

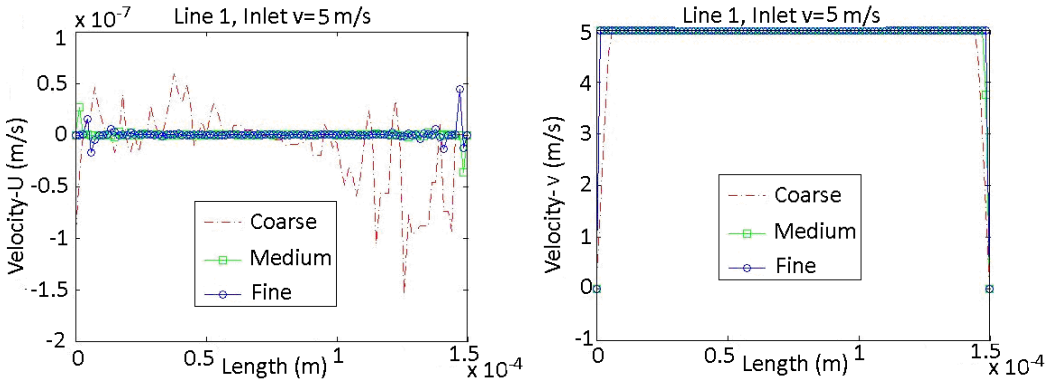

v=5m/s

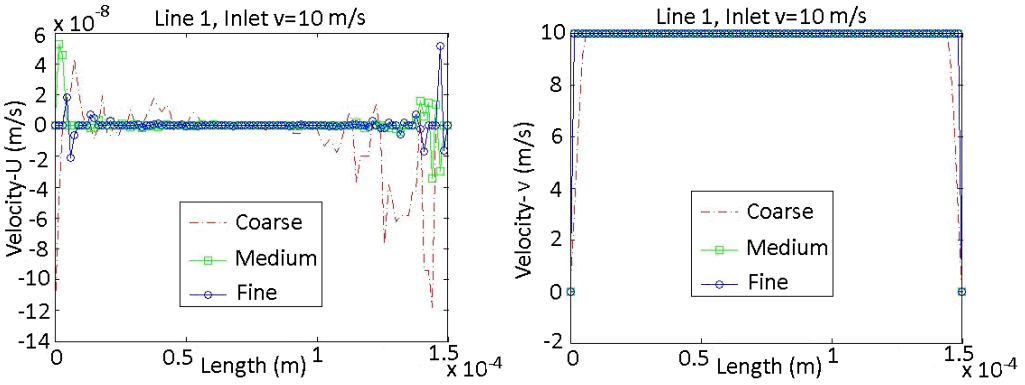

v=10m/s

(a) Line 1, comparison of velocity components U, V

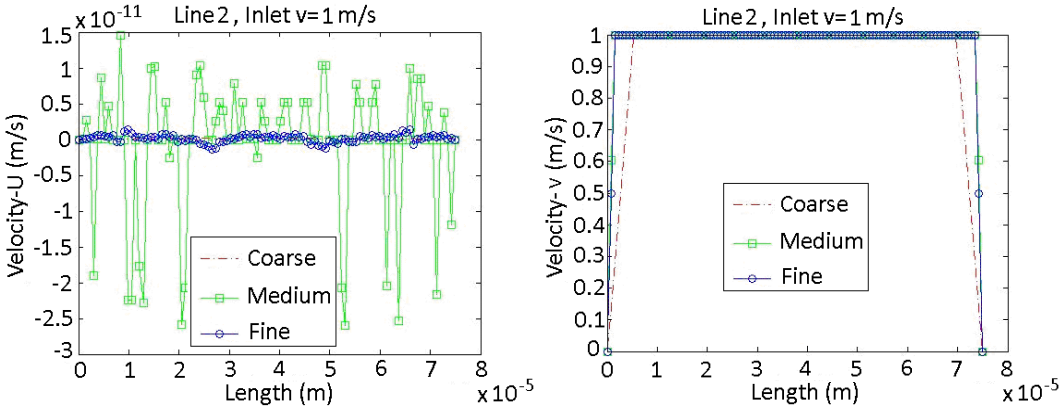

v=1m/s

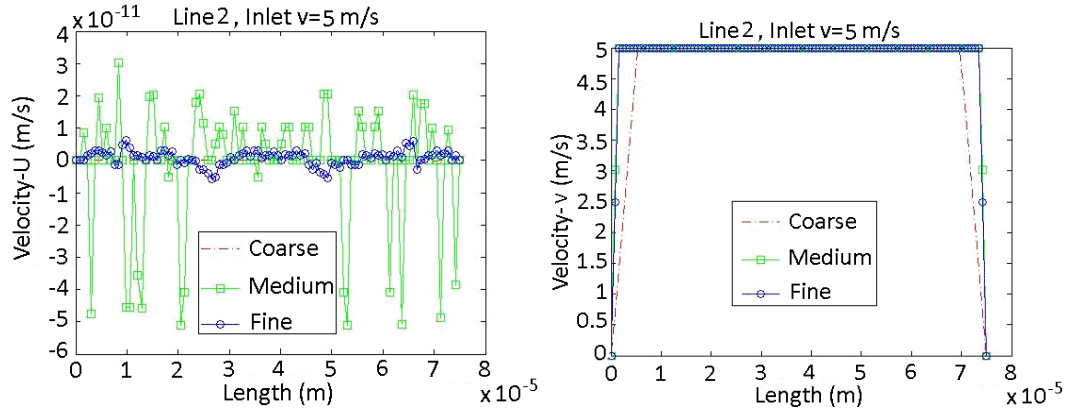

v=5m/s

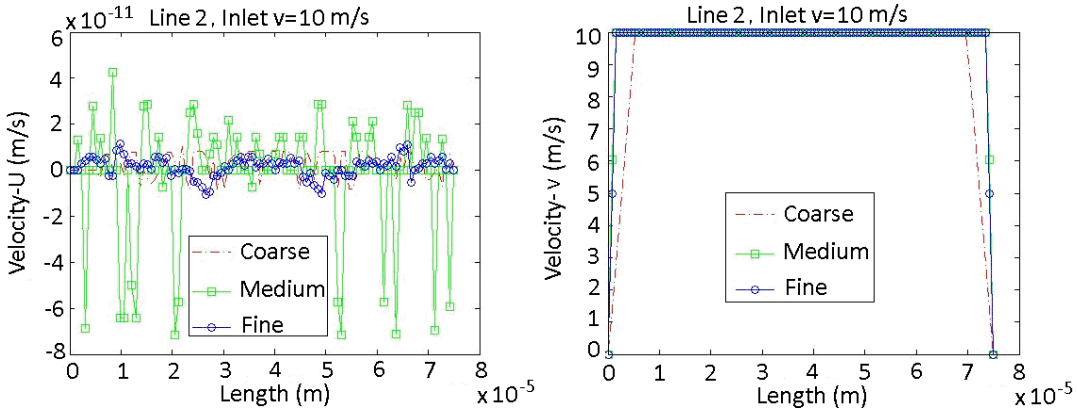

v=10m/s

(b) Line 2, comparison of velocity components U, V

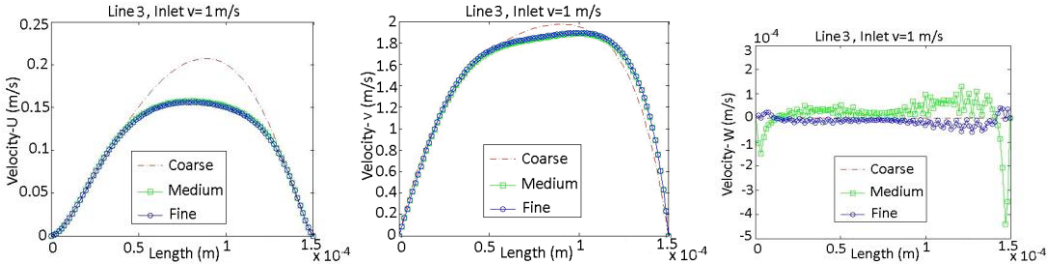

v=1m/s

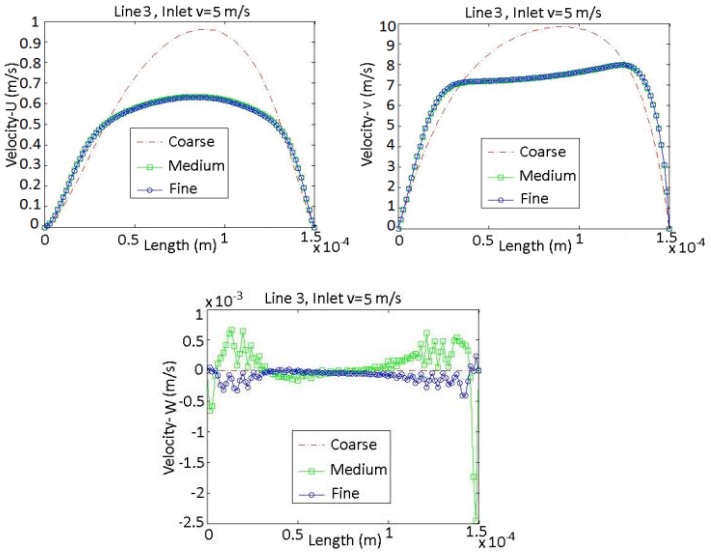

v=5m/s

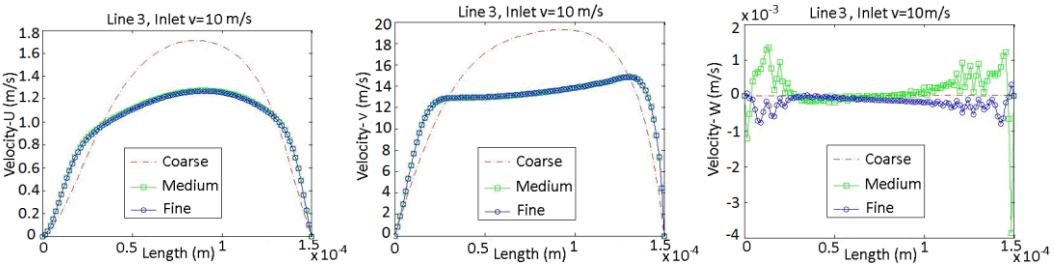

v=10m/s

(c) Line 3, comparison of velocity components U, V, W

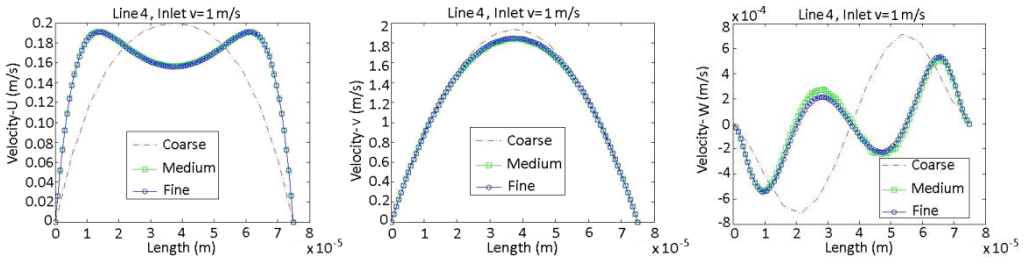

v=1m/s

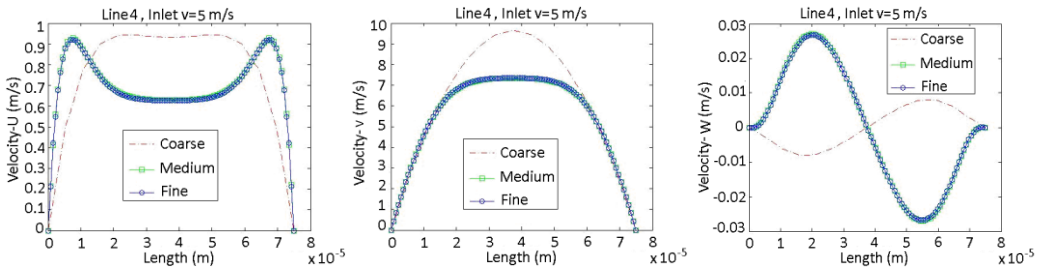

v=5m/s

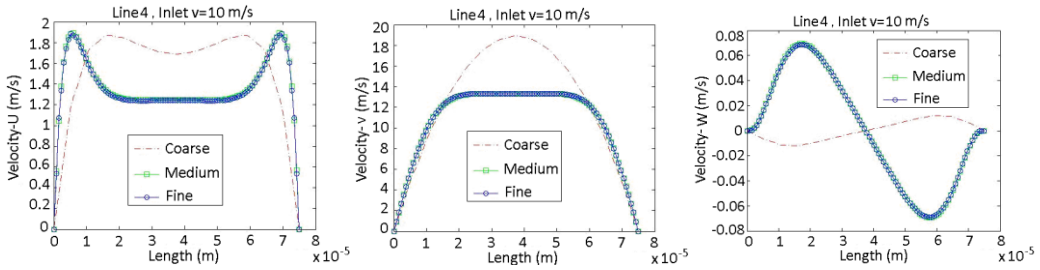

v=10m/s

(d) Line 4, comparison of velocity components U, V, W

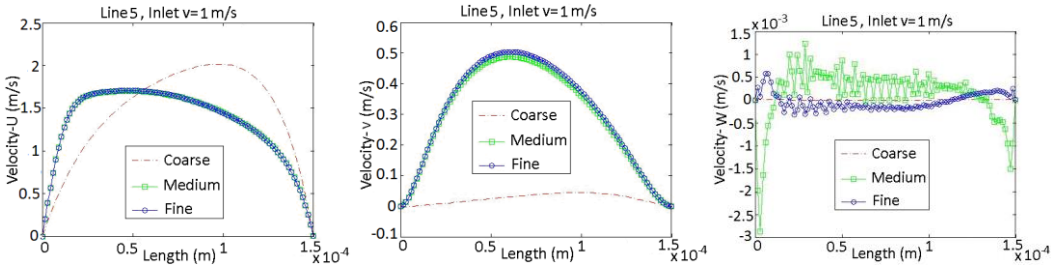

v=1m/s

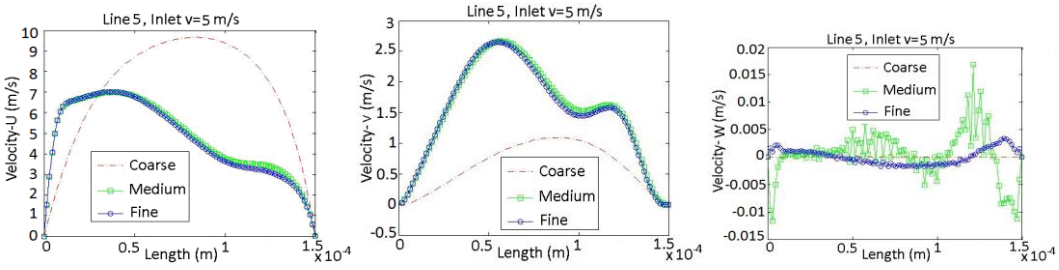

v=5m/s

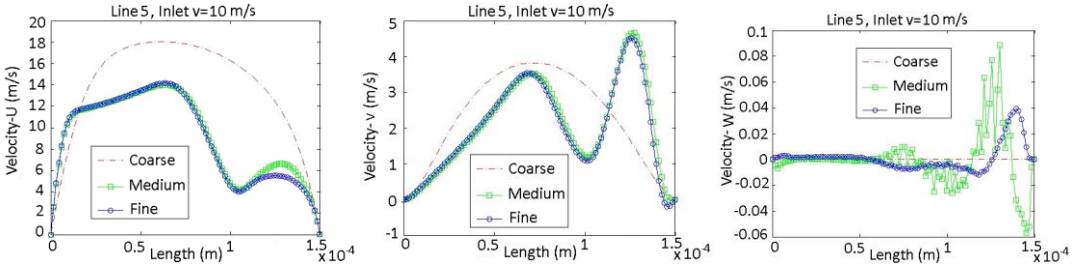

v=10m/s

(e) Line 5, comparison of velocity components U, V, W

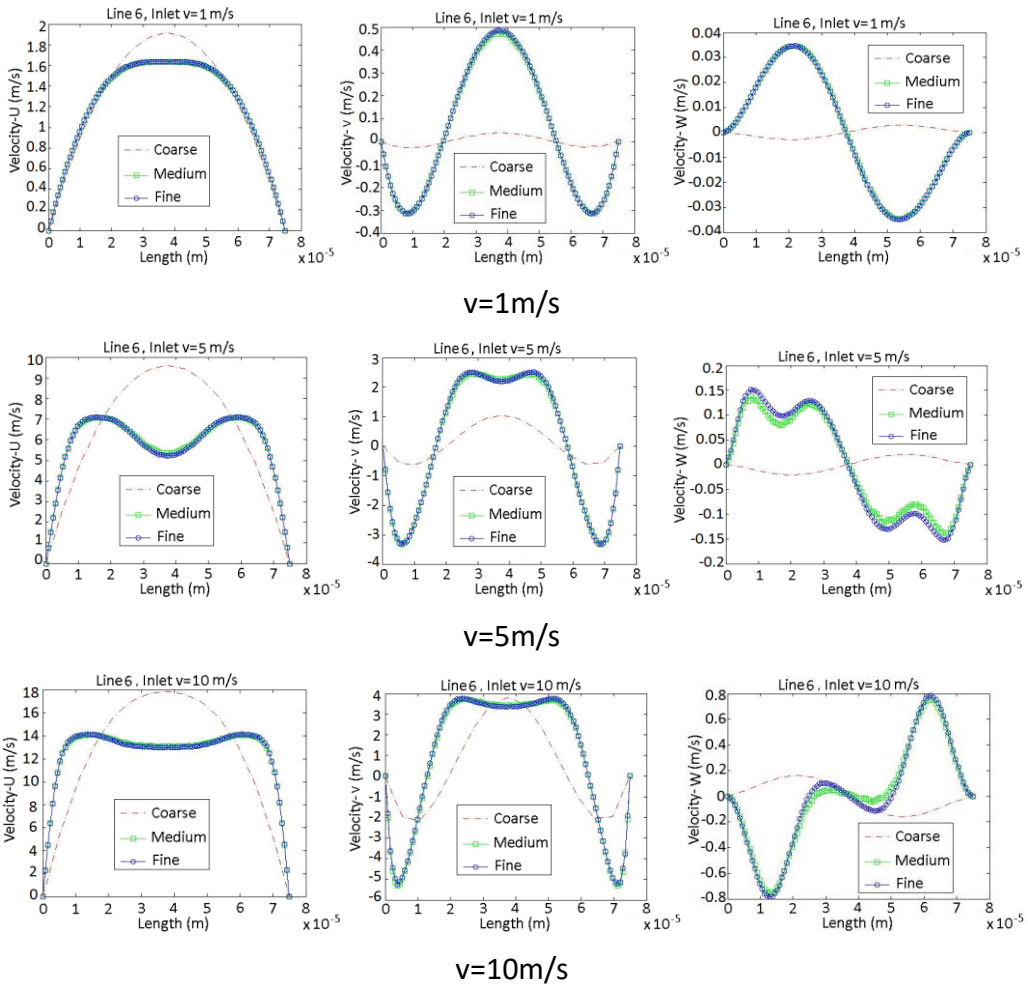

(f) Line 6, comparison of velocity components U, V, W

Fig. 4-4 Flow velocity components on 6 probe lines with different inlet velocities

We can see that these two sets of grids produce reliable and meaningful solutions, while the coarse grid leads to discrepancies which make the solution distinct from the real Dean flow pattern. This can be proved in many aspects when comparing to the experimental data. For example, the real axial velocity profiles measured by experiments on probe line 5 and 6 in curved channels have been shown in chapter 2.5.3 (see Fig. 2-24). Firstly, on the horizontal line 5, the peak of axial velocity profile should be closer to the outer wall within that range of Dean number studied. The medium and fine grids are consistent with this, however, the results of coarse grid

show the opposite trend when U =1 m/s and 5 m/s (see Fig. 4-4 (e)). Secondly, on the vertical line 6, with the increase of inlet velocity the axial velocity profile should develop to a depression (or double peak) from a plateau and then the depression should become more flat in the middle area due to the vortices' evolution, effects that are observed in the experiment. Again, the medium and fine grids depict this phenomenon precisely but results for the coarse grid fail to capture this effect. Considering computing efficiency at the same time, the second set of grids is obviously the one that should be adopted, guaranteeing an acceptable accuracy of the solution with manageable resources. All subsequent computations are also verified for grid independence, but we shall not present further evidence on this for brevity.

We must reiterate that in Fig. 4-4 (a), (b), (c) and (e) the agreement between the two finer grids appears to be sub-optimal and moreover there appears to be quite a bit of irregular noise. This is an artifact that does not compromise the accuracy of the solution and the claim of grid independence: invariably, where such behaviour is observed, the velocity involved is of markedly low value (usually close to zero or exactly zero). Such low velocities, when coexisting in a flow field with substantially higher values (as is the case here) suffer from signal-to-noise problems (different in origin but with the same end-result as any experimental technique) and are of low quality. Nevertheless the error in those (when normalized using the bulk inflow velocity) is always under 1%.

The cross-flow velocity vector field on the middle section (at the middle plane of the bending part, namely the 90^o cross section, containing line 3 and line 4) is

reported in Fig. 4-5.

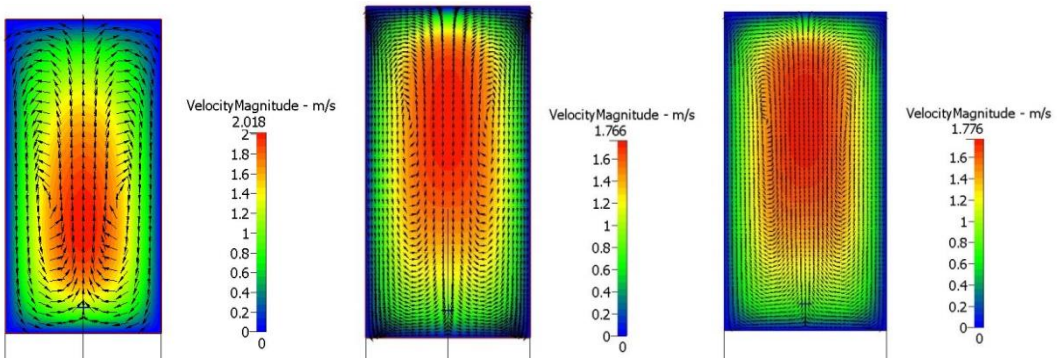

(1) course grids (2) medium grids (3) fine grids

(a) Velocity vectors on the middle section for v=1m/s

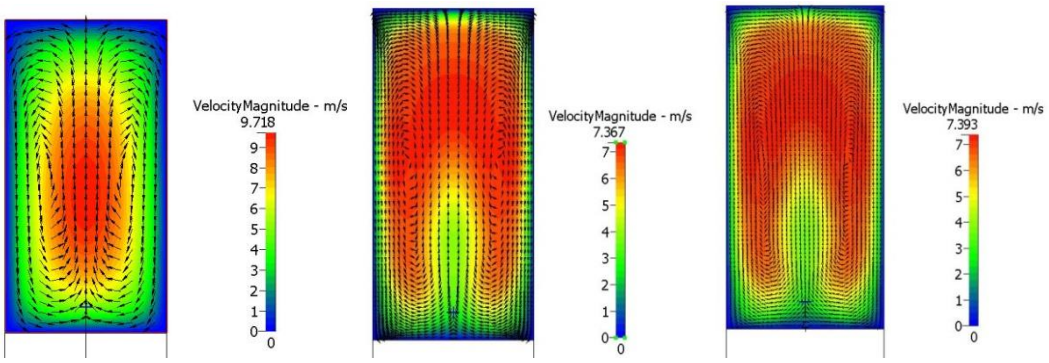

(1) course grids (2) medium grids (3) fine grids

(b) Velocity vectors on middle section for v=5m/s

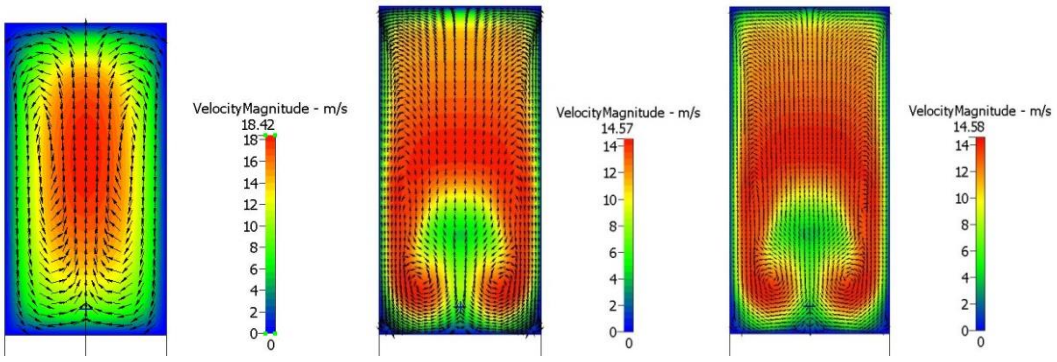

(1) course grids (2) medium grids (3) fine grids

(c) Velocity vectors on middle section for v=10m/s

Fig. 4-5 Velocity vector field on the middle section for different inlet velocities

The same message, i.e. that the coarse mesh is of inadequate resolution whereas the medium and fine ones capture essentially the same features is evident from this figure too.

As stated before, both the flow pattern and the flow velocity distribution of the Dean flow vary significantly at different Dean numbers, the curvature ratio and aspect ratio. Previous research efforts have not provided enough evidence to demonstrate the overall decisive factors influencing a Dean flow, nor given a substantial database to illuminate the relation between Dean flow patterns and a desirable range of Dean number. To investigate and present these clearly, a parametric study would be necessary which eventually could contribute to a parametric space map.

We employed dimensional analysis to get the minimum number of variables on which related phenomena depend. The base dimensions, namely mass, length and time are represented by M, L and T respectively. For the physical process of flow in the curved channel, the 6 variables should be considered: $\phi(\rho,\mu,U,a,b,R_c)=0$, where ρ denotes the density of fluid, μ the viscosity, U the inlet velocity, a the channel width, b the channel height, R_c the mean curvature radius. According to Buckingham's Pi Theorem, the number of independent dimensionless group k is decided by N, the number of decisive variables shown up in the case and R, the number of dimensions the process contains. The relationship is $k=N-R$. In the current study, $N=6$, $R=3$ (without temperature), thus $k=3$. These 3 dimensionless groups could be figured out by dealing with the equation groups set up by the relationship of the dimensions: $\prod_1=\frac{a}{R_c},\prod_2=\frac{b}{R_c},\prod_3=\frac{\mu}{\rho U R_c}$. Through an equivalent transformation, we get the final independent dimensional groups: $\prod_1'=De,\prod_2'=\frac{b}{a},\prod_3'=\frac{R_c}{D_h}$. This result exactly contains Dean number, aspect ratio

and curvature ratio, which can explain why the Dean flow pattern changes along these 3 numbers. Here, again, for a rectangular channel with fixed aspect ratio, the Dean number is chosen instead of the Reynolds number, because the Dean number shows more meaningful characteristics of flows induced by curved channels. For example, in the wide range of curvature ratio of a curved channel, the flow structure is only dependent on the Dean number (critical Dean number approaches to a constant).

In order to present how Dean flow is dependent on these 3 dimensionless numbers, a parametric space exploration is carried out. By filling the spatial points representing previous research and the current study in the three-dimensional space consisting by the 3 coordinates denoting the 3 dimensionless groups respectively, a comprehensive perspective can be depicted in Fig. 4-6. This study of Dean number is an important supplement to the parameter space review [144] regarding other dimensionless numbers for microfluidics.

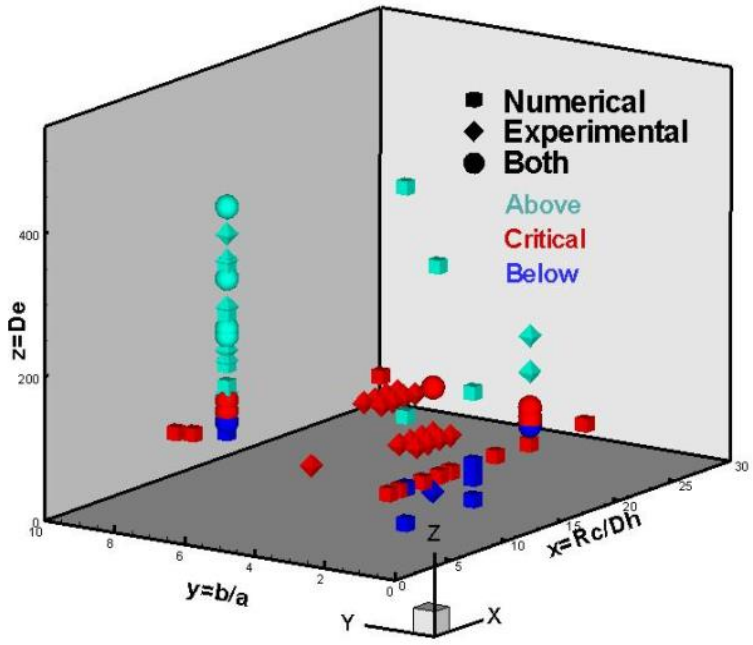

Fig. 4-6 Parametric space for Dean flow

To find the critical Dean number for this particular channel, over 10 cases of different Dean number have been computed. By checking velocity vectors on the middle section, we found that the second pair of vortices, namely the Dean vortices, appears when the inlet velocity ranges between 12.5 m/s $< v \leq$ 15 m/s, which implies the critical Dean number exists between $883 < De \leq 1060$.

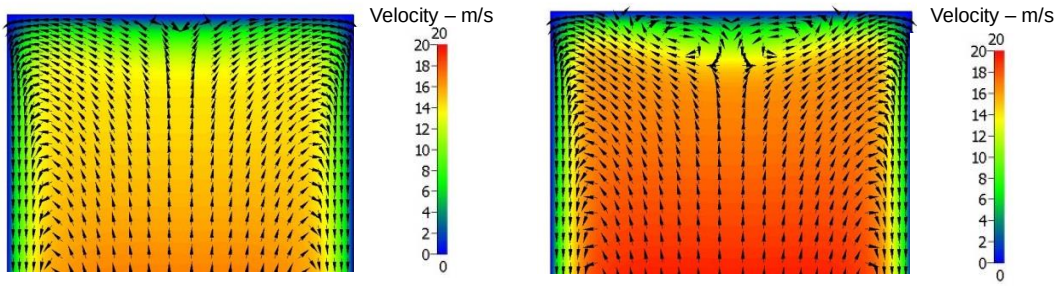

(a) v=12.5m/s, De=883 (b) v=15 m/s, De=1060

Fig. 4-7 The emergence of the Dean vortices for the channel under investigation

Assuming that the grid independence conclusion regarding the overall underlying mesh is now established, the other spatial resolution independence parameter, the Surface Marker Point density independence is satisfied by setting the marker points at inter-marker distances of the same magnitude as the flow domain grid spacing. Because the grid density ultimately determines the resolution, it is not necessary to make the surface marker point spacing much finer than the grid spacing. In this case the grid spacing is 2.5 μm, while the investigated particle sizes range between 10-50 micrometers. The surface marker point spacing can be set around 2.5 μm, hence the particle shape resolution can be guaranteed.

Thus, grid independence should be checked before further investigation in two aspects: 1. grid is fine enough based on which the correct flow field solution can be solved, especially for complex Dean flows; 2. surface marker point density, which

depends on grid ultimately, is fine enough to accurately describe the particle dimension and shape.

4.2 Time step independence

To further consider particle movement in a channel flow, the problem develops to be transient, which means the fourth dimension - time should be taken into account. The aforementioned Frozen Flow and Flow Correction Coefficient (FCC) approach are integrated and implemented with the internal sub-time-step of $10E^{-8}$s, if not explicitly specified differently. The validation of the numerical approach is achieved through several cases, including particle in curved channel, particle rotation, particle sedimentation and lift force on particles.

4.2.1 Particle in curved channel

In this part, an examination of the consistency of the time-stepping adopted, i.e. the Frozen Flow and FCC approaches, is demonstrated by simulating particle movement in curved channels. Without our Frozen Flow and FCC approach, most of the situations we shall present results for either require unrealistically long computing times to achieve, or actually fail, by leading to unphysical solutions (revealing the problems with time step selection we outlined above). Because the initial drag force is tremendously large, given the initial velocity difference of particle and flow, particles are normally ejected out of the boundaries when time step is not substantially finer than particle relaxation time – these computations lead to outright collapse. Even for

the limited number of cases where simulations can proceed, it is shown that unphysical results are obtained when the FF-FCC approach is not activated.

Firstly, a 2D channel with 150 μm width, 90° bend and average curvature radius of 200 μm is tested. A particle is released at the starting point of the bent centerline. Without activating FF-FCC, the particle movement only couples with ambient flow at external time step, thus the particle cannot sense the flow influence sufficiently and collides with the outer wall, shown in Fig. 4-8 (a), obeying thus a crude ballistic trajectory that numerous experimental results demonstrate to be unphysical. On the contrary, the FF-FCC approach results in a realistic trajectory, with the particle turning smoothly which is transported by the centrifugal flow.

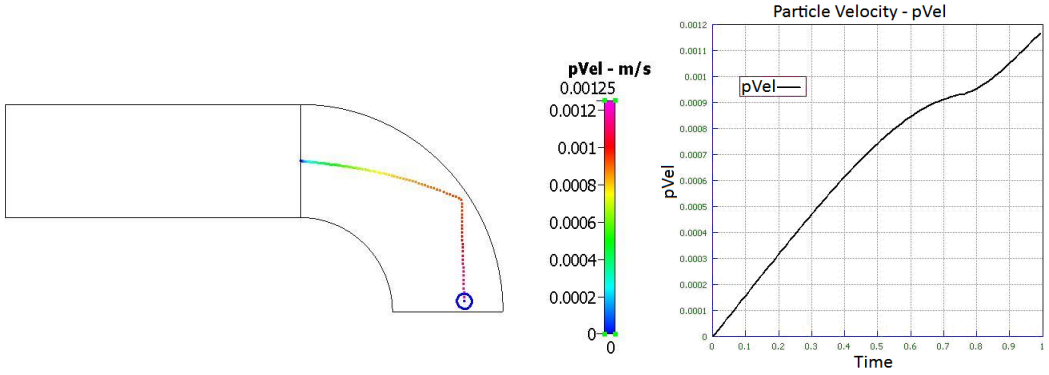

(a) Without Frozen Flow approach

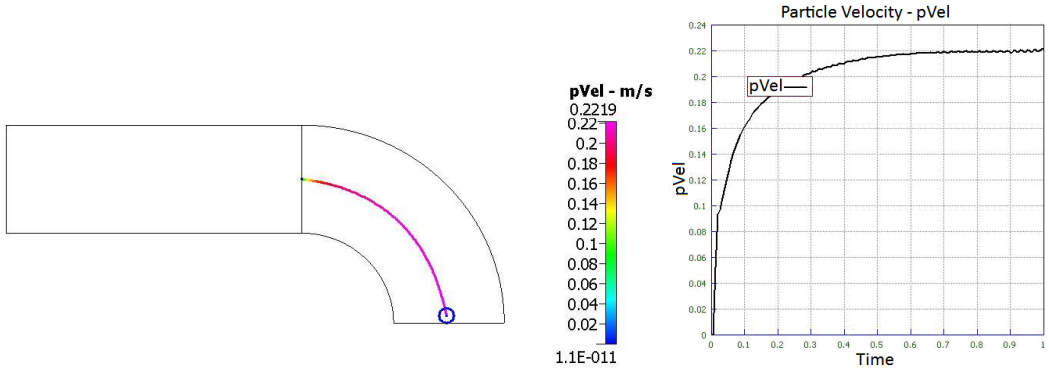

(b) With Frozen Flow approach

Fig. 4-8 Particle in 2D channel with 90° bend

Another 2D channel with 150 μm width, 180° bend and average curvature radius of

200 μm is tested. The same conclusion can be obtained, based on the results shown in Fig. 4-9.

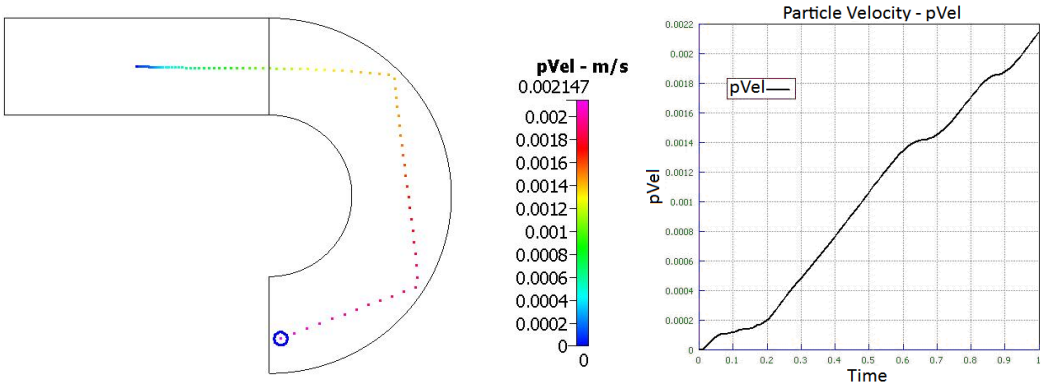

(a) Without Frozen Flow approach

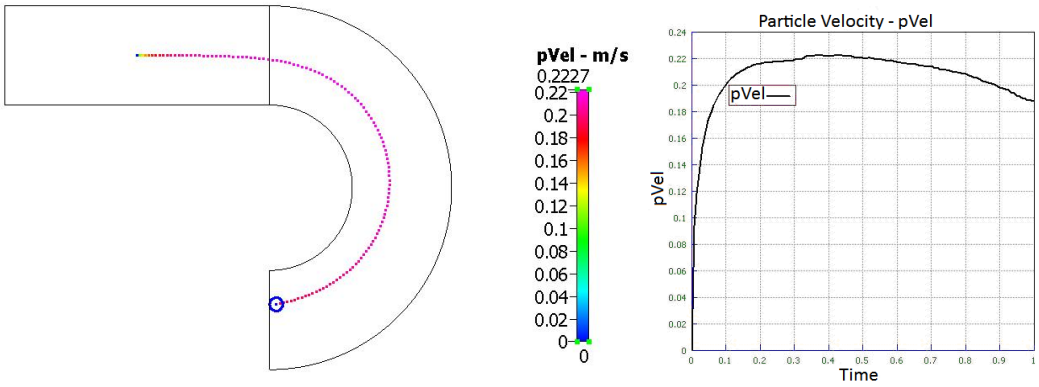

(b) With Frozen Flow approach

Fig. 4-9 Particle in 2D channel with 180° bend

A 3D curved channel with average curvature radius of 200 μm is then tested, with the dimensions shown in Fig. 4-10.

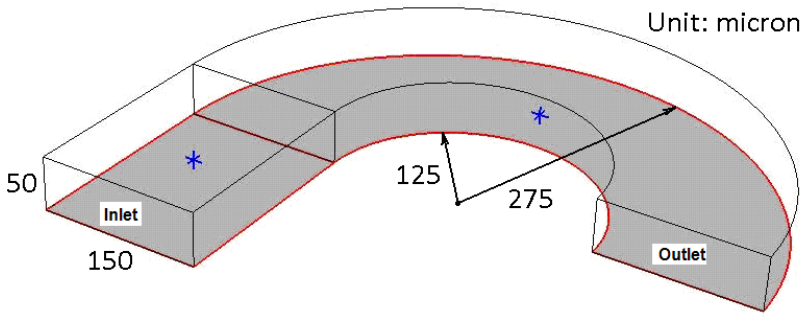

Fig. 4-10 Schematic of curved channel

Inlet flow velocity is 0.1 m/s; diameter of particle is 20 μm; particle Reynolds number thus is 2. Particle is released at the starting point of the bent centerline.

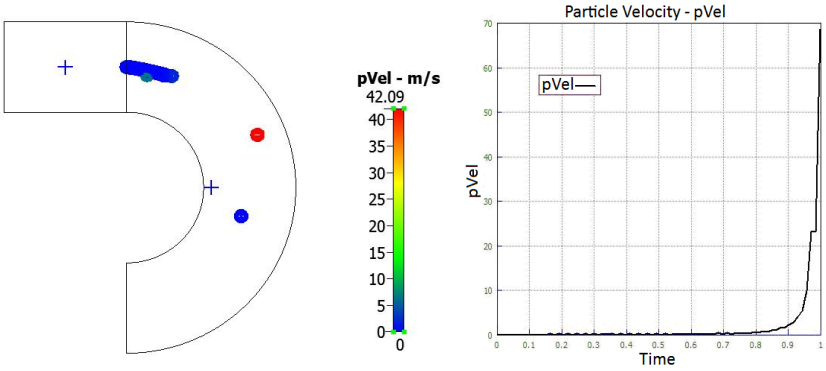

(a) Without FF and FCC approach

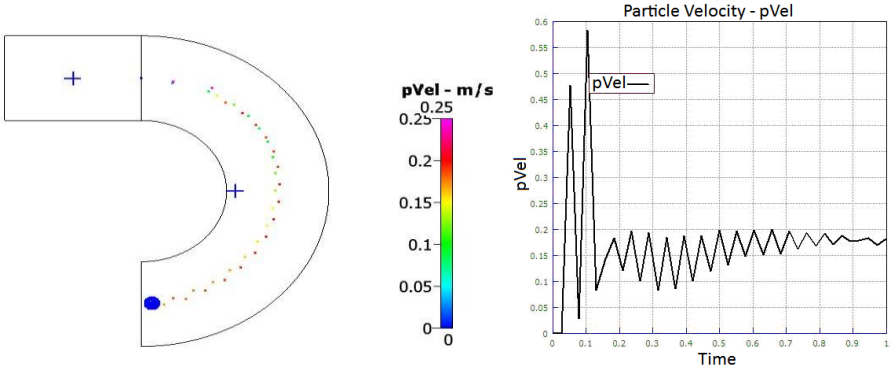

(b) With FF-FCC, time step Δ*t*=1E-4 s

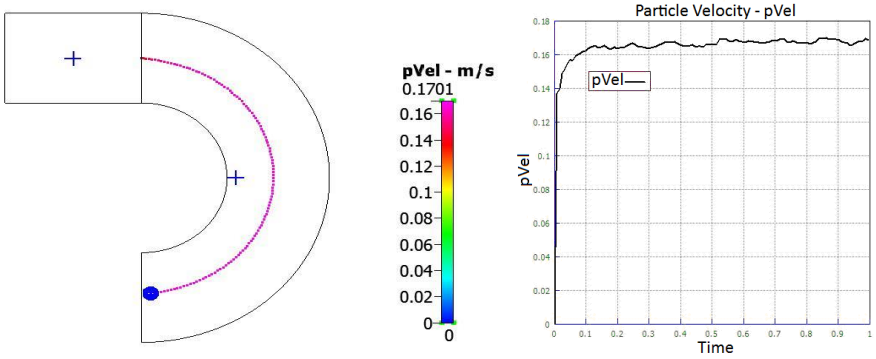

(c) With FF-FCC approach, time step Δ*t*=1E-5 s

Fig. 4-11 Particle in 3D channel with 180° bend

However even if time steps are small enough, across a wide range of particles velocity oscillations occur according to further investigations, which are shown below. This is why a time-adaptive FCC is indispensable. Since different forms of FCC make tremendous difference, the right form cannot be chosen randomly.

Through the comparison of 6 FCC implementations, the optimal form is verified.

(1) Without FCC (FCC=1)

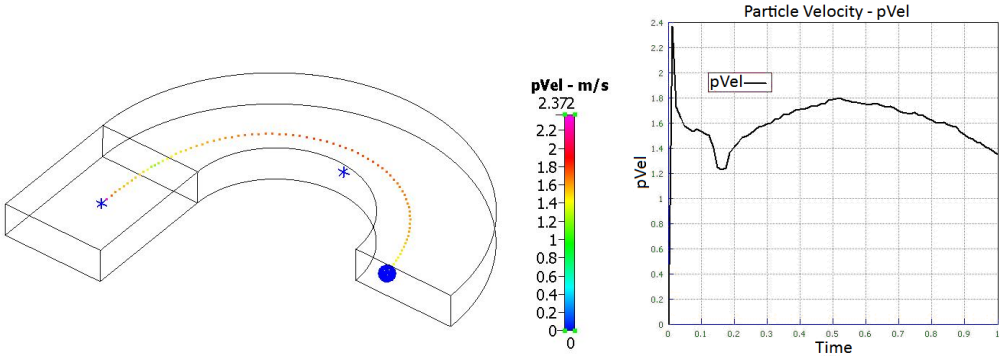

(a) Inlet velocity=1.0 m/s; time step Δt =10E-6s

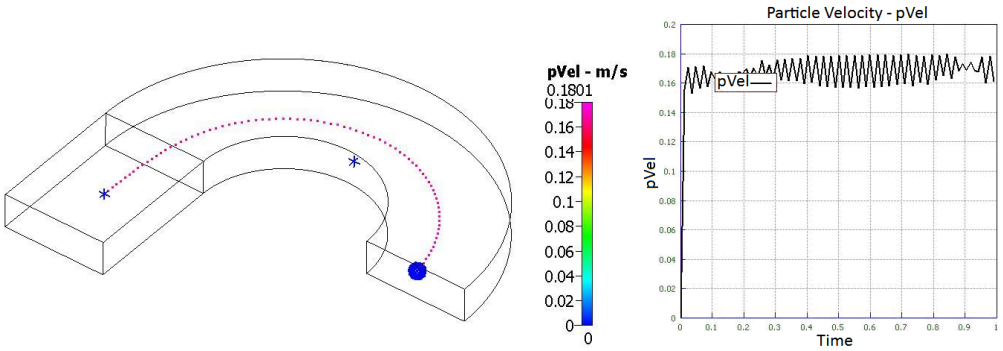

(b) Inlet velocity=0.1 m/s; time step Δt =10E-5s

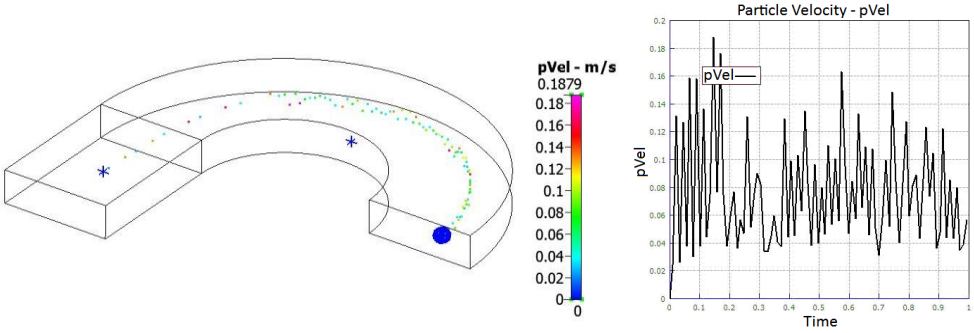

(c) Inlet velocity=0.01 m/s; time step Δt =10E-4s

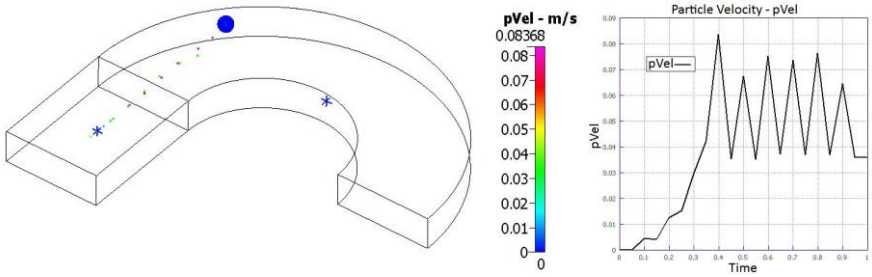

(d) Inlet velocity=0.001 m/s; time step Δt =10E-3s

Fig. 4-12 Trajectories and velocity without FCC approach (FCC=1)

The simulations just adopting Frozen Flow approach show evident velocity oscillations. When the external time step increases to 10E-4s, it leads to artificial trajectory oscillations, while when external time step is reduced to 10E-5s, the particle velocity is still with constant oscillation. This is due to the over-exerted local flow impact when the particle is accelerated, shown in Fig. 4-12.

To derive other FCC formula forms with physical meaning, the situation is considered in which a particle with initial velocity v_{P0} is accelerated merely by fluid with a constant local flow velocity v_f. Its velocity develops with time as $v_{\mathrm{P}} = v_{\mathrm{P0}} + v_f(1-e^{-\frac{t}{\tau_{\mathrm{S}}}})$, where $\tau_{\mathrm{S}} = \frac{\rho_{\mathrm{P}} d_{\mathrm{P}}^{\,2}}{18\mu}$ is particle relaxation time. According to the Galilean invariance, the particle velocity in the reference frame moving with the velocity of v_{P0} has the expression $v_{\mathrm{P}}' = v_f(1-e^{-\frac{t}{\tau_{\mathrm{S}}}})$. Thus we have:

(2) FCC= $(1-e^{-\frac{\Delta t}{\tau_{\mathrm{S}}}})$

This form stems directly from the particle velocity expression $v_{\mathrm{P}}' = v_f(1-e^{-\frac{t}{\tau_{\mathrm{S}}}})$. However through excessive testing, it's demonstrated to be incapable of dealing with low flow velocity because the flow correction is too rigid for large time steps, thus huge oscillations emerge. The results are shown in Fig. 4-13.

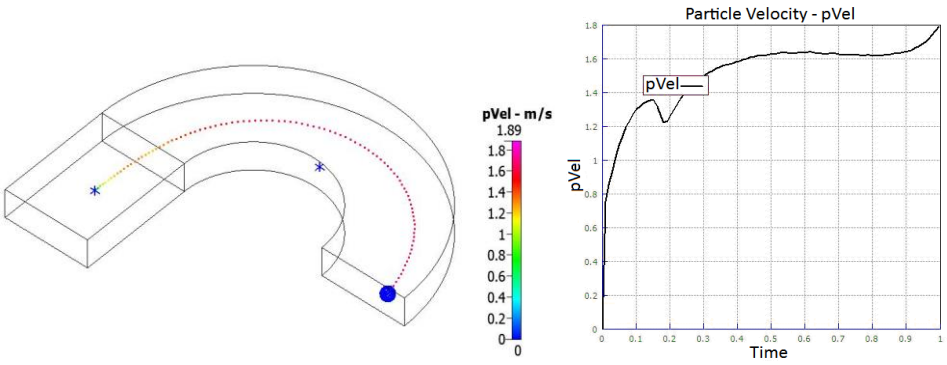

(a) Inlet velocity=1.0 m/s; Time step=10E-6s

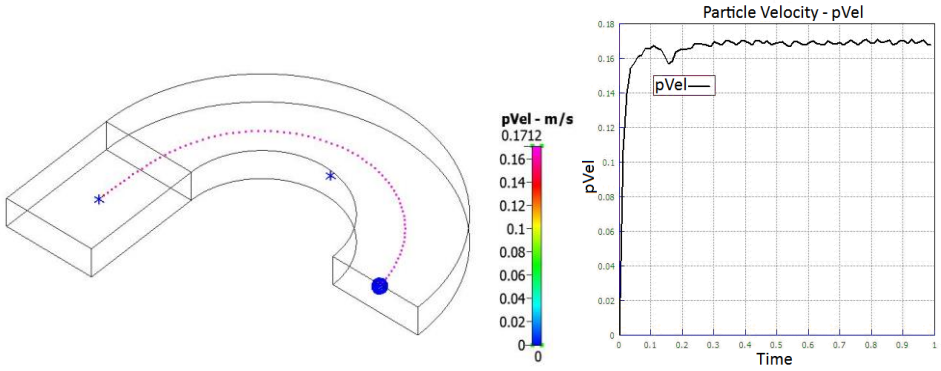

(b) Inlet velocity=0.1 m/s; Time step=10E-5s

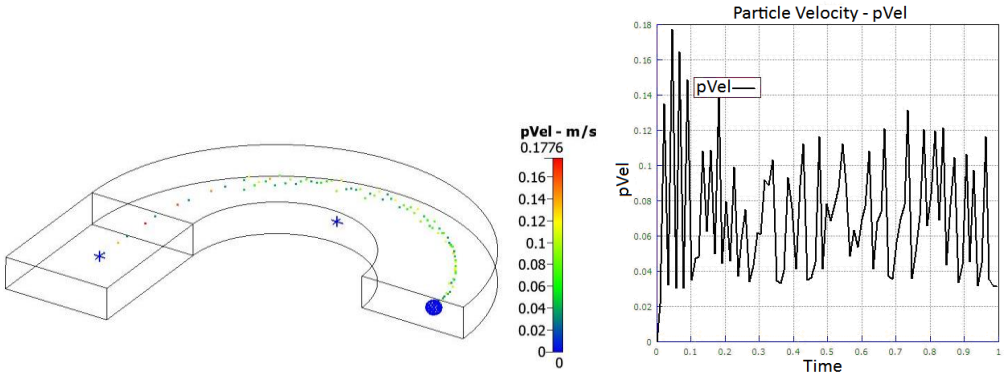

(c) Inlet velocity=0.01 m/s; Time step=10E-4s

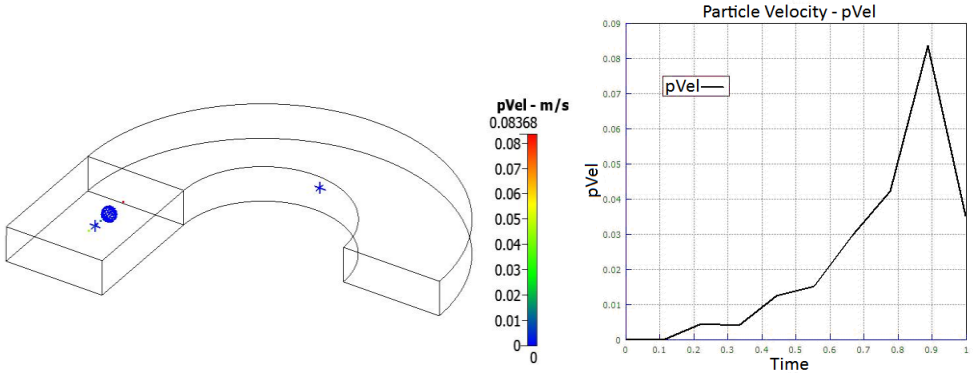

(d) Inlet velocity=0.001 m/s; Time step=10E-3s

Fig. 4-13 Trajectories and velocity with FCC-(2)

(3) FCC= $\frac{1}{2}\frac{\tau_S}{\Delta t}(1-e^{-\frac{\Delta t}{\tau_S}})$

To account for and quantify the time-average effect of local flow velocity: $\overline{\Delta U}=\frac{\int_0^{\Delta t}\Delta U dt}{\Delta t}=\frac{\int_0^{\Delta t}(v_f-v_p)dt}{\Delta t}=v_f\frac{\tau_S}{\Delta t}(1-e^{-\frac{\Delta t}{\tau_S}})$. At the same time we consider the space-average effect of local flow, by multiplying by a coefficient of $\frac{1}{2}$ which is to linearly

take the midpoint value of two instants in time: FCC=$\frac{1}{2}\frac{\tau_S}{\Delta t}(1-e^{-\frac{\Delta t}{\tau_S}})$. However, although this FCC form shows improved results in terms of eliminating oscillations, it is still incapable of dealing with low flow velocity because the flow influence becomes too weak for large time step this time, which makes the particle unresponsive to crossflow, which would result to a change in direction, shown in Fig. 4-14 (d).

(4) FCC=$\sqrt{\frac{1}{2}\frac{\tau_S}{\Delta t}}(1-e^{-\frac{\Delta t}{\tau_S}})$

To address the problem incurred by FCC form (3), this square root correction is to strengthen the flow influence when it comes to low flow velocity (large time step). However, instead it turns out to be incapable of dealing with high flow velocity (small time step) since flow correction turns out to be underestimated, which makes the particle collide with the outer wall, which is shown in Fig. 4-15 (a).

(5) FCC=e^{-1}=0.3679

A constant value-type of FCC form has also been tested. As expected, this form is incapable of dealing with high flow velocity because the flow correction is too inflexible for the small time step case, resulting in (mild) oscillations, shown in Fig. 4-16 (a).

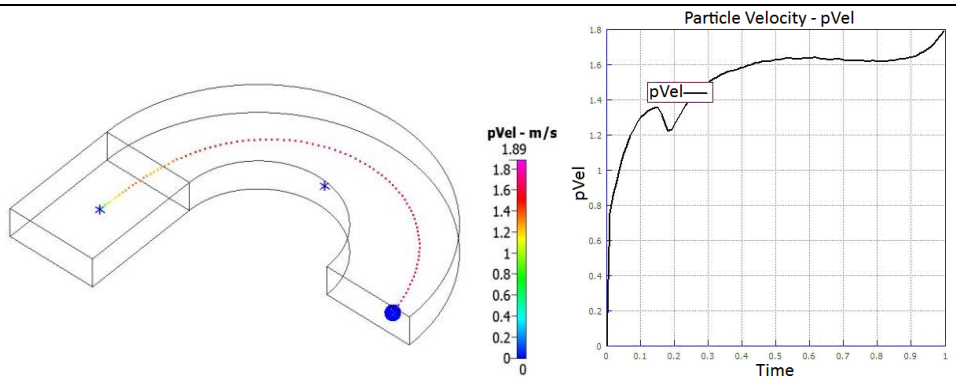

(a) Inlet velocity=1.0 m/s; Time step=10E-6s

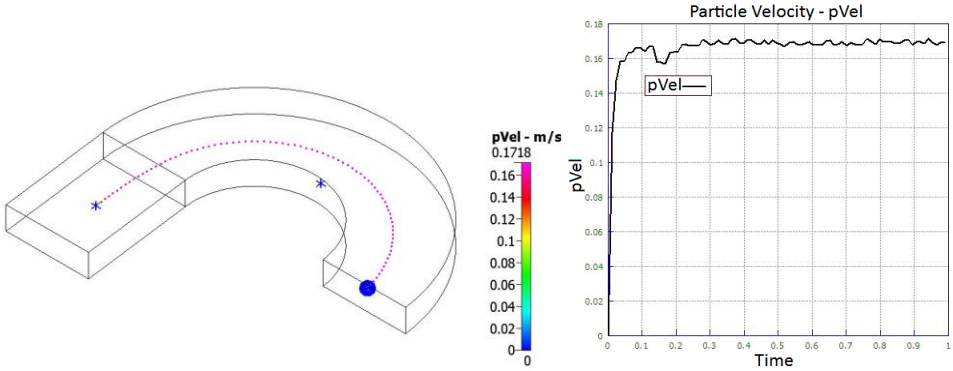

(b) Inlet velocity=0.1 m/s; Time step=10E-5s

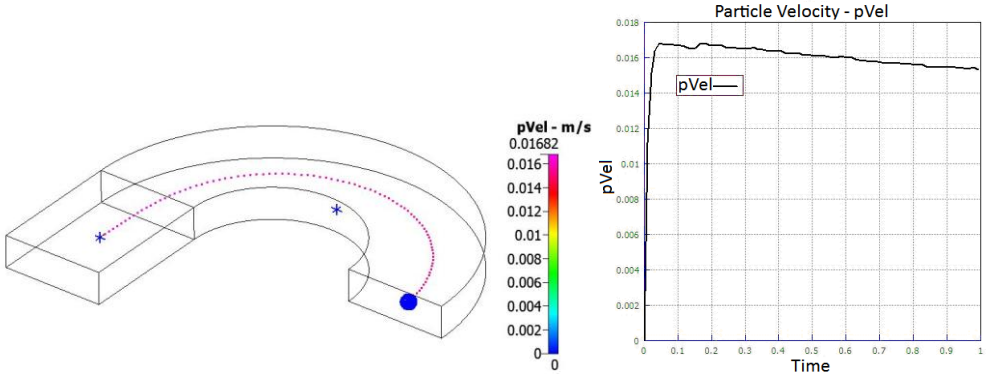

(c) Inlet velocity=0.01 m/s; Time step=10E-4s

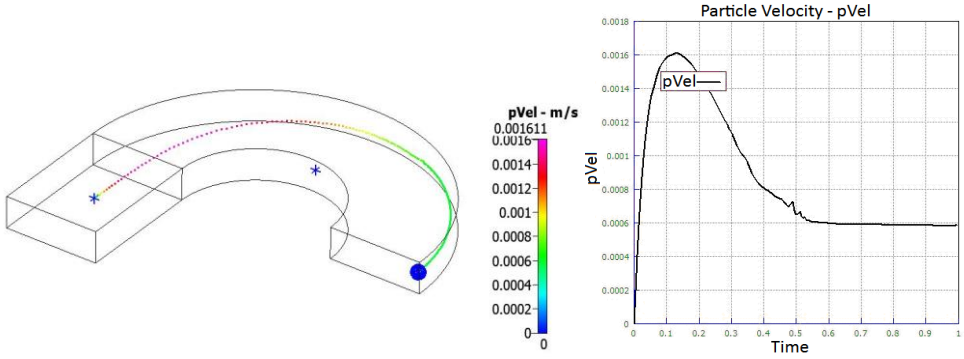

(d) Inlet velocity=0.001 m/s; Time step=10E-3s

Fig. 4-14 Trajectories and velocity with FCC-(3)

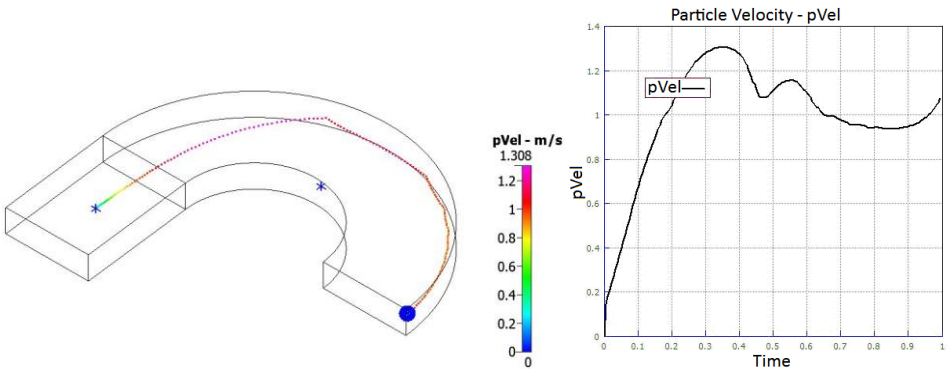

(a) Inlet velocity=1.0 m/s; Time step=10E-6s

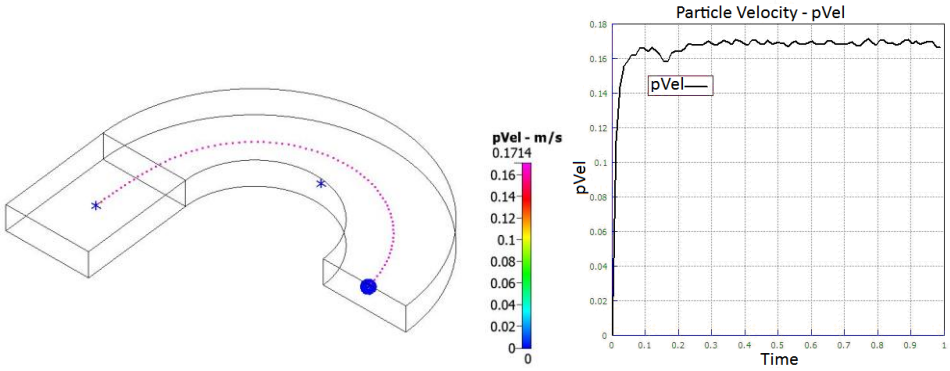

(b) Inlet velocity=0.1 m/s; Time step=10E-5s

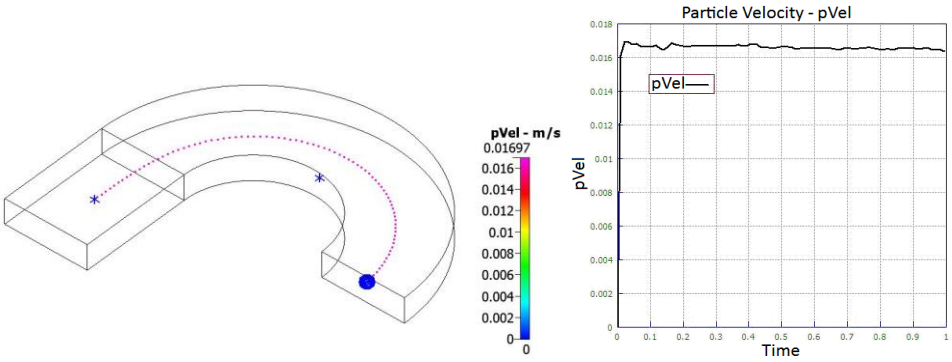

(c) Inlet velocity=0.01 m/s; Time step=10E-4s

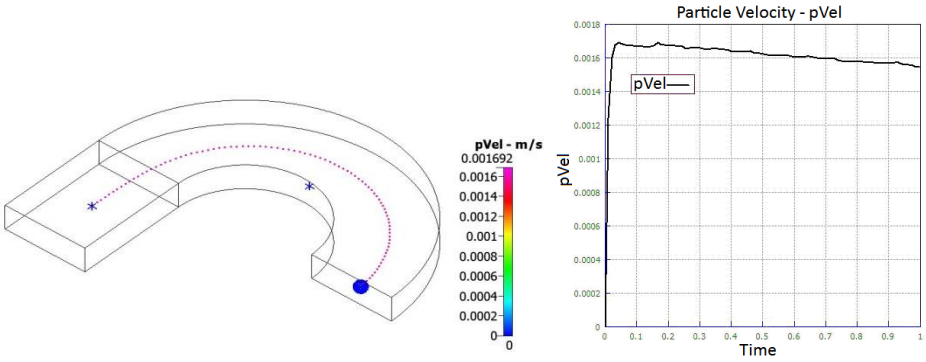

(d) Inlet velocity=0.001 m/s; Time step=10E-3s

Fig. 4-15 Trajectories and velocity with FCC (4)

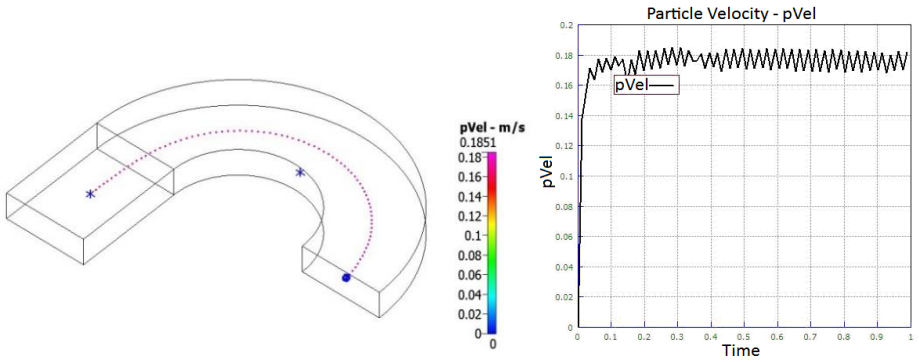

(a) Inlet velocity=0.1 m/s; Time step=10E-5s, d_P=10 μm

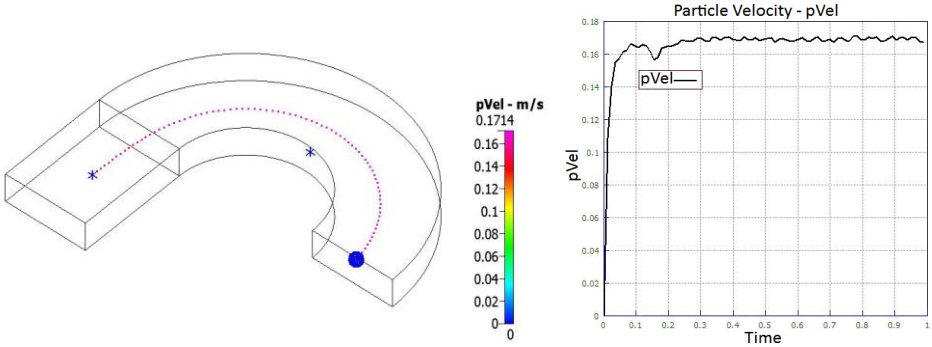

(b) Inlet velocity=0.1 m/s; Time step=10E-5s

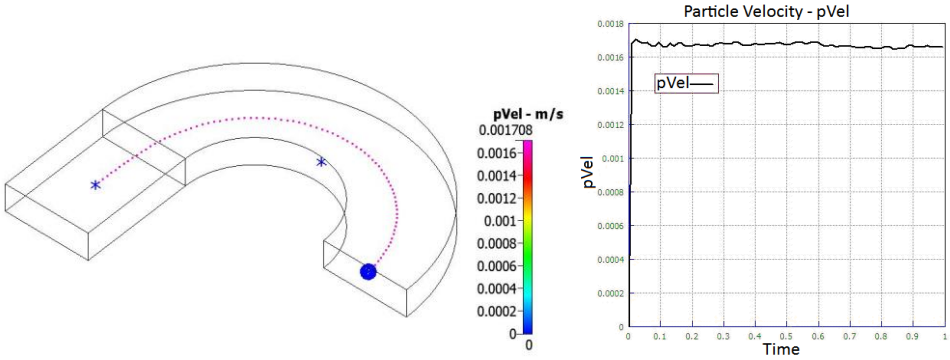

(c) Inlet velocity=0.01 m/s; Time step=10E-4s

Fig. 4-16 Trajectories and velocity with FCC-(5)

(6) FCC=$\frac{1}{2}e^{-1}$=0.1839

To improve the FCC form (5), a coefficient $\frac{1}{2}$ is multiplied. However this causes problems under high flow velocity condition. The flow correction becomes too relaxed this time at the small time step, which causes particles to collide with the outer wall, shown in Fig. 4-17.

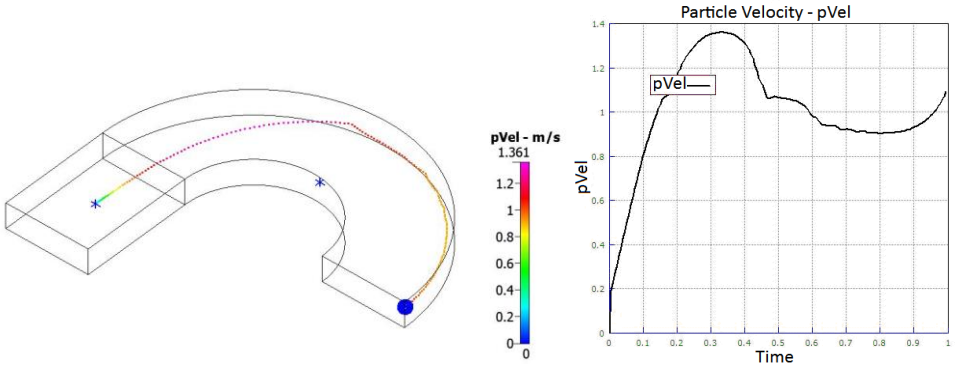

(a) Inlet velocity=1.0 m/s; Time step=10E-6s

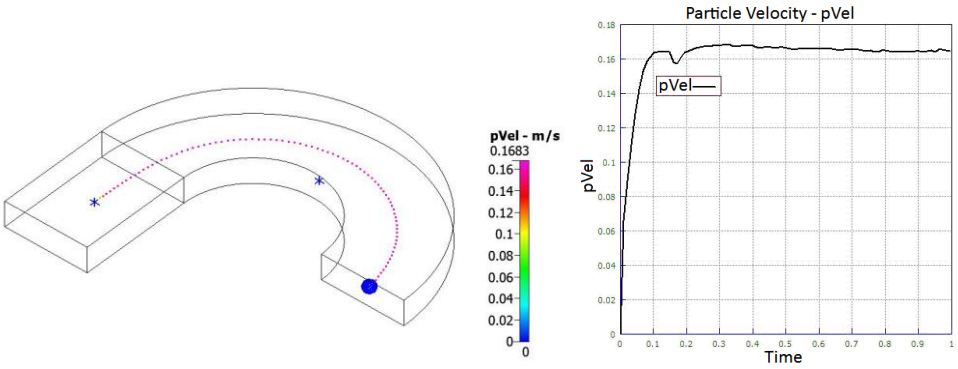

(b) Inlet velocity=0.1 m/s; Time step=10E-5s

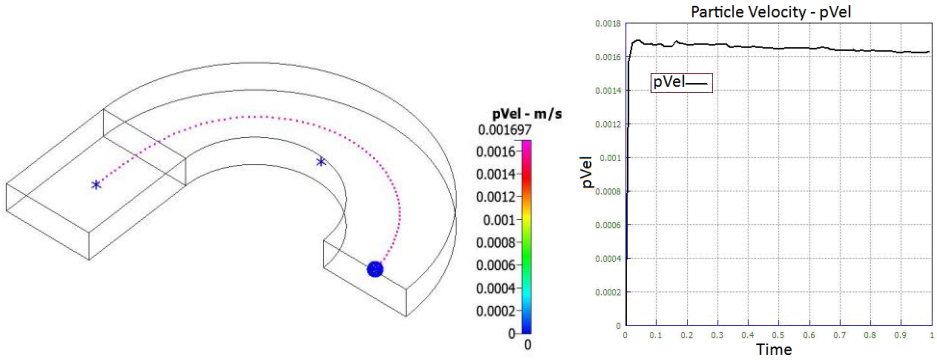

(c) Inlet velocity=0.001 m/s; Time step=10E-3s

Fig. 4-17 Trajectories and velocity with FCC-(6)

By so far, different FCC forms have been tested. The results above demonstrate that, although there is promise in the technique, since it allows for computations that are realistic and feasible in terms of cost, the results are not of general enough validity. Constant coefficients are proved to be unsuitable, while relaxation-based formulations lead to over-applied or under-applied flow influence on the particle. Thus a continuous piecewise function is proposed and tested:

$$(7)\ \mathrm{FCC}=\begin{cases}\frac{1}{2}e^{-\frac{\Delta t}{\tau_S}}, \Delta t \le \tau_S \\ \frac{1}{2}e^{-1}, \Delta t > \tau_S\end{cases}$$

This form works very well through a wide range of flow conditions, as demonstrated in Fig. 4-18. By comparison, this form of FCC can capture the particle movement accurately (without collisions with channel walls) and smoothly (without artificial oscillation) in a wide range of flow velocities and time steps (1 - 0.001m/s; $10E^{-6}$ - $10E^{-3}$s). Thus for all subsequent work, this particular FCC scheme is adopted. After this preliminary confirmation regarding initial plausibility of the results obtained, within a practical computational cost framework, we shall proceed to validate the method by comparing our results with experimental measurements.

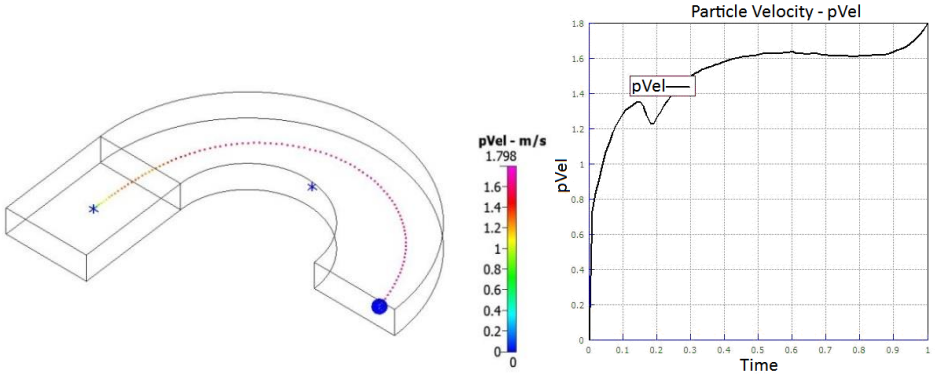

(a) Inlet velocity=1.0 m/s; Time step=10E-6s

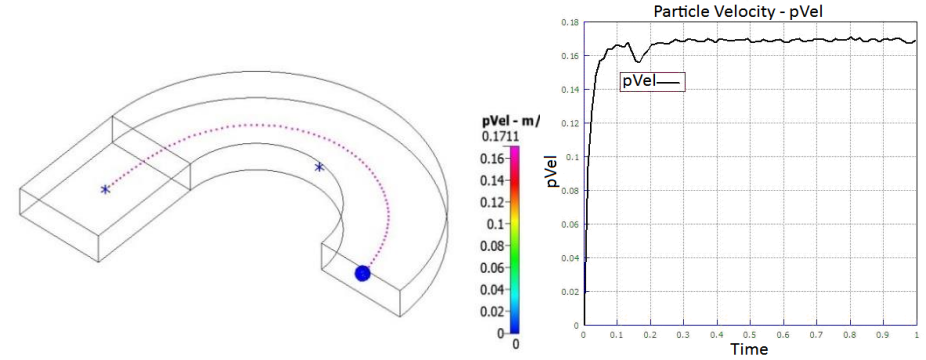

(b) Inlet velocity=0.1 m/s; Time step=10E-5s

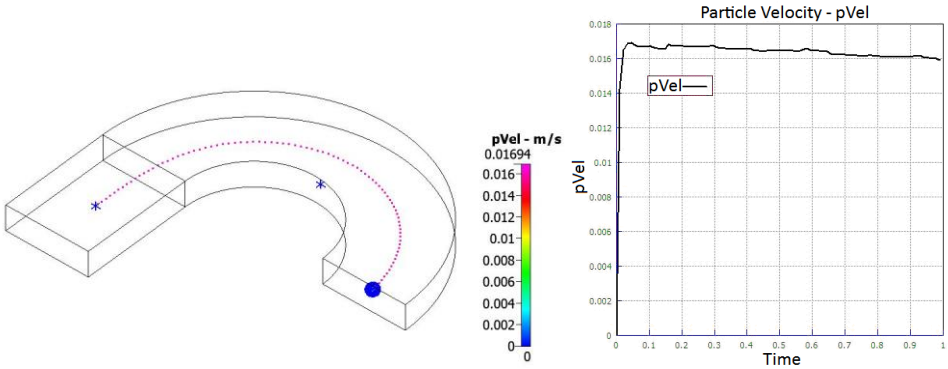

(c) Inlet velocity=0.01 m/s; Time step=10E-4s

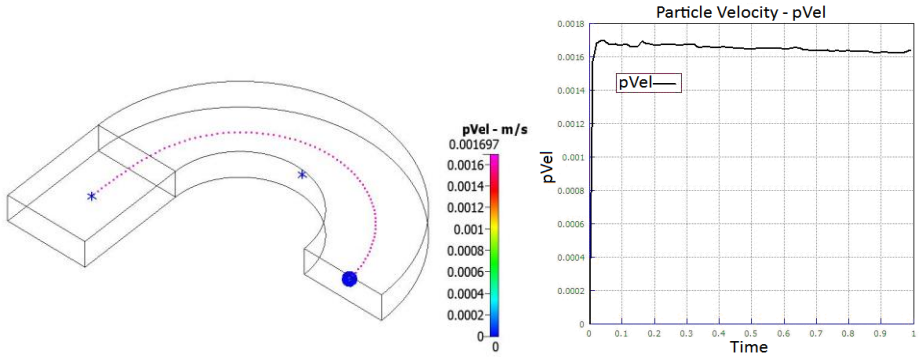

(d) Inlet velocity=0.001 m/s; Time step=10E-3s

Fig. 4-18 Trajectories and velocity with FCC-(7)

4.2.2 Particle rotation

When particle rotation is computed, without adopting the developed rationale $FCC_{Rotation}$, the computations often collapse or diverge. By using $FCC_{Rotation}$ derived in chapter 3, simulations can be run successfully. The results show that without considering particle rotation, the particle trajectories are normally the same as the cases considering rotation, since the trajectories are nearly overlapping. This is attributed to the fact that the spherical particles we are examining, in the microchannels we are testing, do not undergo significant rotational motions. However, there's a special situation when particles approach to the channel walls, the near-wall shear is very substantial and even particle-wall collision may be involved to increase the particle rotational speed. In such cases the particle rotational speed increases dramatically to induce a significant Magnus force. Fig. 4-19 shows the simulation results of a 40 μm particle drifted in a curved channel with inlet velocity of 1m/s. The blue trajectory represents a path without rotation computation, while the red trajectory denotes the result considering rotation and adopting $FCC_{Rotation}$. With rotation, when the particle gets closer to the wall, its angular velocity ω (3 components for 3D, however only the one in the direction perpendicular to the plane and pointing out is shown here) increases dramatically several times as it is at the middle of channel, because the shear gradient near the wall is much higher than at the central area. Magnus force is in the direction of $\vec{\omega}\times\vec{v}$, where $\vec{v}$ is the particle velocity relative to the flow, which is negative in the flow direction. Thus Magnus force should point to the inner wall, which agrees with this simulation result. In this case, the ratio of

Magnus force to drag force $R_{MS} = \frac{d_p^2}{24}\frac{\rho}{\mu}\Omega$ can reach 2, while normally this ratio is far less than 1 without particle-wall collision. After bouncing back, the angular velocity of the particle decreases, because it's moving away from the wall again where the shear drops.

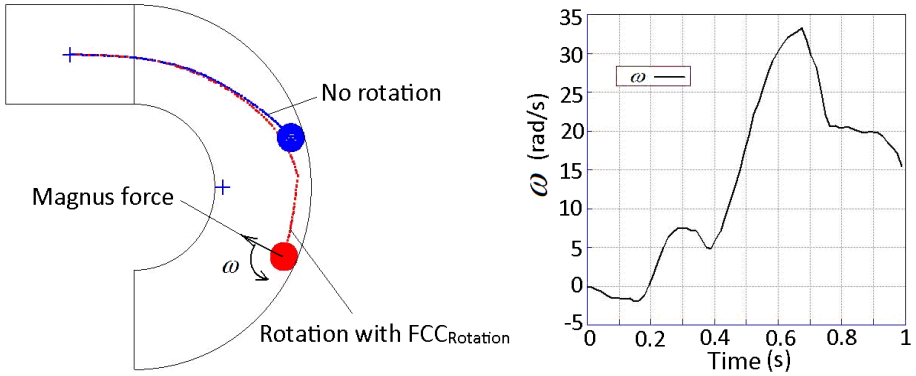

Fig. 4-19 Rotation influence on particle trajectory and angular velocity

Because the timescale is short in the above situation (total time for the whole process is 5E-4 s), even 1 rotation of the particle leads to huge angular velocity.

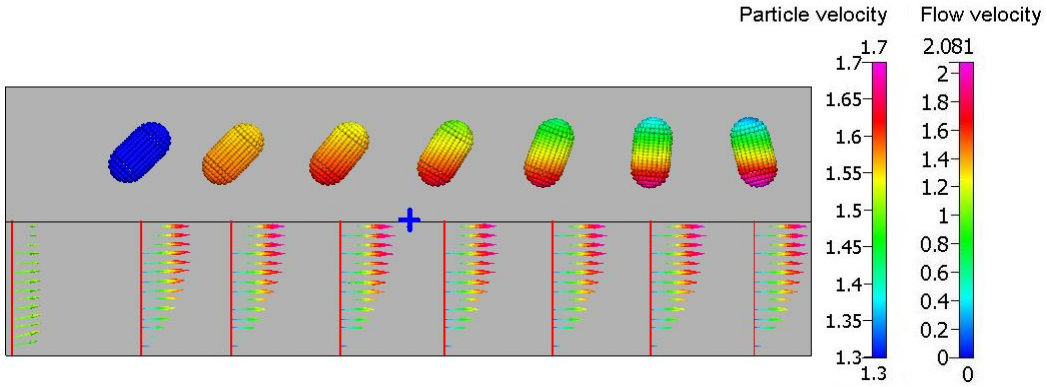

Fig. 4-20 Cap-cylinder particle rotation in rectangular channel

Another example of a 3D cap-cylinder with maximum span of 1μm drifting in a straight channel illustrates this effect: the angular velocity can even reach 300,000 rad/s. Flow enters in the left side with uniform inlet flow velocity of 1 m/s and develops a paraboloid velocity distribution. This case also demonstrates capacity of

the methodology to simulate arbitrary shaped particles, shown in Fig. 4-20. Time interval between adjacent snapshots is 1E-6 s and the whole timescale is about 6E-6 s.

4.2.3 Validation via sedimentation studies

There is a substantial volume of experimental work examining particle sedimentation and terminal velocity of particles falling in a liquid in the influence of gravity. Such experiments offer excellent ground for validating our computational method, since they represent many, if not all of the aspects of the flows involved and the measurements are detailed, cross-checked and thus accurate.

Terminal settling velocity doesn't depend on the initial velocity of a settling particle, thus particle initial velocity is set to be zero. We firstly test 50 μm glass particle with density of 2488 kg/m^3. Due to the fact that the Reynolds number is at most 0.1 in this case, terminal settling velocity can be roughly calculated by Stokes' law, $v_S = \frac{2g(\rho_P - \rho)r^2}{9\mu}$, which is $v_S = 2.03\times10^{-3}$ m/s. Different time integration schemes have been adopted, including forward Euler and Verlet. It's found that Verlet integration with sub-time-step two orders of magnitude smaller than the external timestep can achieve excellent accuracy, comparable to a direct computation with 100 times smaller timestep –leading to a roughly hundred-fold speedup for the same result. Fig. 4-21 shows the comparison of settling velocity development between Stokes' law and numerical simulations by our approach. Terminal settling velocity for this 50 μm glass particle settling in 20°C water is 2.05×10^{-3} m/s by our simulation which adopts sub-time-step 10E^{-10}s. This value just has an error of 1.46% in

comparison to the theoretical value $v_S = 2.02\times10^{-3}$ m/s predicted by Stokes' law. The experimental work [145] shows that the exact same particle has a terminal settling velocity of 1.98×10^{-3} m/s in 20 °C water, which is slightly smaller than our result with an error of 3.41%. The slight error can be due to a small uncertainty regarding the shape of glass microparticles; as the authors of that study report, such particles are never perfect spheres. Shape correction would make a difference in drag force: $F_D = 3\pi\mu d_p V_p \chi$, where χ is shape correction coefficient, which is a measure for roundness of the sphere. When the ideal particle is perfectly spherical, $\chi = 1$, while when the shape of the particle is not perfect sphere $\chi > 1$ which implies the incurred increase of drag force. In this way the terminal settling velocity of a real non-sphere particle $v_S = \dfrac{2g(\rho_P - \rho)r^2}{9\mu\chi}$ would be smaller than the theoretical value for a perfect sphere.

Size effect on settling velocities has also been investigated. Though the terminal velocities agree with Stokes' law, particles tend to accelerate more slowly in our simulation for our method also considers added mass effect intrinsically. Relaxation time for 50 μm $\tau_S = \dfrac{\rho_P d_P^{\,2}}{18\mu}$ is 1.4×10^{-4} s, while 5 μm and 500 μm particles have respectively 100 times lower and higher value. For the 500 μm particle, the terminal velocity reaches $v_S = 2.03\times10^{-1}$ m/s, which makes the Reynolds number approach 250. In this region, the flow pattern obviously deviates from Stokes flow. Settling velocity of the simulation result is smaller than that predicted by Stokes' law at the beginning, which is shown in Fig. 4-21 (d). This indicates the real drag coefficient is larger than

$\frac{24}{\mathrm{Re}}$, which demonstrates that a correction for the inertial term should be added to Stokes' law, such as the Oseen's approximation [146]. Afterwards the settling velocity develops and exceeds the theoretical value, possibly because the kinetic energy of this large particle influences directly the entire volume of fluid inside the vertical channel (see Fig. 4-22) leading to a non-zero downward average velocity. Due to higher order accuracy of the Verlet integration scheme, it is adopted for all cases.

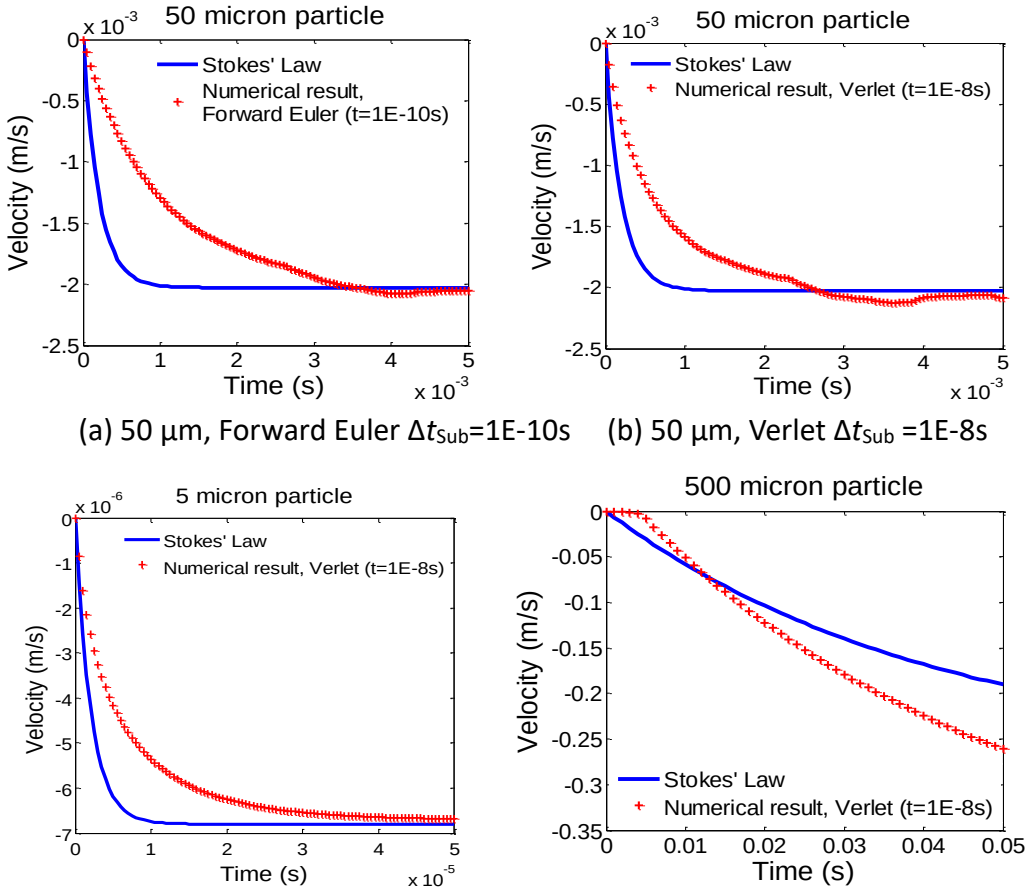

(a) 50 μm, Forward Euler Δt_{Sub}=1E-10s (b) 50 μm, Verlet Δt_{Sub} =1E-8s

(c) 5 μm, Verlet Δt_{Sub} =1E-8s (d) 500 μm, Verlet Δt_{Sub} =1E-8s

Fig. 4-21 Theoretical and simulation results of micro particle settling velocity

Another experiment work [147] adopting particle image velocimetry (PIV) investigated the bottom wall confinement effect on a settling sphere. A nylon particle with diameter d_{p}=15 mm and density ρ_{p}=1120 kg/m^3 was released in a depth×width

×height=100×100×160 mm container filled with silicone oil (ρ_f=970 kg/m^3, dynamic viscosity if 0.373 Pa□s). The initial position of the sphere is 120 mm from the bottom of the tank. Fig. 4-22 shows different time (t=0.01s, 1s, 2s, 3s) snapshots of particle settling, highlighting its impact on flow field and pressure distribution on the walls. A pair of symmetric vortices triggered by the settling particle, predicted by our results, is verified convincingly by the PIV measurement in the experiment, which is shown in Fig. 4-23. Fig. 4-24 shows the comparison of particle trajectory changing with time between the experiment and our simulation. Fig. 4-25 shows the comparison of particle settling velocity. Here, it is pointed out again that our simulation result for terminal settling velocity is slightly larger than the experimental value, which is probably due to shape correction, the same reason as for the last case. To verify this, particles with slightly different sizes have been tested, trying to replicate the inevitable slight dispersion of sizes that an experimental measurement would entail. These particles are respectively d_p=14.5, 14.85, 15.15 and 15.5 mm, covering a range of $\pm$3.33% deviation from the standard 15 mm particle. Their settling distance and velocity over time are shown in Fig. 4-26. Especially, when there is a -3.33% error in size(d_p=14.5), the results agree with the experiment well.

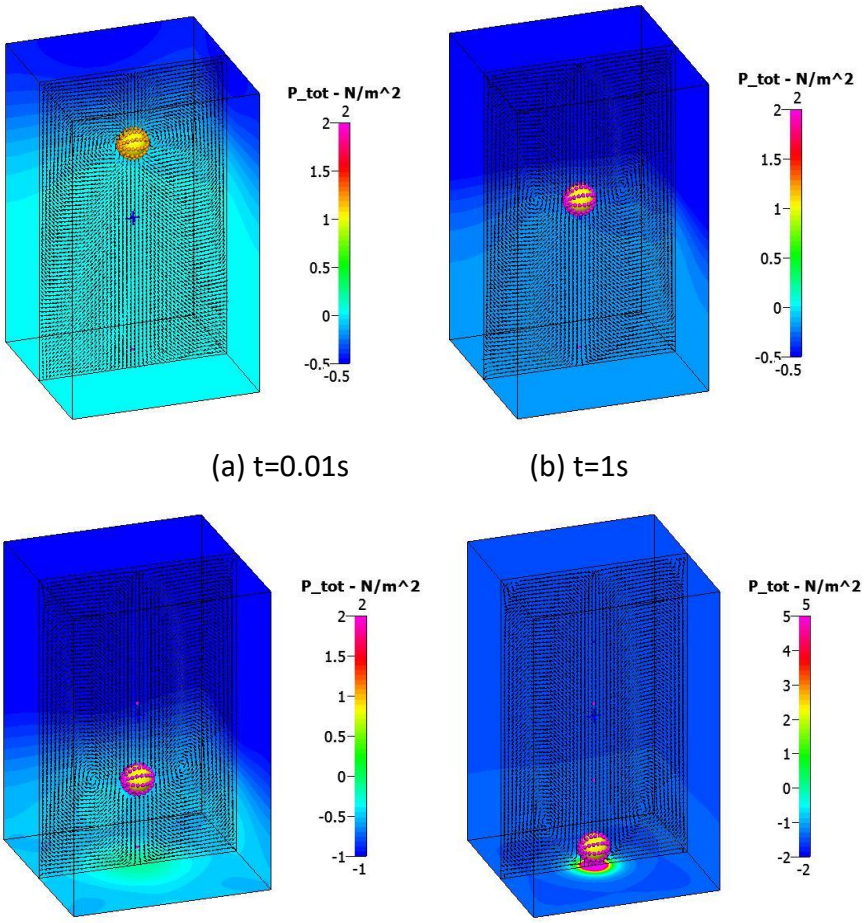

(a) t=0.01s (b) t=1s

(c) t=2s (d) t=3s

Fig. 4-22 Snapshots of particle settling, its impact on flow field and pressure distribution on the walls

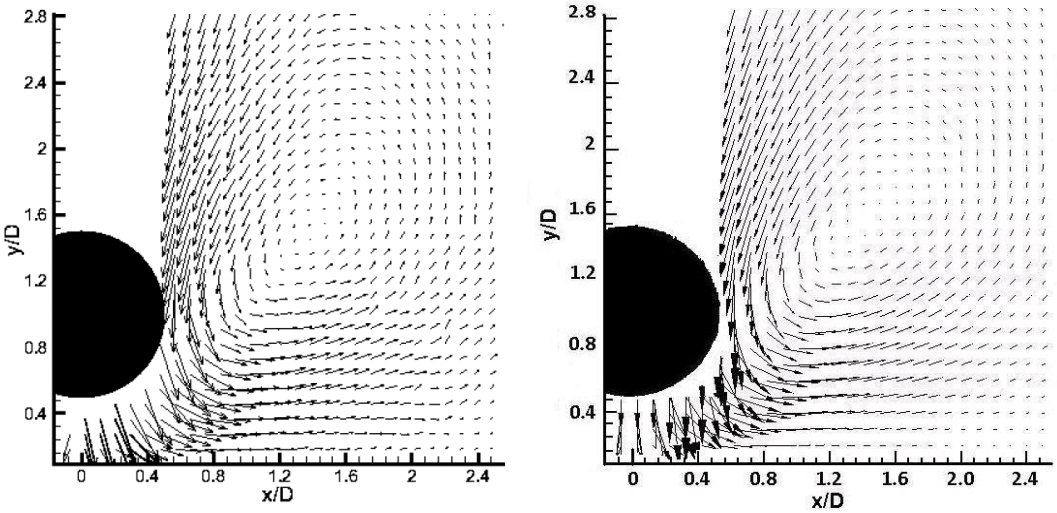

(a) PIV measurement [147] (b) Simulation

Fig. 4-23 Comparison of PIV measurement and simulation for flow field on vertical cross section in the vicinity of particle approaching the bottom wall

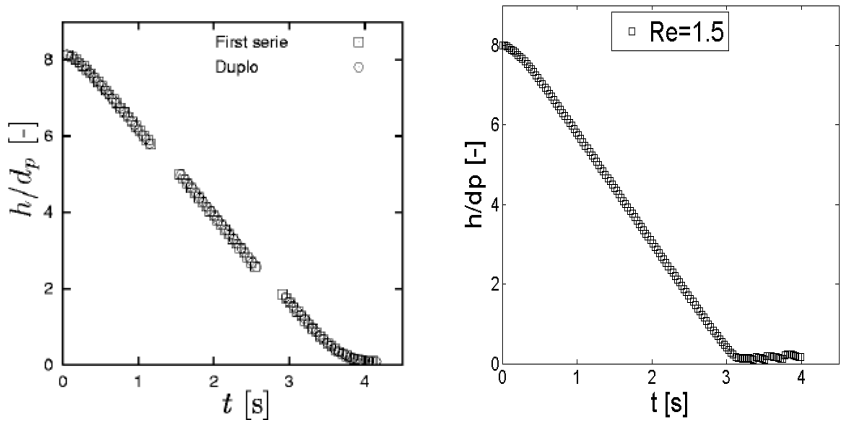

(a) Experiment [147] (b) Simulation

Fig. 4-24 Particle trajectory over time

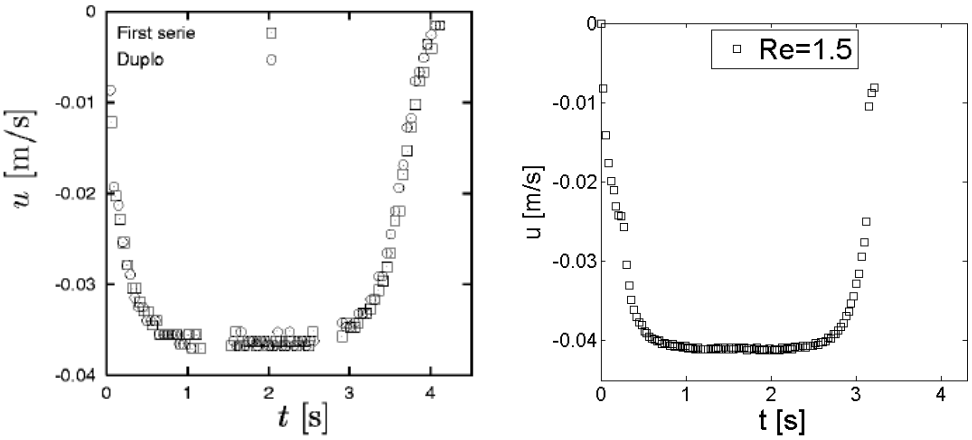

(a) Experiment [147] (b) Simulation

Fig. 4-25 Particle settling velocity over time

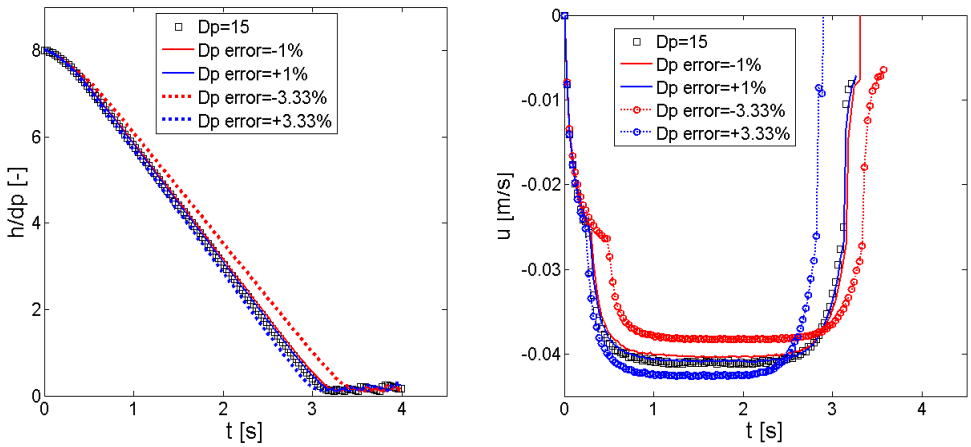

Fig. 4-26 Result sensitivity about particle size

Based on the above, we conclude that the Surface Marker Point method, combined

with the Frozen Flow and Flow Correction Coefficient approach can capture the particle-fluid coupling and evidently depict the 3D particle trajectories influenced by ambient flow (self-induced in this case) and external forces (gravity in this case).

A more complex case is examined next, where 5 particles with diameter of 500 μm and density of 3000 kg/m^3 are released in a vertical channel and driven by gravity. External time step is set to 10^{-4}s. Two particles vertically arranged at lower positions are approaching to each other when falling, which is shown in Fig. 4-27.

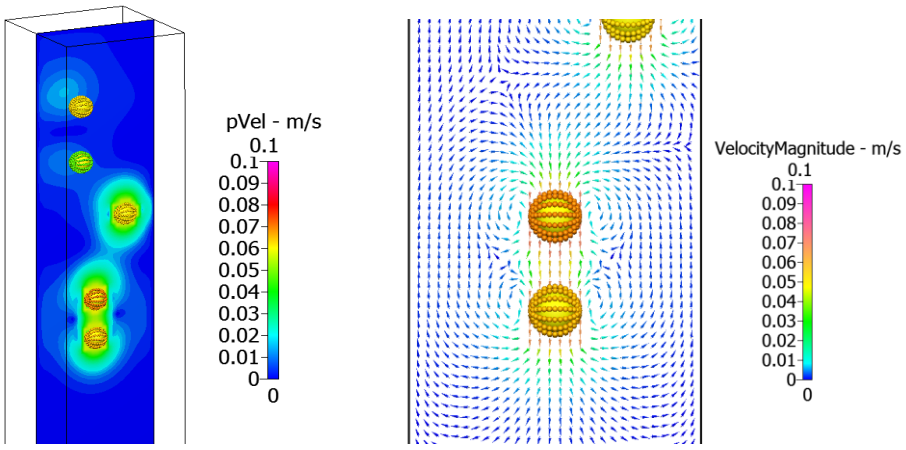

(a) 100th time step

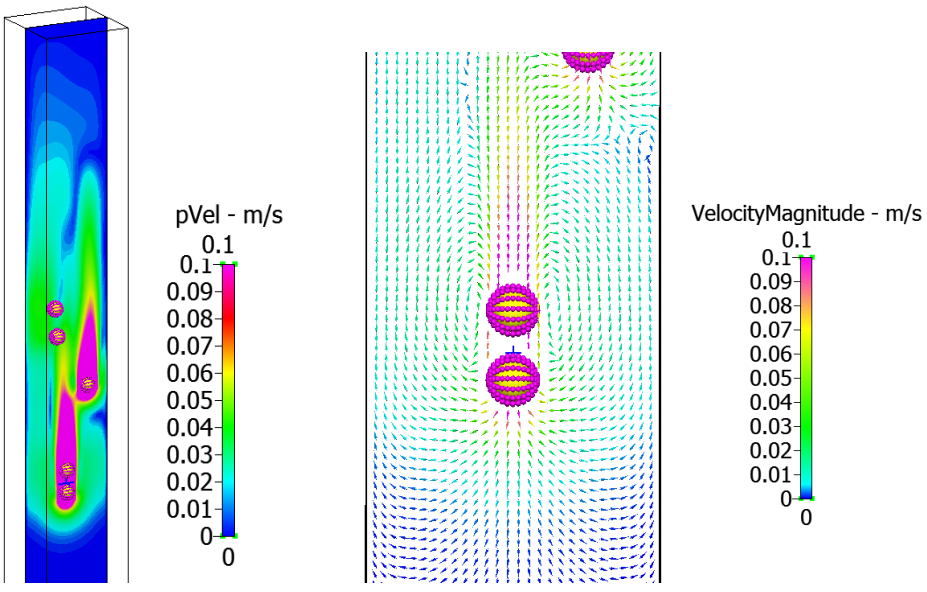

(b) 500th time step

Fig. 4-27 Five particle settling from different initial positions

These two particles induce symmetric vortices in their lateral vicinity. With the distance between them decreasing, two pairs of vortices merge to a single pair, which reveals the mechanism of two particles “kissing” [148].

In summary, we have shown that spatial resolution of complex flows is guaranteed by the grid independence study. Particle-flow coupling as implemented by the Surface Marker Point approach lead to time integration constraints regarding particle motion that we have addressed via the Frozen Flow and Flow Correction Coefficient approach, which largely enhance the simulation time step limit. Time step independence is also assured by verification of both external time step and sub-time-step.

4.3 Comparison with point-particle approximation

As mentioned in chapter 2, conventional particle simulation approaches are based on the point-particle approximation. However, for large-scale particles whose dimensions are comparable with those of the microfluidic channels, this approximation is invalid due to lack of accounting for the volume blockage and the specific shape of particles. Moreover, point particles cannot deal with particle rotation. In this part, the discrete particle method is investigated as a typical and widely adopted point-particle approximation approach, through cases of lift force influencing particle movement. The results are further compared with the simulations adopting our approaches.

In discrete particle method, discrete parcels are tracked by solving Newton’s

equation of motion in a Lagrangian approach:

$$m_{\mathrm{P}} \frac{dv}{dt} = F_{\mathrm{D}} + F_{\mathrm{P}} + F_{\mathrm{L}} + F_{\mathrm{B}}$$

where drag force $F_{\mathrm{D}} = \frac{1}{2}\rho v^2 C_{\mathrm{d}} A$; pressure gradient force $F_{\mathrm{P}} = -\frac{\pi}{6} d_{\mathrm{P}}{}^3 \nabla P$. F_{B} is body force, which can refer to gravity or other external forces. It is important to note that for point particle methods, all forces, including drag force, must be accounted for explicitly through "external" relationships, since the particle on its own, being of zero volume experiences not intrinsic loading from the flow.

For lift force, which is related to velocity gradient, without taking the real particle volume and shape into account, the local velocity gradient cannot be derived properly. Even if the point-particle approximation is accepted, the lift force formula currently derived by Saffman is $\mathbf{F}_{\mathrm{L}} = \mathbf{F}_{\mathrm{S}} = \frac{K\mu}{4} d_{\mathrm{P}}{}^2 \sqrt{\frac{1}{\nu}\left|\frac{1}{\nabla \times \mathbf{U}}\right|}((\mathbf{U} - \mathbf{U}_{\mathrm{P}}) \times (\nabla \times \mathbf{U}))$, is only valid under the assumption of spherical particle moving in a constant shear flow at low particle Reynolds number $\mathrm{Re}_{\mathrm{P}} \ll 1$. Although other derivations of the Saffman force formula have been made, there is not one for arbitrary velocity gradient in complex flow reported.

Also, virtual mass effect can only be taken into account by adopting complicated empirical formula in discrete particle method, while the method developed in Chapter 3 intrinsically addresses all the forces directly.

According to the analysis above, point-particle approximation doesn't suit large-scale particle simulations. In comparison, the approaches adopted in this research are conducting a direct simulation, which solves the particle-flow coupling and derives

the surface forces by surface integral. Thus by our approaches, all of the drag force, pressure gradient force and lift force have been computed directly in the presence of the particle. The following shows the comparison of simulation results of lift force on particles between using point-particle approximation and adopting the approaches we developed.

Firstly, a 2D problem is investigated. A long 2D channel with width of 100 μm ($H = 2R$) is adopted, with inlet flow velocity of 0.1m/s. A particle with diameter d_p =20 μm is released at a position of 35 μm above the channel centre line, above the 'tubular pinch' equilibrium position (around 0.6 of the pipe radius from the centerline, y_{eq}/R =0.6), which is 30 μm above the centre line. This position is also away from the channel inlet to avoid inlet effects. The discrete particle method and our method have both been implemented. Results show that the particle in discrete particle method is constantly approaching to the wall (in the end it collides with the upper wall). On the contrary, our simulation successfully predicted the particle equilibrium position, which agrees well with the experimental observations of tubular pinch effect, shown in Fig. 4-28 and Fig. 4-29. Furthermore, experiments [83] show with the ratio of particle diameter to channel dimension increasing, the equilibrium position will be continuously pushed back toward the central line due to the wall effect. For d_p/R =0.2, y_{eq}/R should be slightly under 0.6. In fact by our simulation y_{eq}/R = 0.590, which agrees with this finding very well.

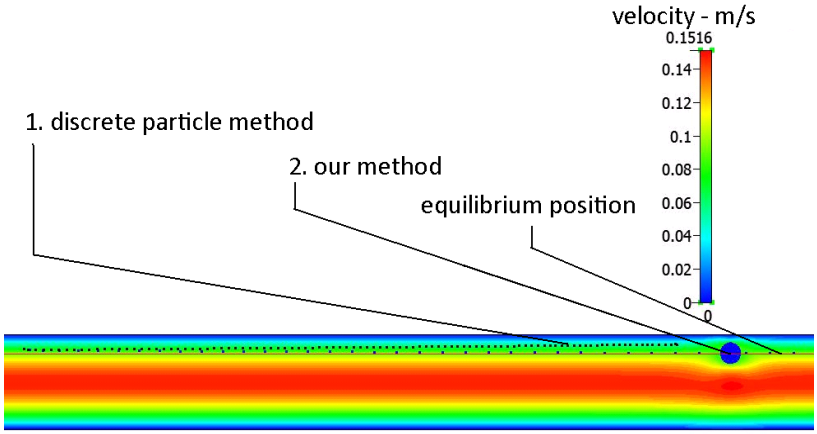

Fig. 4-28 Influence of lift force on particle trajectory in 2D channel

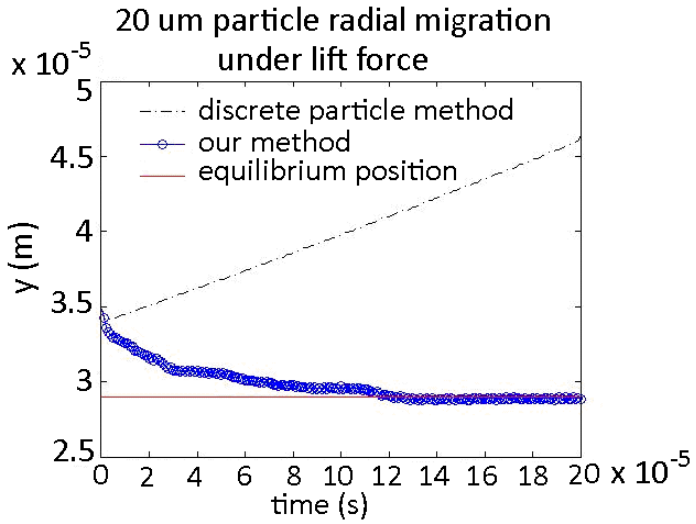

Fig. 4-29 20 μm particle radial migration under lift force

To further prove this, a 10 μm particle is tested. According to the theory mentioned above, its equilibrium position should be closer to the wall, namely y_{eq}/R value should be closer to 0.6. Actually the result by our method shows the equilibrium position for the 10 μm particle is y_{eq}/R =0.596, shown in Fig. 4-30. This means the equilibrium position for smaller particle predicted by our simulation is closer to equilibrium position y_{eq}/R =0.6, which is exactly consistent with the experiments. However, the discrete particle method predicts, incorrectly, the opposite trend.

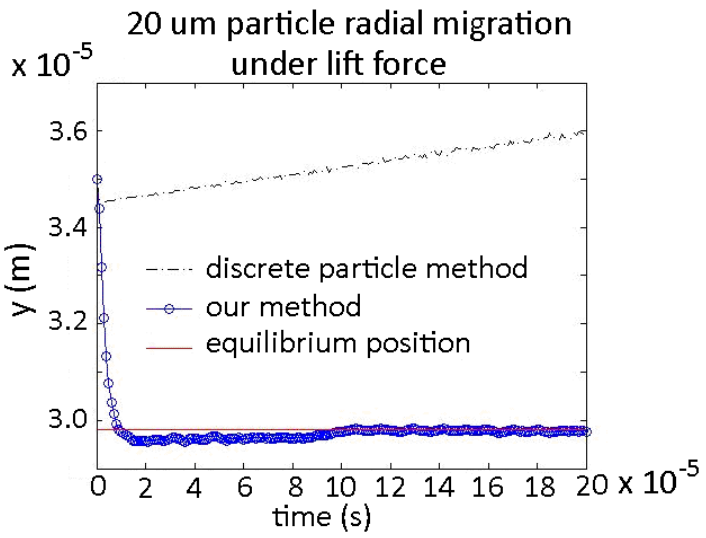

Fig. 4-30 10 μm particle radial migration under lift force

A 3D problem is also investigated. The curved 3D channel shown in chapter 4.2.1 is examined in this case. A 20 μm particle is released at the same position when the flow inlet velocity is 1 m/s and 0.1 m/s.

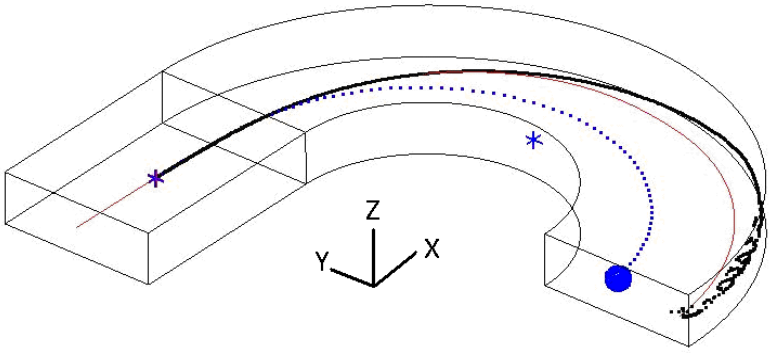

(a) Inlet velocity 1 m/s

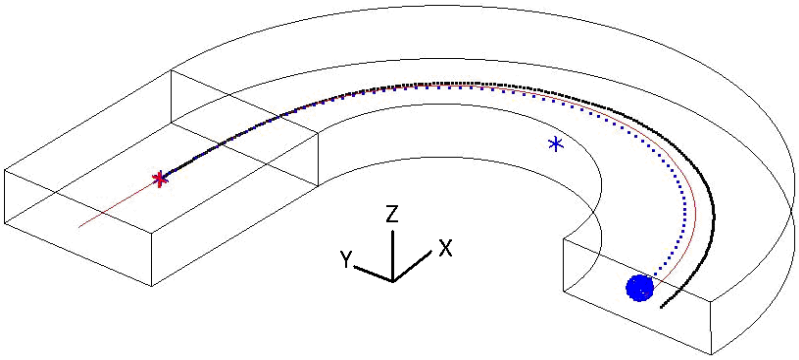

(b) Inlet velocity 0.1 m/s

Fig. 4-31 20 μm particle in curved 3D channel, compared with the discrete particle approach

Fig. 4-31 (a) shows that the discrete particle method predicts a particle trajectory with artificial scattering and collision with the outer wall. Fig. 4-31 (b) demonstrates that in the influence of the Dean flow vortices, the actual particle trajectory has an inward offset due to particle vertical span exposed to the inward secondary flow, which is predicted by our approach.

In this case the influence of the initial release position is studied. With the same flow inlet velocity 0.1m/s, 10 μm particles are respectively released at initial positions 5 μm (point A) and 10 μm (point B) above the horizontal mid-plane. Firstly the results by discrete particle method indicate that this approach fails to capture the particle equilibrium position, which is shown in Fig. 4-32.

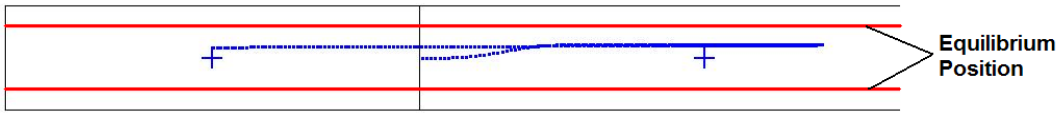

(a) 5 μm above the mid-plane

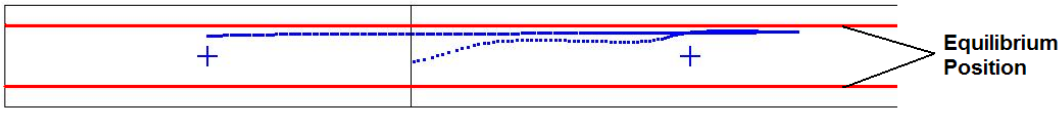

(b) 10 μm above the mid-plane

Fig. 4-32 10 μm particle released above the mid-plane by discrete particle method

In comparison, the trajectories of both 10 μm (termed as 'D10') and 20 μm particles (termed as 'D20') are investigated by our method. They are also released at initial positions 5 and 10 μm above the mid-plane.

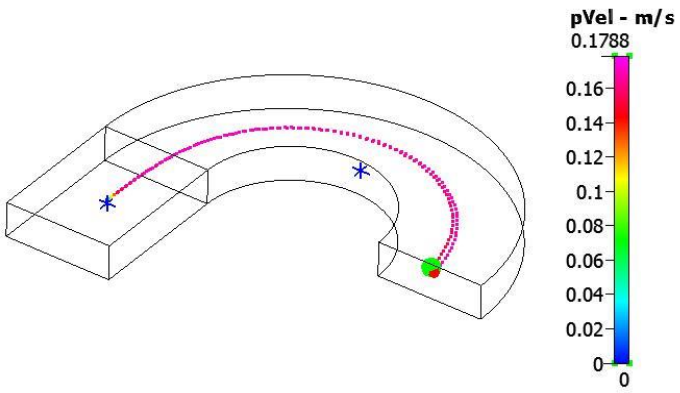

(a) 5 µm above

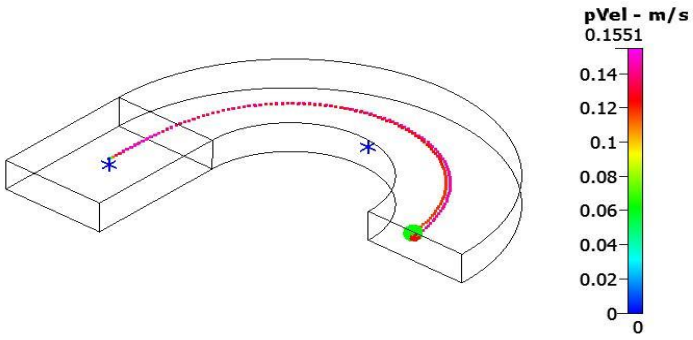

(b) 10 µm above

Fig. 4-33 Trajectories of D10 and D20

From the side view shown in Fig. 4-34, both of the particles move upward to find their equilibrium position, driven by the lift force. This trend lasts until the particles leave this channel.

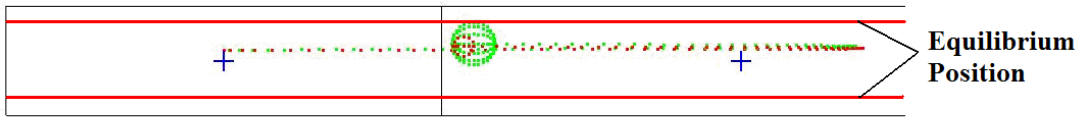

(a) 5 µm above

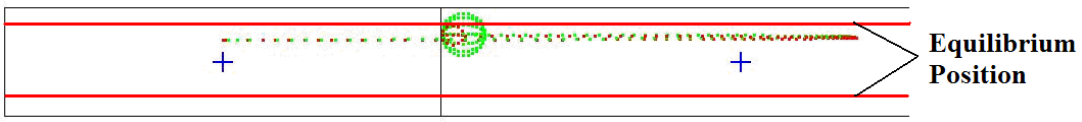

(b) 10 µm above

Fig. 4-34 Trajectories of particles with releasing point 5 µm above the mid-plane

The horizontal coordinates Y of the particles have been recorded, shown in Fig. 4-35 (a) and (b). They show slight deviation of the two particles' trajectories, where the larger 20 μm particle D20 tends to move inside under a critical velocity, which agrees with the experimental observations. The distance between the two curves originating from the same point develops and increases, which highlights the origin of the mechanism for size-based particle lateral separation, that we shall discuss in detail in the next chapter. This displacement will increase with the length of channel.

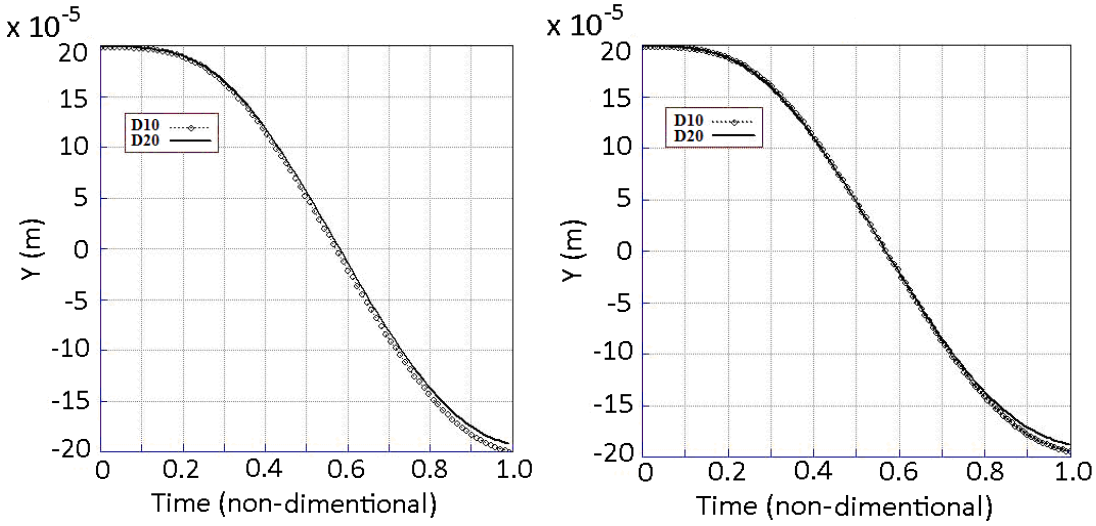

(a) 5 μm above (b) 10 μm above

Fig. 4-35 Coordinates Y of the particles D10 and D20

Fig. 4-36 clearly shows the particles are moving upwards driven by lift force. More convincingly, the D20 are moving faster vertically, which is consistent with the notion that larger particles will be experiencing larger lift forces (proportional to r^4). It is also noticed that the vertical migration velocity is approaching a constant, which indicates this lateral terminal velocity is the outcome of the balance of lift force and vertical drag force, i.e. $F_L = F_{D\perp} = 6\pi\mu r v_\perp$, where $v_\perp$ is the particle vertical migration velocity. Because this velocity is much smaller than the mainstream velocity, the

Stokes law can be applied. This provides a method to measure the lift force exerted on a particle. The terminal settling velocity of D10 released from A is $v_{\perp A10} = 0.37\times10^{-3}$ m/s. Similarly, $v_{\perp A20} = 0.67\times10^{-3}$ m/s, $v_{\perp B10} = 0.46\times10^{-3}$ m/s, $v_{\perp B20} = 0.48\times10^{-3}$ m/s. Particles released from A end up with bigger vertical offset distance, because D20, when released from B, is influenced by the wall-induced lift and decelerated, which is demonstrated in Fig. 4-36 (b), where the line representing its vertical movement is actually a curve gradually approaching to the equilibrium position.

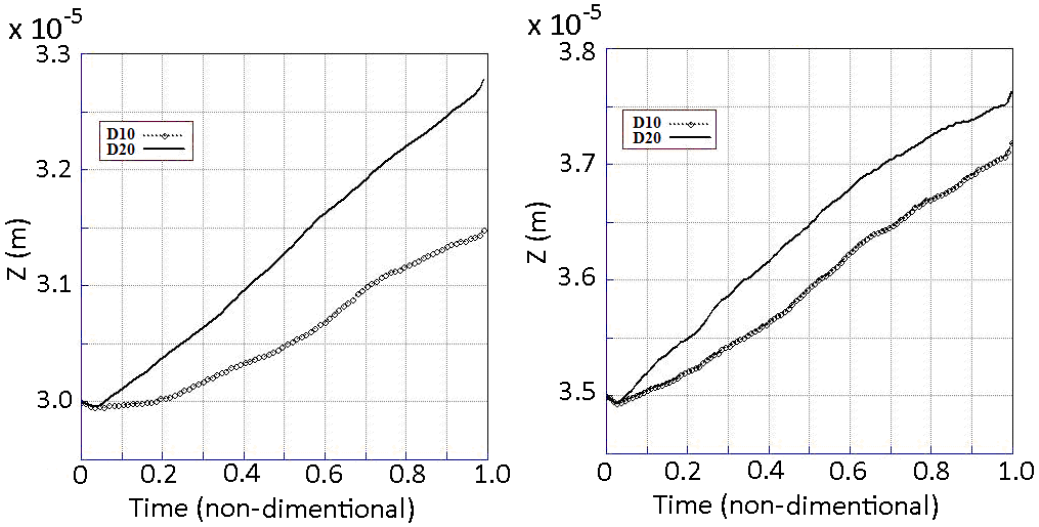

(a) 5 µm above (b) 10 µm above

Fig. 4-36 Z Coordinates of the particles D10 and D20

5. Fluidic particle manipulation

In this chapter, particle manipulation based on microfluidic channels has been investigated, adopting our developed simulation platform. First, hydrodynamic focusing is achieved in straight channels with buffer flows. Second, under a wide range of flow velocities, curved channels, including 180^o bends and spiral geometries have been designed and tested. Third, to enhance particle focusing and separation efficiency, novel designs of multi-inlet curved channels are introduced and tested.

5.1 Hydrodynamic focusing

Hydrodynamic focusing [149] describes in general a technique where multiple inlet branches (central plus two side branches in 2D or 2D-like flows, core-and-annular-sheath inlets in 3D flow, or variants of these) guide or force the middle sample flow to predefined regions of the channel, usually within a narrow streak. Hydrodynamic focusing is a useful tool for manipulation of samples, as a pretreatment for flow cytometry and Coulter counter detection. Two streams of flows are introduced to two side inlet branches, which is termed as *buffer flow* or *sheath flow*. Sample fluids, containing particles, can be focused so that inside the channel, they only occupy and propagate along the middle section – with the option to make that passage so narrow as to lead to an alignment of the carried particles – then only a single particle passes at a time. This technique is beneficial for biochemical mixing (fast mixing) and cell analysis (flow cytometry). Velocities can differ substantially between the buffer flow and sample flow – many of the test cases we have examined involved $v_{inlet-buffer} = 0.5$ m/s; $v_{inlet-sample} = 0.1$ m/s. In our tests, we start by releasing particles from 3 initial positions with adjacent distances of 55 μm.

Trajectories can be simulated either with all particles present (see previous chapter, where multiple settling particles interacted with each other) to test both particle-flow and particle-particle interactions, or independently to avoid mutual particle influence. We focus here in the latter case. The channel schematic is shown in Fig. 5-1.

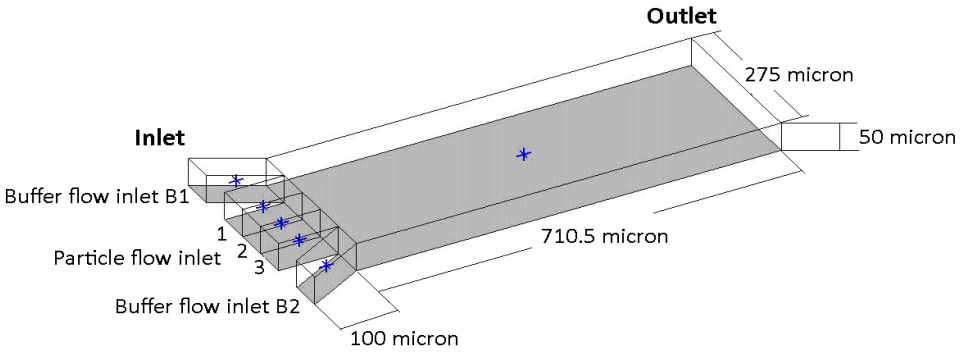

Fig. 5-1 Schematic of hydrodynamic focusing straight channel

Fig. 5-2 demonstrates the hydrodynamic focusing effect on different-sized particles. After focusing, the average distance between the 10 μm particles at outlet exiting the channel $\overline{s}_{10}$=22.19 μm; while for 20 μm particles $\overline{s}_{20}$=19.66μm; further for 40 μm particles $\overline{s}_{40}$=18.31 μm. Thus for larger particles, hydrodynamic focusing effect is revealed to be marginally more effective. The equally spaced trace lines at inlet are also calculated which demonstrates the middle sample flow is squeezed into a much thinner layer. The flow velocity within this sample flow exhibits an inverted triangle velocity distribution, shown in Fig. 5-2 (a). This is expected, as the shear-driven Couette-type contribution of the rapidly moving sheath flow dominates the core flow.

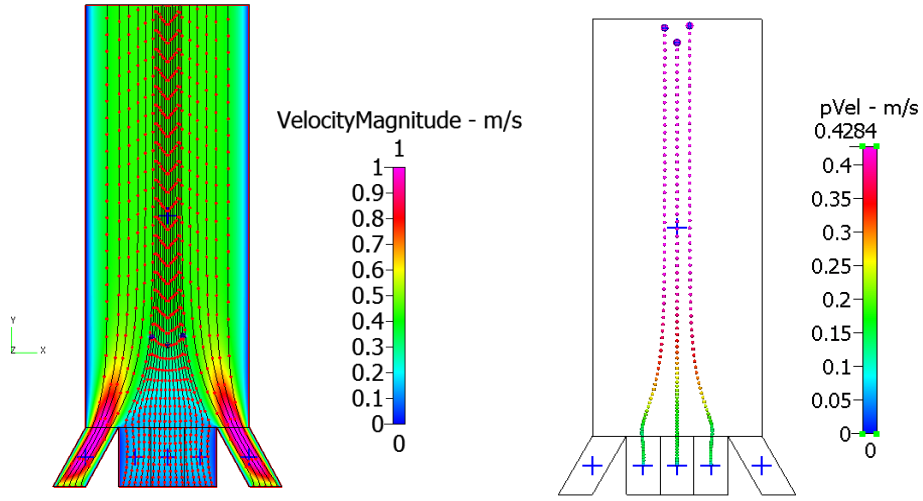

(a) 10 µm particles

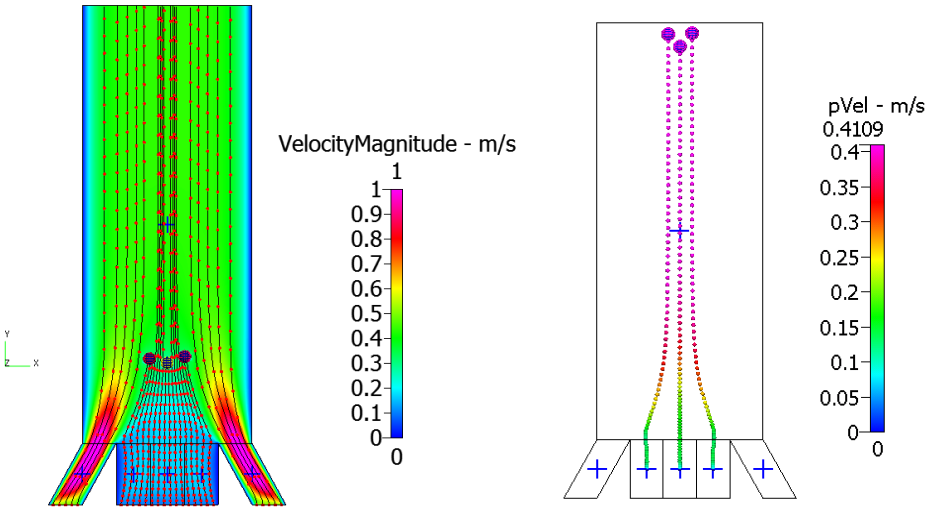

(b) 20 µm particles

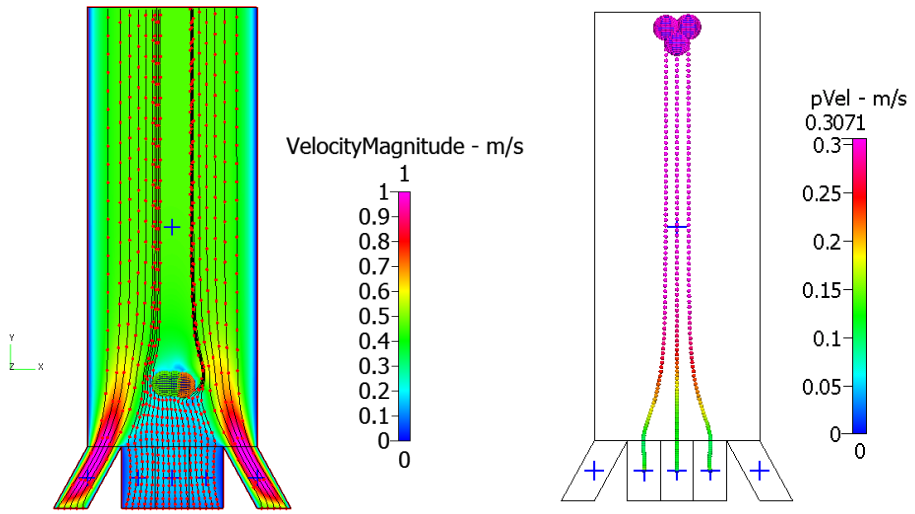

(c) 40 µm particles

Fig. 5-2 Hydrodynamic focusing in straight channel

5.2 Curved channel for size-based particle separation

A 3D low aspect ratio 180° curved channel is adopted, with width 150 μm, height 50 μm and curvature radius 200 μm. A straight section is added, connecting to its inlet to make the channel flow at the bend fully developed.

5.2.1 Curved channel

Particles of 3 different sizes (10 μm, 20 μm and 40 μm) are released at the same starting point. Cases with a wide range of inlet velocity have been studied. Some indicative results are shown in Fig. 5-3.

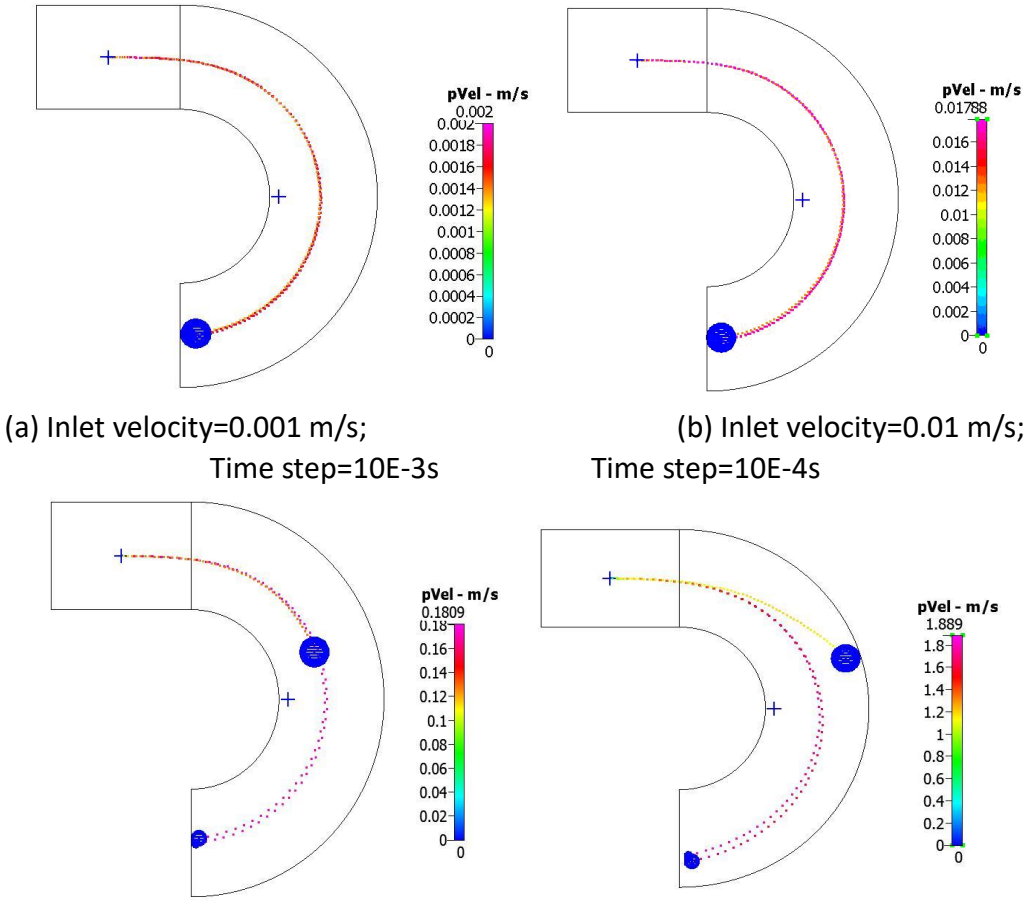

(a) Inlet velocity=0.001 m/s; Time step=10E-3s

(b) Inlet velocity=0.01 m/s; Time step=10E-4s

(c) Inlet velocity=0.1 m/s; Time step=10E-5s

(d) Inlet velocity=1 m/s; Time step=10E-6s

Fig. 5-3 Particles of different sizes under various inlet velocities

With high flow velocity, the larger particles tend to move to the outer wall of the channel while the smaller one tends to move to the inner wall. With flow velocity decreasing, the trajectories of different-sized particles converge to one lateral position across the channel. This resonates with the fact that smaller Stokes number $S_{tk} = \frac{\tau U_0}{d_c}$ indicates better tracing accuracy, where $\tau = \frac{\rho_P d_P^{\ 2}}{18\mu}$ is particle relaxation time. Thus the smaller particles have smaller Stokes number, moving closer to the streamlines of flow, while the bigger particles can evidently deviate from the streamlines.

This also sheds light on the separation principle: for particles whose sizes are fixed, the Stokes number difference of at least one particle group must be over a threshold for separation. There are two approaches to achieve this: one is to increase the flow velocity while the other is to decrease the dimension of the channel. Thus only by microfluidics microparticle separation can be achieved with high specificity under normal velocity conditions.

It is important to explain and discuss now the mechanisms through which particle separation under different flow inlet velocities actually takes place:

1. Dean-lift separation at low flow velocity

In the first case, 3 groups of particles respectively with diameter of 10, 20 and 40 μm have been tested. They are released at the centre of the channel straight section. The inlet velocity is set to be 0.001 m/s. The external time step for the micro particle trajectory integration (and consequently for the flow equations integration) is 0.001s,

a value that satisfies the CFL condition $\frac{u\Delta t}{\Delta x} \le 1$. Combined with our Frozen Flow and Flow Correction Coefficient approach, time independence of simulation is confirmed. The internal time-step is set at $\Delta t_{\text{Sub}}=10^{-8}$s. Fig. 5-4 shows flow field velocity and pressure contours at the same time step (100th time step, equivalent to 0.1s), as well as the positions of three particles in the channel. As $F_{\text{D}} = \frac{1}{2}\rho v^2 C_d A = \frac{\pi}{2}\rho v^2 C_d r^2$, the particle acceleration $a = \frac{F_{\text{D}}}{m} \propto \frac{1}{r}$, which explains why the smaller particle migrates faster than the bigger ones. The peak of velocity magnitude appears near the inner wall in this channel. The pressure has an axial gradient, while the radial pressure gradient is small.

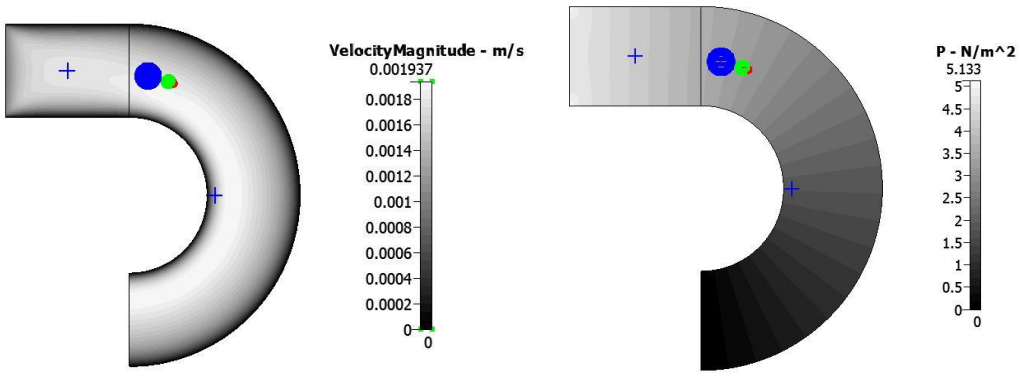

Fig. 5-4 Velocity, pressure contour at the mid-plane and the particle positions at 0.1s

Fig. 5-5 shows the positions of all the three particles when they pass through the 60° (from upstream to downstream) cross section. Only the 40 μm particle is drifting towards the upper wall. This is because the lift force grows proportionally to r^4, according to Asmolov's analysis [82]. When the particle dimension is comparable to the channel, the lift force can play a key role in determining the particle trajectory. Cutoff diameter is defined as $d_{\text{Cutoff}} / L = 0.07$, where L is the characteristic length

[84]. Taking particle migration distance into account, we adopt half of the channel length, 414 μm, thus the cutoff diameter for lift force would be $d_{\text{Cutoff}} = 0.07L = 29.0$ μm. Thus both the 10 μm and 20 μm particles can't be forced by the lift and thus stay close to the mid-plane. This conclusion is valid through the whole process, which is shown in the side view, Fig. 5-6. To make it clear, through this research unless otherwise noted, different sized particles and their trajectories are denoted by distinct colors, red for 10 μm, green for 20 μm and blue for 40 μm particle.

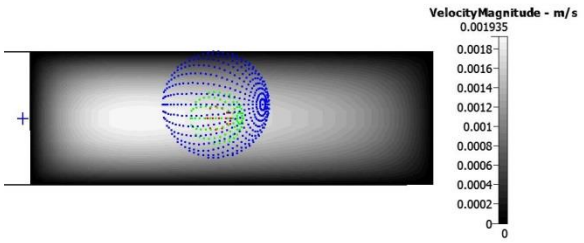

Fig. 5-5 Velocity contour and particles at the 60^{o} cross section

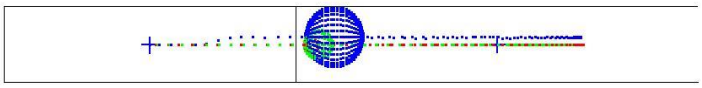

Fig. 5-6 Side view of particle trajectories and vertical positions

Fig. 5-7 shows the particle trajectories at the time when the 20 μm particle goes through the 90^{o} cross section and the flow field on the 90^{o} cross section. They closely follow the streamline which originates from the releasing point. The axial distance between the 40 μm particle and the smaller ones increases over time. This reveals the mechanism of size-based particle streamwise separation by migration speed difference. The flow field demonstrates typical Dean vortices and indicates the larger particles will expose a larger area to the effects of the upper and lower backward flows.

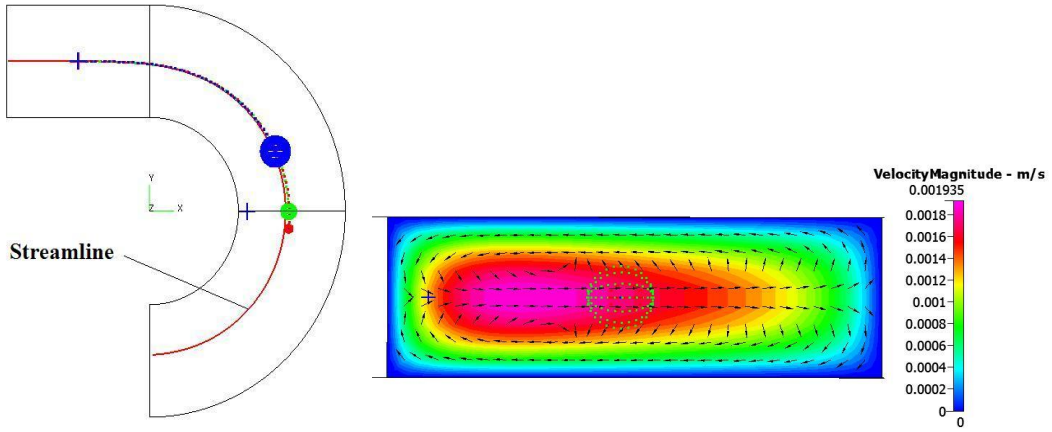

Fig. 5-7 Particle trajectories and flow field on the middle cross section

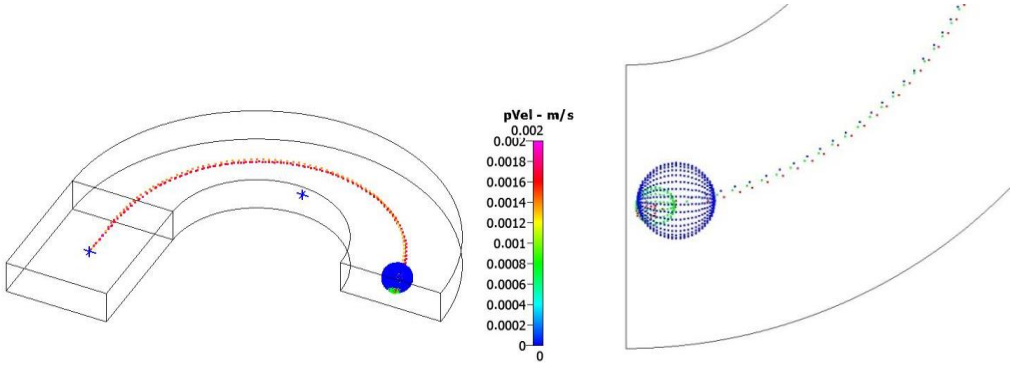

Fig. 5-8 Whole particle trajectories for v_{inlet}=0.001 m/s

In summary, for smaller particles (size is below the cutoff value $d / D_h \leq 0.07$), with the lift force decreasing dramatically, drag force becomes dominant leading them to be carried by Dean vortices to fill the whole channel, which is demonstrated in Fig. 5-9 (a). Above the cutoff diameter, the large particles are transported towards equilibrium positions by the lift force, as shown in Fig. 5-9 (b). Further, if two particles are both above the cutoff size, in comparison to the smaller particle, the larger particle is more likely to be forced by the backward flow near the upper or lower walls (from the outer to the inner wall) because it exposes more surface area to the backward flow. Also, the larger particle moves vertically more quickly due to the lift force. So the larger particle will be located at an inner position while the smaller

particle is located more towards the outer position. Because the geometry is symmetric with respect to the mid-plane, the particles can similarly move downwards to the lower half. The lift force is proportional to r^4 while the Dean-direction drag is $F_D \propto \rho U_m{}^2 d_p D_h{}^2 R^{-1} \propto r$ [144]. Thus larger particles are more reluctant to be moved by the secondary flow, while smaller particles are more inclined to move with the Dean vortices to the outer wall. If the channel has enough curvature length eventually the smaller particle would circle in a loop and move inwards near the upper or lower walls. So the particles above certain dimension tend to focus to a lateral equilibrium positions near the inner wall, which provides a mechanism for size-based particle separation.

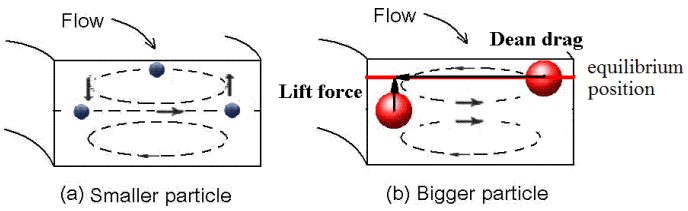

Fig. 5-9 Size-based particle lateral migration

The above analysis didn't bring particle centrifugal force and radial pressure gradient effects into account because the flow velocity is low. Pressure difference between the inner and outer walls not only forces the flow to turn with the curved channel to drag the particle, but also imposes a radial pressure gradient across the channel to influence the particle. When the flow velocity increases, centrifugal force caused by the particle inertia $F_C = \frac{m v_\theta^2}{R} = \frac{4}{3}\pi\rho r^3 \frac{v_\theta^2}{R}$ can be much larger than the radial pressure gradient force $F_P = -\frac{\pi}{6} d_P{}^3 \nabla P$, namely $F_C \gg F_P$, resulting in inertia

dominating the particle motion. Thus the particles with circumferential speed $v_\theta >$ $\frac{1}{8}\sqrt{-\frac{R}{\rho}\nabla P}$ would move towards the outer wall.

2. Radial pressure gradient separation at high flow velocity

In the second case, the inlet velocity is increased to 1 m/s (since this value demonstrates the effect well). The time step was 10^{-6}s. Fig. 5-10 shows flow velocity field and pressure contour at the same time step (100th time step, equivalent to 10^{-4}s), as well as the positions of three particles in the channel. The pressure distribution develops to such a pattern that on the same axial cross section, the pressure near the outer wall is higher than the pressure near the inner wall, suggesting the pressure gradient is not purely axial when the flow velocity increases. This radial pressure gradient is triggered by the increase of Dean number.

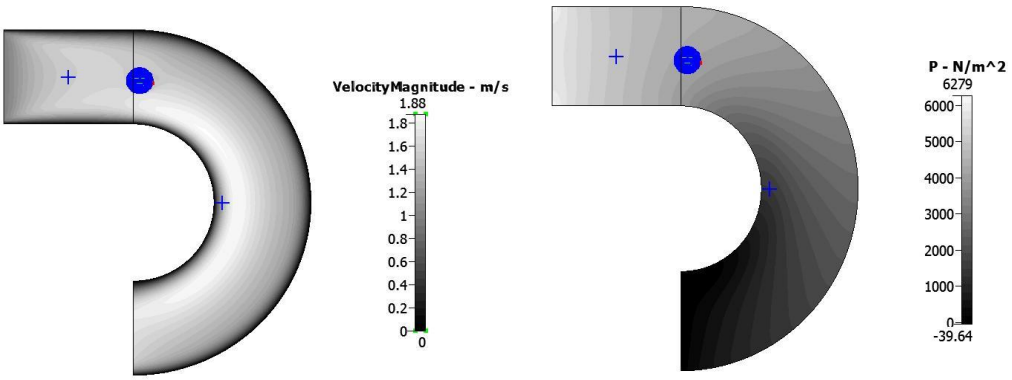

Fig. 5-10 Velocity and pressure contours at the mid-plane and particle positions at 0.001s

Fig. 5-11 shows the positions of all the three particles when they pass through the 60^o (from upstream to downstream) cross section. Only the 40 μm particle is substantially affected by the lift force obviously, for the same reason as the last case. But in this case it migrates to the lower wall, indicating the problem is symmetric

about the middle horizontal cross section.

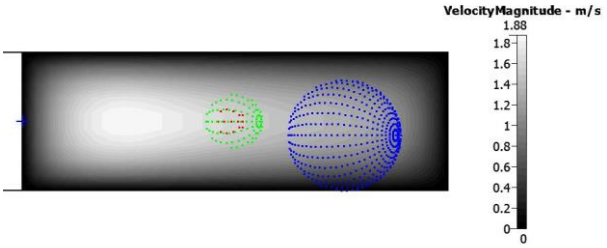

Fig. 5-11 Velocity contour and particles at the 60° cross section

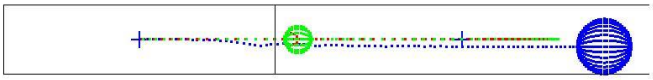

Fig. 5-12 Side view of particle trajectories and vertical positions

Fig. 5-13 shows the particle positions at the time when the 20 μm particle goes through 90° cross section and the flow field on the 90° cross section. The particle axial sequence is the same, but the larger particles present the trend to go to the outer wall, away from the streamline. The drag force $F_D = \frac{1}{2}\rho v^2 C_d \pi r^2$. With the same circumferential speed v_θ and centrifugal force $F_C = \frac{4}{3}\pi\rho r^3 \frac{v_\theta^2}{R}$, if the particle size is over a limit to satisfy $F_C > F_D$, i.e. $r > \frac{3}{8} C_d (\frac{v}{v_\theta})^2 R$, this particle will obviously deviate from the streamline and go to the outer position. Because the flow drag is streamwise in a curved pattern, which is caused by radial pressure gradient induced by confinement of the walls, this separation scheme is termed as radial pressure gradient separation.

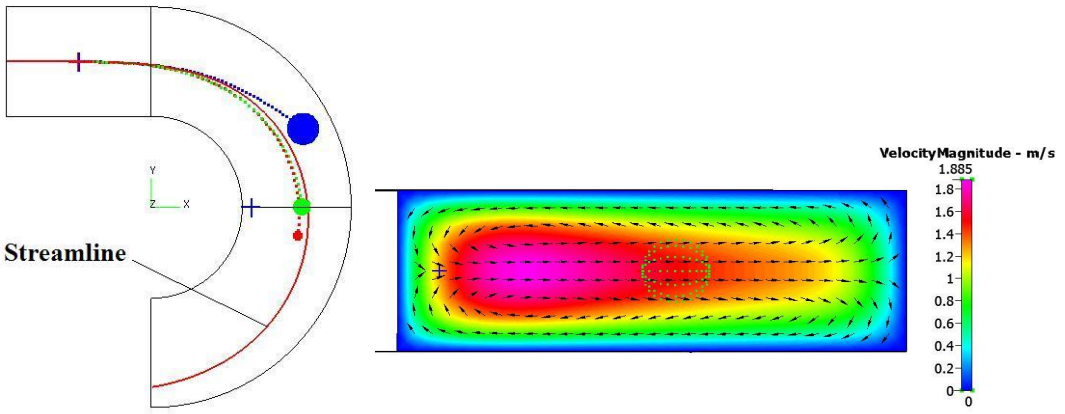

Fig. 5-13 Particle positions and flow field on the middle cross section

Fig. 5-14 shows the entire particle trajectories. Clearly the largest 40 μm particle deviates from the streamline and migrates outward. From another perspective of view, larger particles induce higher Stokes number $S_{tk} = \frac{\tau_S U_0}{L}$, where τ_S is the particle relaxation time, U_0 is the fluid velocity, L is the characteristic length (in this case it should be the channel hydraulic diameter $D_h = 75$ μm). Stokes numbers represent tracing accuracy of particles on the flow. Only for $S_{tk} \ll 1$, can particles follow fluid streamlines closely. Taking the inlet velocity 1m/s, for the 40 μm particle, $S_{tk} = \frac{\tau_S U_0}{L}$ =1.19. This also explains why at high velocities particles with dimension comparable to the channel diverge substantially from the streamline.

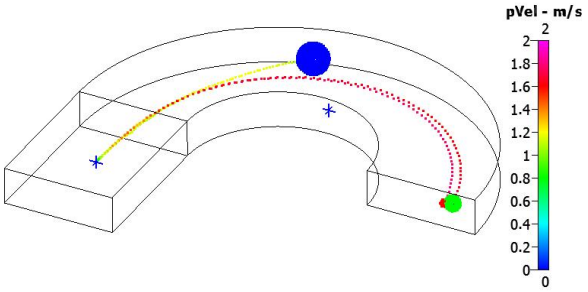

Fig. 5-14 Whole particle trajectories for v_{inlet}=1 m/s

To verify the above findings and to eliminate the inlet/outlet effects, another 3D channel (adopted in chapter 4.1) with extended inlet and outlet branches has been investigated. In the same wide range of velocities (0.001 – 1 m/s), particles of different sizes (10 μm, 20 μm and 40 μm) are released at the same origin, 200 μm away from the inlet. Firstly the results prove that within the normal velocity range for microfluidic channels, particle rotation effect is secondary comparing to translational movement on trajectories. The comparison between the simulation results of the cases with and without rotation is shown in Fig. 4-19. The results also agree with the two separation mechanisms stated previously - Dean-lift separation at low flow velocity and radial pressure gradient separation at high flow velocity. When in the Dean-lift separation scheme (see Fig. 5-15 (a)), with increasing of particle size, larger particles tend to move inward laterally. When in radial pressure gradient separation scheme (see Fig. 5-15 (b) and (d)), with increasing of particle size, larger particles move outward laterally. The resolution of the radial pressure gradient separation scheme can be adjusted to be significantly larger than the Dean-lift separation. Although the trajectory difference seems not substantial for Dean-lift separation, when the channel path is elongated, this resolution could be effectively enhanced.

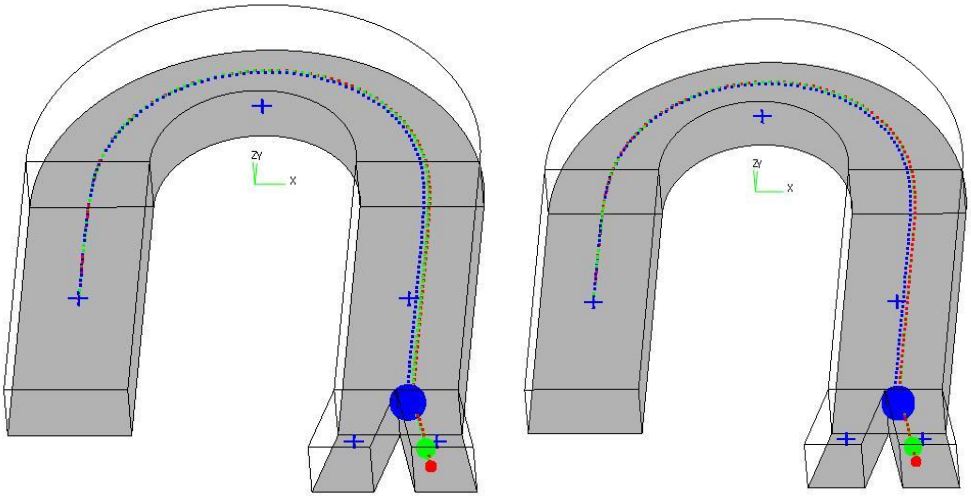

(a) v_{inlet}=0.001 m/s, time step=10E-3s

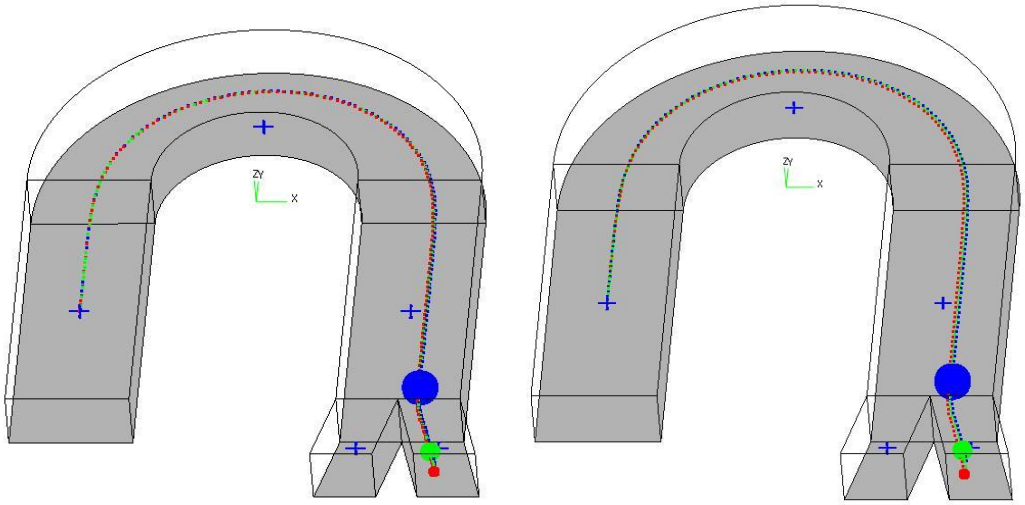

(b) v_{inlet}=0.01 m/s, time step=10E-4s

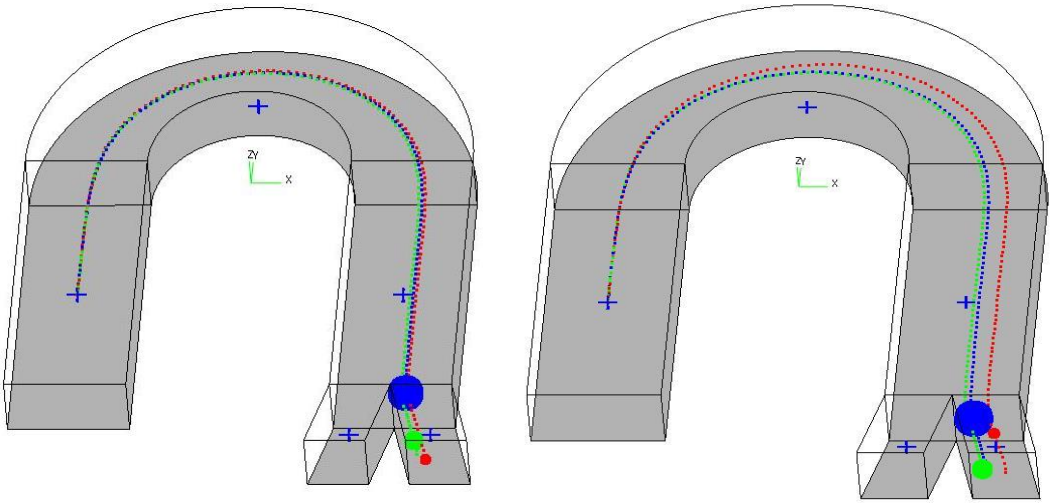

(c) v_{inlet}=0.1 m/s, time step=10E-5s

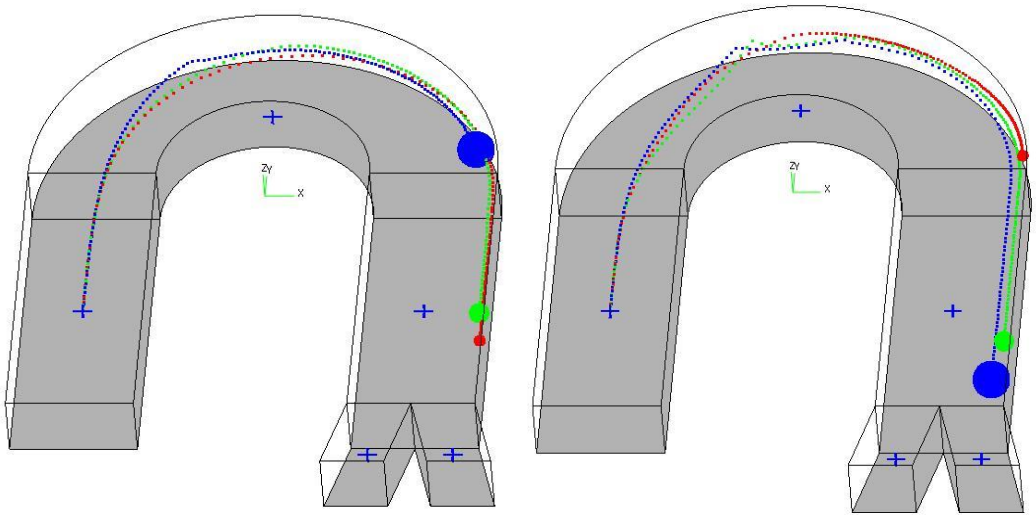

(d) v_{inlet}=1 m/s, time step=10E-6s

Fig. 5-15 Particle trajectories of different sizes under various inlet velocity: left - with particle rotation; right – without particle rotation

It is further found that with increasing size, the influence of particle presence on the flow field is more substantial, as expected, sometimes changing the flow patterns profoundly, as shown in Fig. 5-16. Actually, in Fig. 5-16 (a), the smallest particle (10 μm in diameter) does not change the flow field in a discernible manner. However, in Fig. 5-16 (c), the largest particle with 40 μm diameter alters the flow field by cutting off the peak velocity area. Another finding is that with the increase of flow velocity, the same particle tends to influence the flow field more dramatically, which can be seen in Fig. 5-16 (a) and (b). All these results are presented for the same 300th time step. These also prove, again, that when particle dimensions are comparable to that of the microfluidic channel, our direct simulation approach is competent, while the point-particle approximation would evidently be inappropriate.

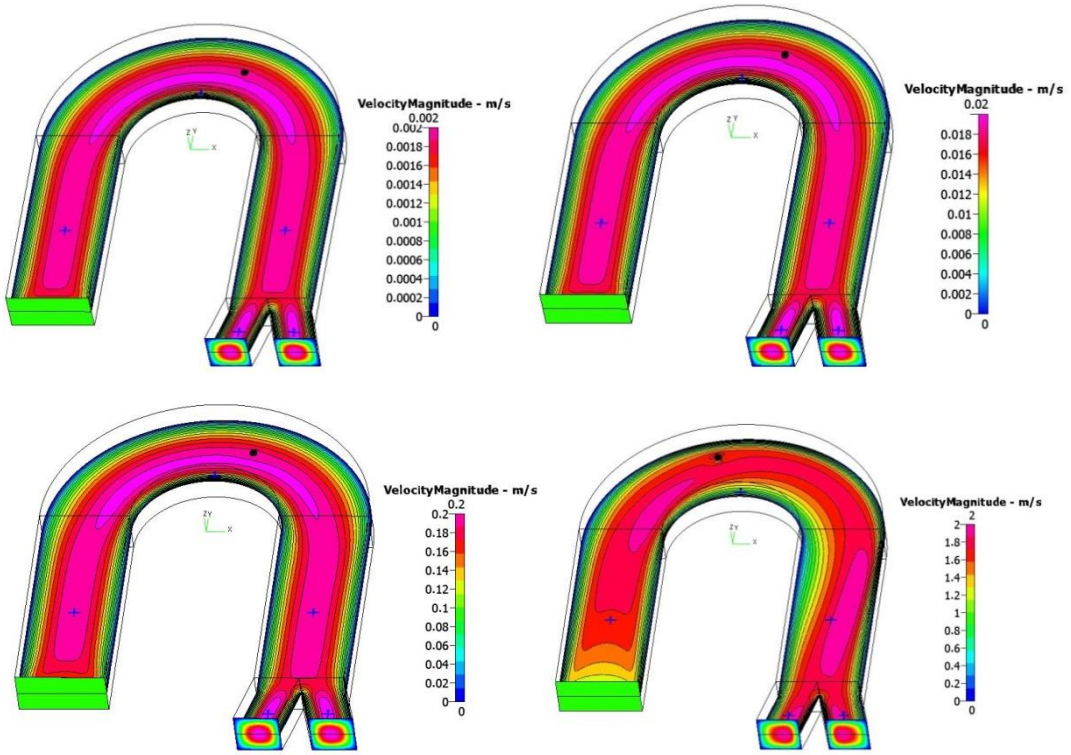

(a) 10 µm particle

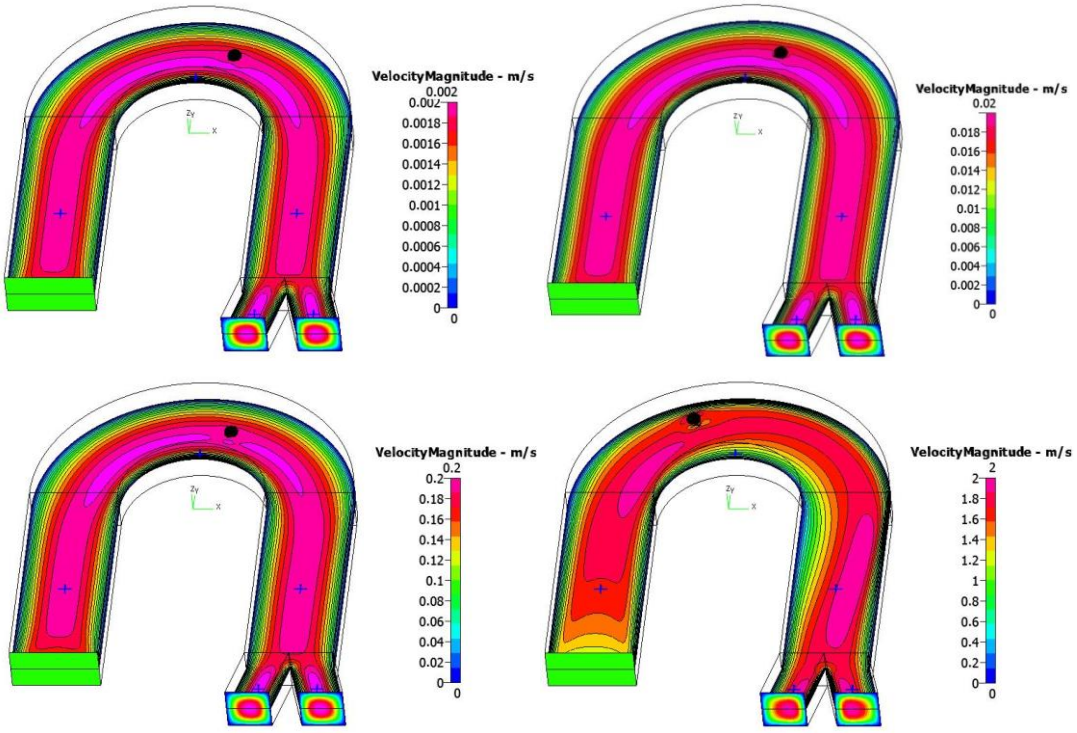

(b) 20 µm particle

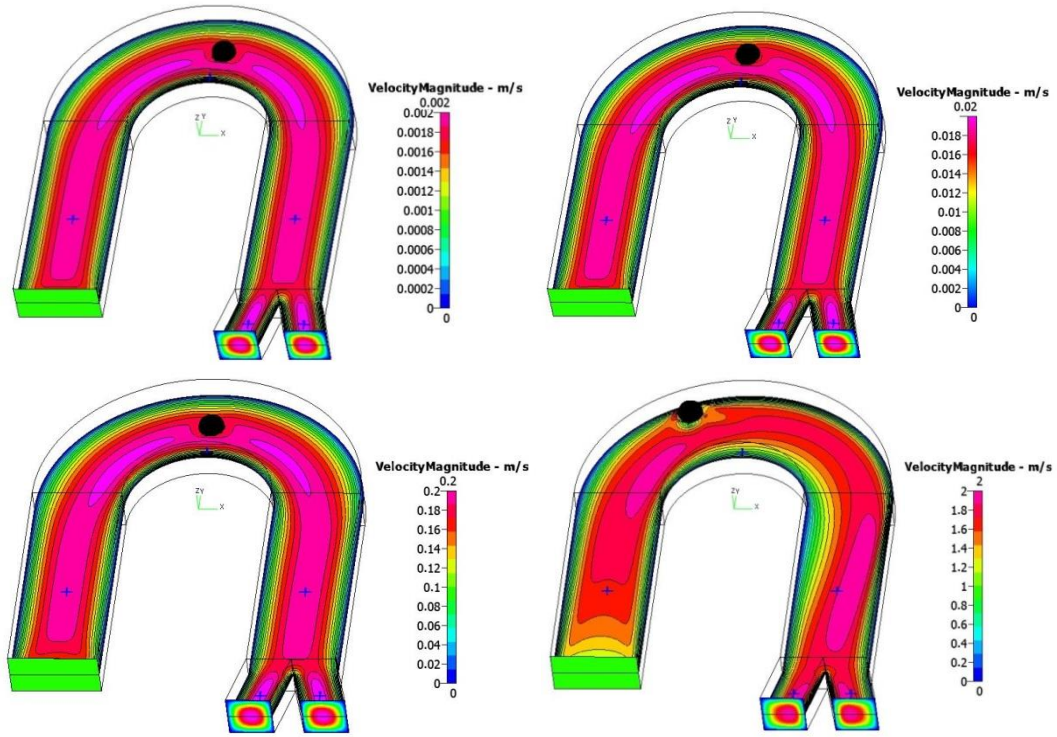

(c) 40 μm particle

Fig. 5-16 Particle-flow coupling for different particle sizes and flow velocities

5.2.2 Spiral channel

As a preliminary excursion into more complex geometries, with more intense curvature features, a 2D spiral channel has been designed and tested. Inlet velocity is set to be 0.2 m/s. 10 μm and 7 μm particles are adopted. Geometry design and simulation results of particle trajectories are shown in Fig. 5-17, which is consistent with the experimental findings that in a long spiral channel, the larger 10 μm particle will focus to an inner lateral position while smaller 7 μm particles move to outer position, shown in Fig. 5-18 [69], where lateral displacement refers to the radial distance between the particle streams. The flow field and pressure contour are shown in Fig. 5-19.

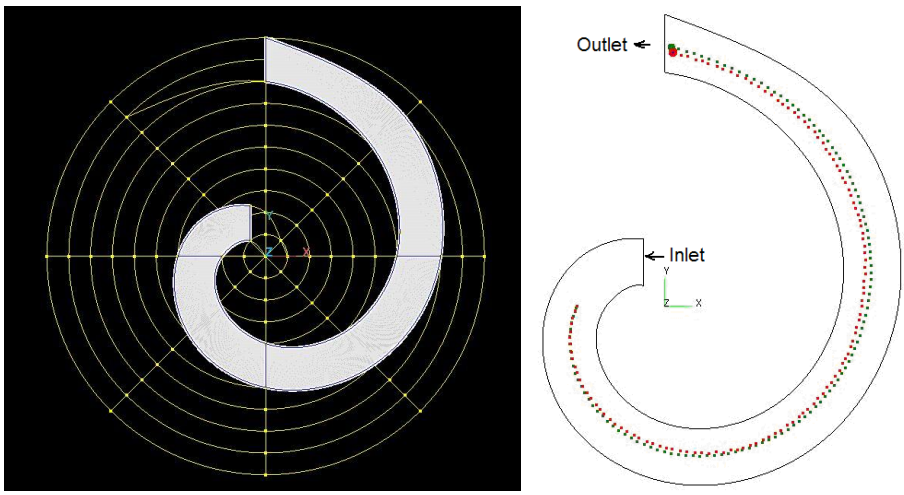

Fig. 5-17 7 µm (green) and 10 µm (red) particles in 2D spiral channel

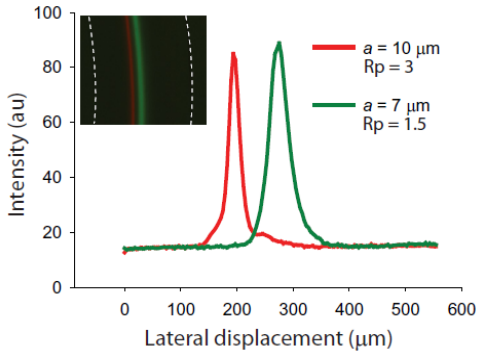

Fig. 5-18 Lateral displacement of different-sized particles [69]

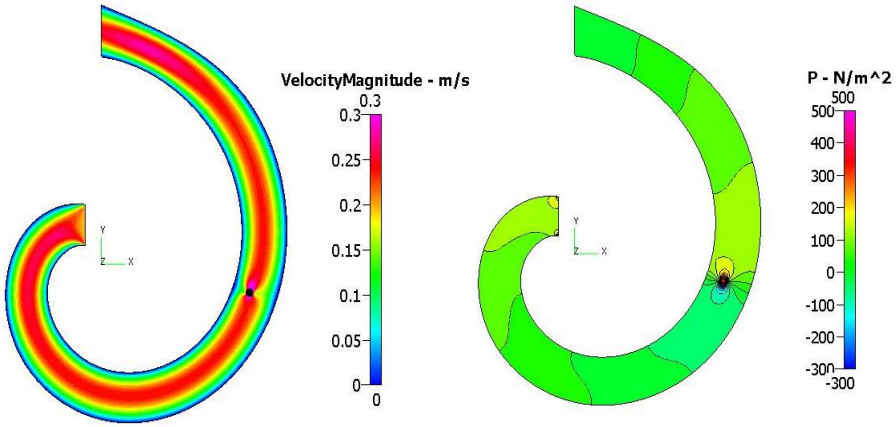

Fig. 5-19 Flow field and pressure contour of 2D spiral channel

The natural extension to a 3D spiral channel is then pursued. With the same planar configuration, the channel height is given as 20 µm to demonstrate 3D effects. This time the inlet velocity is raised to 2 m/s, which is comparable to the experiment

parameter [69]. Fig. 5-20 shows the results of trajectory separation by particle size in the 3D spiral channel within a wide range of velocities. The velocity and total pressure contours are also computed. We demonstrate that in spiral channels, both at low velocity (0.02 m/s) and high velocity (2 m/s), 7 μm and 10 μm particles can be separated and the larger particle moves towards the inner lateral position, shown in Fig. 5-20 (a) and (c). Clearly in these two cases the Dean-lift particle separation mechanism is dominant, and the flow velocity threshold transition from Dean-lift separation to radial pressure gradient separation is much higher than that in the previous 180^{o} curved channel. This demonstrates that spiral channels, with elongated axial length, can further increase the impact of the Dean-lift effect over the influence of the inertia effect because wall effect increases with migration length.

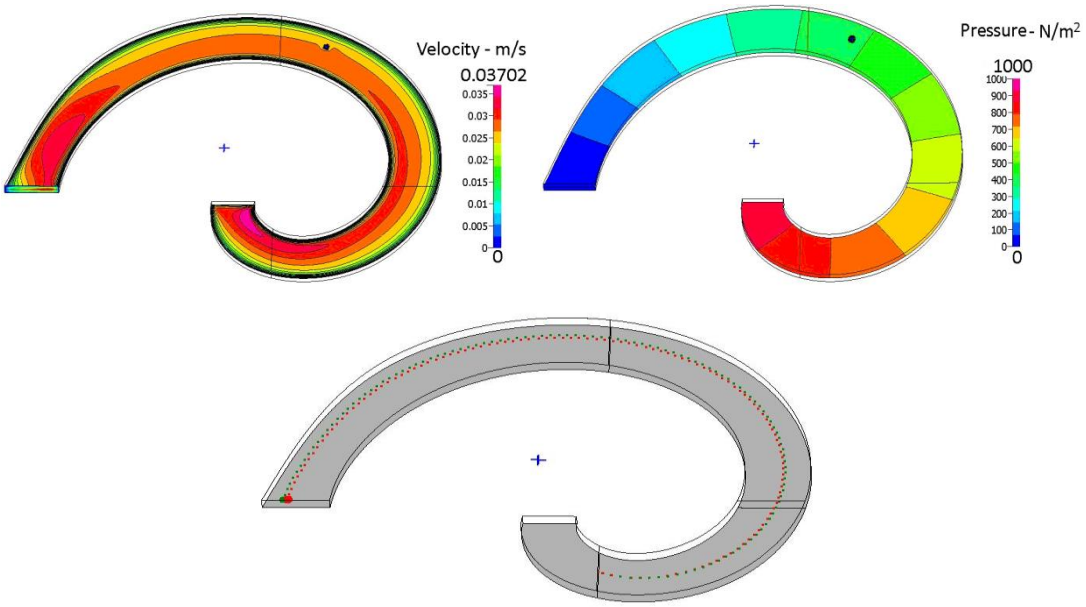

(a) v_{inlet}=0.02 m/s, time step=10E-4s

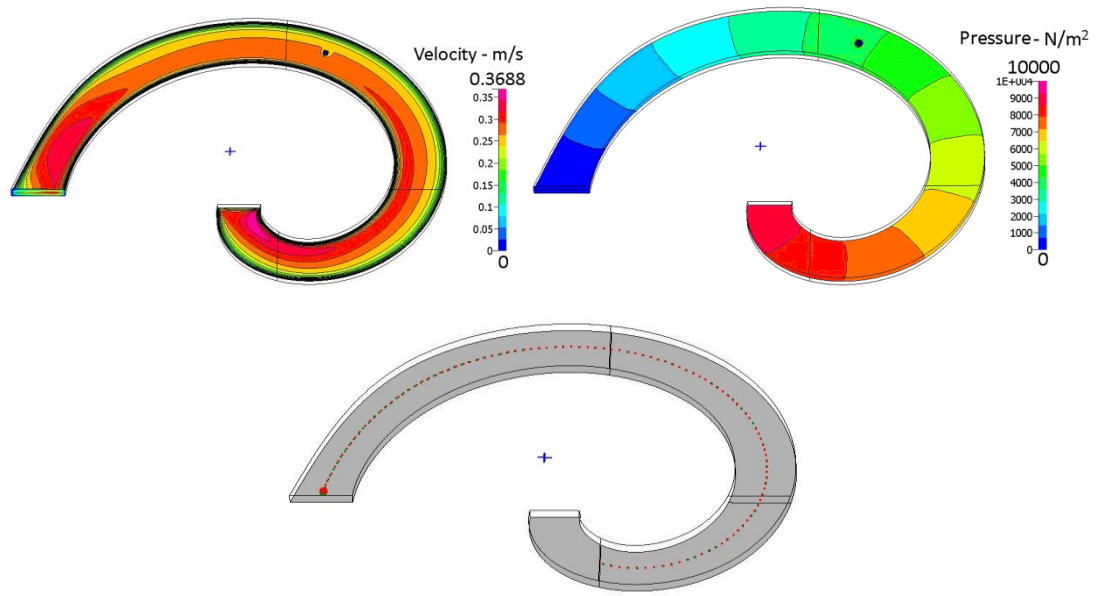

(b) v_{inlet}=0.2 m/s, time step=10E-5s

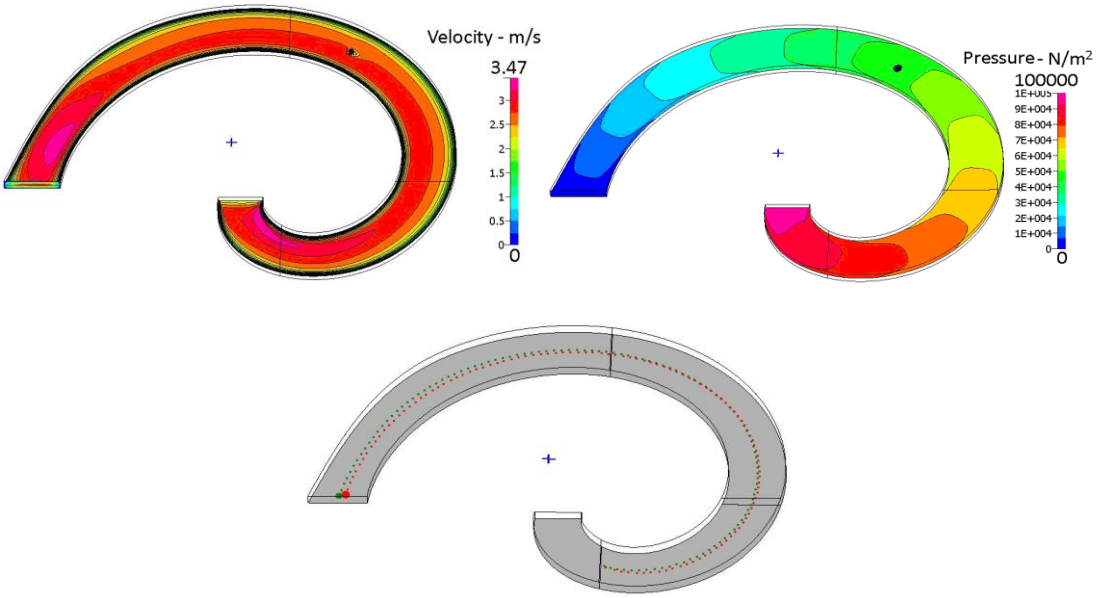

(c) v_{inlet}=2 m/s, time step=10E-6s

Fig. 5-20 7 µm (green) and 10 µm (red) particles in the 3D spiral channel

References

[1] W. R. Dean and J. M. Hurst, "Note on the motion of fluid in a curved pipe," *Mathematika,* vol. 6, pp. 77-85, 1959.

[2] H. A. Stone and S. Kim, "Microfluidics: Basic issues, applications, and challenges," *AIChE Journal,* vol. 47, pp. 1250-1254, 2001.

[3] S. A. Morsi and A. J. Alexander, "An investigation of particle trajectories in two-phase flow systems," *Journal of Fluid Mechanics,* vol. 55, pp. 193-208, 1972.

[4] D. A. Drew, "Mathematical Modeling of Two-Phase Flow," *Annual Review of Fluid Mechanics,* vol. 15, pp. 261-291, 1983.

[5] Q. A. Pankhurst, J. Connolly, S. K. Jones, and J. Dobson, "Applications of magnetic nanoparticles in biomedicine," *J. Phys. D: Appl. Phys,* 2003.

[6] G. M. Whitesides, "The origins and the future of microfluidics," *Nature,* vol. 442, pp. 368-373, 2006.

[7] P. Yager, T. Edwards, E. Fu, K. Helton, K. Nelson, M. R. Tam, and B. H. Weigl, "Microfluidic diagnostic technologies for global public health," *Nature,* vol. 442, pp. 412-418, 2006.

[8] J. M. Freyssinet, "Cellular microparticles: what are they bad or good for?," *Journal of Thrombosis and Haemostasis,* vol. 1, pp. 1655-1662, 2003.

[9] P. Wolf, "The Nature and Significance of Platelet Products in Human Plasma," *British Journal of Haematology,* vol. 13, pp. 269-288, 1967.

[10] J. George, L. Thoi, L. McManus, and T. Reimann, "Isolation of human platelet membrane microparticles from plasma and serum," *Blood,* vol. 60, pp. 834-840, October 1, 1982.

[11] J. Simak and M. P. Gelderman, "Cell Membrane Microparticles in Blood and Blood Products: Potentially Pathogenic Agents and Diagnostic Markers," *Transfusion Medicine Reviews,* vol. 20, pp. 1-26, 2006.

[12] C. Thery, L. Zitvogel, and S. Amigorena, "Exosomes: composition, biogenesis and function," *Nat Rev Immunol,* vol. 2, pp. 569-579, 2002.

[13] H. F. G. Heijnen, A. E. Schiel, R. Fijnheer, H. J. Geuze, and J. J. Sixma, "Activated Platelets Release Two Types of Membrane Vesicles: Microvesicles by Surface Shedding and Exosomes Derived From Exocytosis of Multivesicular Bodies and alpha -Granules," *Blood,* vol. 94, pp. 3791-3799, December 1, 1999.

[14] E. Pap, É. Pállinger, M. Pásztói, and A. Falus, "Highlights of a new type of intercellular communication: microvesicle-based information transfer," *Inflammation Research,* vol. 58, pp. 1-8, 2009.

[15] A. M. Weerheim, A. M. Kolb, A. Sturk, and R. Nieuwland, "Phospholipid Composition of Cell-Derived Microparticles Determined by One-Dimensional High-Performance Thin-Layer Chromatography," *Analytical Biochemistry,* vol. 302, pp. 191-198, 2002.

[16] J. H. W. Distler, D. S. Pisetsky, L. C. Huber, J. R. Kalden, S. Gay, and O. Distler, "Microparticles as regulators of inflammation: Novel players of cellular crosstalk in the rheumatic diseases," *Arthritis & Rheumatism,* vol. 52, pp. 3337-3348, 2005.

[17] R. Altman, A. Scazziota, M. Herrera, and C. Gonzalez, "Thrombin generation by activated factor VII on platelet activated by different agonists. Extending the cell-based model of hemostasis," *Thrombosis Journal,* vol. 4, p. 5, 2006.

[18] S. Nomura, Y. Ozaki, and Y. Ikeda, "Function and role of microparticles in various clinical settings," *Thrombosis Research,* vol. 123, pp. 8-23, 2008.

[19] R. Nieuwland, R. J. Berckmans, R. C. Rotteveel-Eijkman, K. N. Maquelin, K. J. Roozendaal, P. G. M. Jansen, K. t. Have, L. Eijsman, C. E. Hack, and A. Sturk, "Cell-Derived Microparticles Generated in Patients During Cardiopulmonary Bypass Are Highly Procoagulant," *Circulation,* vol. 96, pp. 3534-3541, November 18, 1997.

[20] É. Biró, K. N. Sturk-Maquelin, G. M. T. Vogel, D. G. Meuleman, M. J. Smit, C. E. Hack, A. Sturk, and R. Nieuwland, "Human cell-derived microparticles promote thrombus formation in vivo in a tissue factor-dependent manner," *Journal of Thrombosis and Haemostasis,* vol. 1, pp. 2561-2568, 2003.

[21] R. J. Berckmans, R. Nieuwland, A. N. Böing, F. P. H. T. M. Romijn, C. E. Hack, and A. Sturk, "Cell-derived Microparticles Circulate in Healthy Humans and Support Low Grade Thrombin Generation,"

Thromb Haemost, vol. 85, pp. 639–646, 2001.

[22] S. Martin, A. Tesse, B. Hugel, M. C. Martinez, O. Morel, J.-M. Freyssinet, and R. Andriantsitohaina, "Shed Membrane Particles From T Lymphocytes Impair Endothelial Function and Regulate Endothelial Protein Expression," *Circulation*, vol. 109, pp. 1653-1659, April 6, 2004.

[23] S. V. Brodsky, F. Zhang, A. Nasjletti, and M. S. Goligorsky, "Endothelium-derived microparticles impair endothelial function in vitro," *Am J Physiol Heart Circ Physiol*, vol. 286, pp. H1910-1915, May 1, 2004.

[24] W. Jy, W.-W. Mao, L. L. Horstman, J. Tao, and Y. S. Ahn, "Platelet Microparticles Bind, Activate and Aggregate Neutrophils In Vitro," *Blood Cells, Molecules, and Diseases*, vol. 21, pp. 217-231, 1995.

[25] H. K. Kim, K. S. Song, J.-H. Chung, K. R. Lee, and S.-N. Lee, "Platelet microparticles induce angiogenesis in vitro," *British Journal of Haematology*, vol. 124, pp. 376-384, 2004.

[26] A. Brill, O. Dashevsky, J. Rivo, Y. Gozal, and D. Varon, "Platelet-derived microparticles induce angiogenesis and stimulate post-ischemic revascularization," *Cardiovasc Res*, vol. 67, pp. 30-38, July 1, 2005.

[27] M. Mack, A. Kleinschmidt, H. Bruhl, C. Klier, P. J. Nelson, J. Cihak, J. Plachy, M. Stangassinger, V. Erfle, and D. Schlondorff, "Transfer of the chemokine receptor CCR5 between cells by membrane-derived microparticles: A mechanism for cellular human immunodeficiency virus 1 infection," *Nat Med*, vol. 6, pp. 769-775, 2000.

[28] A. Janowska-Wieczorek, M. Wysoczynski, J. Kijowski, L. Marquez-Curtis, B. Machalinski, J. Ratajczak, and M. Z. Ratajczak, "Microvesicles derived from activated platelets induce metastasis and angiogenesis in lung cancer," *International Journal of Cancer*, vol. 113, pp. 752-760, 2005.

[29] N. Pamme, "Magnetism and microfluidics," *Lab on a Chip*, vol. 6, pp. 24-38, 2006.

[30] E. Boutsianis, T. Frauenfelder, H. Dave, J. Grunenfelder, S. Wildermuth, G. Zund, M. Turina, D. Poulikakos, and Y. Ventikos, "Cardiovascular Haemodynamic Simulations of Anatomically Accurate Coronaries," 2003.

[31] G. Chironi, C. Boulanger, A. Simon, F. Dignat-George, J.-M. Freyssinet, and A. Tedgui, "Endothelial microparticles in diseases," *Cell and Tissue Research*, vol. 335, pp. 143-151, 2009.

[32] A. E. Kamholz, B. H. Weigl, B. A. Finlayson, and P. Yager, "Quantitative Analysis of Molecular Interaction in a Microfluidic Channel: The T-Sensor," *Analytical Chemistry*, vol. 71, pp. 5340-5347, 1999.

[33] S. K. Sia and G. M. Whitesides, "Microfluidic devices fabricated in Poly(dimethylsiloxane) for biological studies," *Electrophoresis*, vol. 24, pp. 3563-3576, 2003.

[34] A. R. Wheeler, W. R. Throndset, R. J. Whelan, A. M. Leach, R. N. Zare, Y. H. Liao, K. Farrell, I. D. Manger, and A. Daridon, "Microfluidic Device for Single-Cell Analysis," *Analytical Chemistry*, vol. 75, pp. 3581-3586, 2003.

[35] P. S. Dittrich and A. Manz, "Lab-on-a-chip: microfluidics in drug discovery," *Nat Rev Drug Discov*, vol. 5, pp. 210-218, 2006.

[36] G. Piotr, G. Irina, D. Willow, M. W. George, K. Eugenia, and A. S. Howard, "Formation of monodisperse bubbles in a microfluidic flow-focusing device," *Applied Physics Letters*, vol. 85, pp. 2649-2651, 2004.

[37] P. Garstecki, M. J. Fuerstman, H. A. Stone, and G. M. Whitesides, "Formation of droplets and bubbles in a microfluidic T-junction-scaling and mechanism of break-up," *Lab on a Chip*, vol. 6, pp. 437-446, 2006.

[38] P. Couvreur and F. Puisieux, "Nano- and microparticles for the delivery of polypeptides and proteins," *Advanced Drug Delivery Reviews*, vol. 10, pp. 141-162, 1993.

[39] B. A. Buchholz, H. E. Tuazon, M. D. Kaminski, S. B. Aase, L. Nufiez, and G. F. Vandegrift, "Optimizing the coating process of organic actinide extractants on magnetically assisted chemical separation particles," *Separation and Purification Technology*, vol. 11, pp. 211-219, 1997.

[40] M. Kersaudy-Kerhoas, R. Dhariwal, and M. P. Y. Desmulliez, "Recent advances in microparticle continuous separation," *Nanobiotechnology, IET*, vol. 2, pp. 1-13, 2008.

[41] C. H. Ahn, C. Jin-Woo, G. Beaucage, J. H. Nevin, L. Jeong-Bong, A. Puntambekar, and J. Y. Lee, "Disposable smart lab on a chip for point-of-care clinical diagnostics," *Proceedings of the IEEE*, vol. 92, pp. 154-173, 2004.

[42] F. B. Myers and L. P. Lee, "Innovations in optical microfluidic technologies for point-of-care diagnostics," *Lab on a Chip*, vol. 8, pp. 2015-2031, 2008.

[43] T. J. Wang, P. Gona, M. G. Larson, G. H. Tofler, D. Levy, C. Newton-Cheh, P. F. Jacques, N. Rifai, J. Selhub, S. J. Robins, E. J. Benjamin, R. B. D'Agostino, and R. S. Vasan, "Multiple Biomarkers for the Prediction of First Major Cardiovascular Events and Death," *New England Journal of Medicine*, vol. 355, pp. 2631-2639, 2006.

[44] M. S. Pepe, R. Etzioni, Z. Feng, J. D. Potter, M. L. Thompson, M. Thornquist, M. Winget, and Y. Yasui,

"Phases of Biomarker Development for Early Detection of Cancer," *Journal of the National Cancer Institute*, vol. 93, pp. 1054-1061, July 18, 2001.

[45] M. Kersaudy-Kerhoas, R. Dhariwal, and M. P. Y. Desmulliez, "Recent advances in microparticle continuous separation," *IET Nanobiotechnology,* vol. 2, pp. 1-13, 2008.

[46] J. C. Giddings, F. J. Yang, and M. N. Myers, "Flow-field-flow fractionation: a versatile new separation method," *Science (New York, N.Y.),* vol. 193, pp. 1244-1245, 1976.

[47] J. P. Brody and P. Yager, "Diffusion-based extraction in a microfabricated device," *Sensors and Actuators A: Physical,* vol. 58, pp. 13-18, 1997.

[48] J. C. Giddings, "A System Based on Split-Flow Lateral-Transport Thin (SPLITT) Separation Cells for Rapid and Continuous Particle Fractionation," *Separation Science and Technology,* vol. 20, pp. 749-768, 1985.

[49] Y. Zhang, R. W. Barber, and D. R. Emerson, "Particle Separation in Microfluidic Devices SPLITT Fractionation and Microfluidics," *Current Analytical Chemistry,* vol. 1, pp. 345-354, 2005.

[50] S. J. Sheard, M. G. Somekh, and T. Hiller, "Non-contacting determination of carrier lifetime and surface recombination velocity using photothermal radiometry," *Materials Science and Engineering: B,* vol. 5, pp. 101-105, 1990.

[51] G. Trippa, Y. Ventikos, D. P. Taggart, and C. C. Coussios, "CFD Modeling of an Ultrasonic Separator for the Removal of Lipid Particles From Pericardial Suction Blood," *Biomedical Engineering, IEEE Transactions on,* vol. 58, pp. 282-290, 2011.

[52] F. Baldessari and J. Santiago, "Electrophoresis in nanochannels: brief review and speculation," *Journal of Nanobiotechnology,* vol. 4, p. 12, 2006.

[53] H. A. Pohl, *Dielectrophoresis the Behaviour of Neutral Matter in Nonuniform Electric Fields*. Cambrige: Cambrige University Press, 1978.

[54] M. A. M. Gijs, "Magnetic bead handling on-chip: new opportunities for analytical applications," *Microfluidics and Nanofluidics,* vol. 1, pp. 22-40, 2004.

[55] H. Tsutsui and C.-M. Ho, "Cell separation by non-inertial force fields in microfluidic systems," *Mechanics Research Communications,* vol. 36, pp. 92-103, 2009.

[56] Y. Zhang and D. R. Emerson, "Effect of flow development region and fringing magnetic force field on annular split-flow thin fractionation," *Journal of Chromatography A,* vol. 1042, pp. 137-145, 2004.

[57] I. M. Hsing, Y. Xu, and W. Zhao, "Micro- and Nano- Magnetic Particles for Applications in Biosensing," *Electroanalysis,* vol. 19, pp. 755-768, 2007.

[58] S. Miltenyi, W. Müller, W. Weichel, and A. Radbruch, "High gradient magnetic cell separation with MACS," *Cytometry,* vol. 11, pp. 231-238, 1990.

[59] Q. A. Pankhurst, J. Connolly, S. K. Jones, and J. Dobson, "Applications of magnetic nanoparticles in biomedicine," *Journal of Physics D: Applied Physics,* vol. 36, p. R167, 2003.

[60] A. E. M. Vermunt, A. A. J. M. Franken, and R. R. Beumer, "Isolation of salmonellas by immunomagnetic separation," *Journal of Applied Microbiology,* vol. 72, pp. 112-118, 1992.

[61] A. Španová, B. Rittich, D. Horák, J. Lenfeld, J. Prodělalová, J. Sučiková, and S. Štrumcová, "Immunomagnetic separation and detection of Salmonella cells using newly designed carriers," *Journal of Chromatography A,* vol. 1009, pp. 215-221, 2003.

[62] O. Olsvik, T. Popovic, E. Skjerve, K. S. Cudjoe, E. Hornes, J. Ugelstad, and M. Uhlén, "Magnetic separation techniques in diagnostic microbiology," *Clinical Microbiology Reviews,* vol. 7, pp. 43-54, January 1, 1994.

[63] E. B. Setterington and E. C. Alocilja, "Rapid electrochemical detection of polyaniline-labeled Escherichia coli O157:H7," *Biosensors and Bioelectronics,* vol. 26, pp. 2208-2214. 2011.

[64] C. H. Ahn, M. G. Allen, W. Trimmer, Y. N. Jun, and S. Erramilli, "A fully integrated micromachined magnetic particle separator," *Microelectromechanical Systems, Journal of,* vol. 5, pp. 151-158, 1996.

[65] L. Sasso, A. Ündar, and J. Zahn, "Autonomous magnetically actuated continuous flow microimmunofluorocytometry assay," *Microfluidics and Nanofluidics,* vol. 9, pp. 253-265. 2010.

[66] C. Z. Liang-Shih Fan, *Principles of Gas-Solid Flows*: Cambridge University Press, 1998.

[67] M. Jean-Philippe, G. Virginie, G. Elisabeth, and F. M. Jeffrey, "Trains of particles in finite-Reynolds-number pipe flow," *Physics of Fluids,* vol. 16, pp. 4192-4195, 2004.

[68] J. F. Edd, D. Di Carlo, K. J. Humphry, S. Koster, D. Irimia, D. A. Weitz, and M. Toner, "Controlled encapsulation of single-cells into monodisperse picolitre drops," *Lab on a Chip,* vol. 8, pp. 1262-1264, 2008.

[69] A. Russom, A. K. Gupta, S. Nagrath, D. Di Carlo, J. F. Edd, and M. Toner, "Differential inertial focusing of particles in curved low-aspect-ratio microchannels," *New journal of physics,* vol. 11, p. 75025, 2009.

[70] D. Di Carlo, D. Irimia, R. G. Tompkins, and M. Toner, "Continuous inertial focusing, ordering, and separation of particles in microchannels," *Proceedings of the National Academy of Sciences,* vol. 104,

pp. 18892-18897, 2007.
[71] J. Oakey, R. W. Applegate, E. Arellano, D. D. Carlo, S. W. Graves, and M. Toner, "Particle Focusing in Staged Inertial Microfluidic Devices for Flow Cytometry," *Analytical Chemistry,* vol. 82, pp. 3862-3867, 2010.
[72] S. C. Hur, H. T. K. Tse, and D. Di Carlo, "Sheathless inertial cell ordering for extreme throughput flow cytometry," *Lab on a Chip,* vol. 10, pp. 274-280, 2010.
[73] C. T. Crowe, M. Sommerfeld, and Y. Tsuji, *Multiphase flows with droplets and particles*: CRC Press, 1998.
[74] G. Sridhar and J. Katz, "Drag and lift forces on microscopic bubbles entrained by a vortex," *Physics of Fluids,* vol. 7, pp. 389-399, 1995.
[75] G. Segre and A. Silberberg, "Radial Particle Displacements in Poiseuille Flow of Suspensions," *Nature,* vol. 189, pp. 209-210, 1961.
[76] J.-P. Matas, J. F. Morris, Guazzelli, Eacute, and Lisabeth, "Inertial migration of rigid spherical particles in Poiseuille flow," *Journal of Fluid Mechanics,* vol. 515, pp. 171-195, 2004.
[77] P. G. Saffman, "The lift on a small sphere in a slow shear flow," *Journal of Fluid Mechanics,* vol. 22, pp. 385-400, 1965.
[78] J. A. Schonberg and E. J. Hinch, "Inertial migration of a sphere in Poiseuille flow," *Journal of Fluid Mechanics,* vol. 203, pp. 517-524, 1989.
[79] E. S. Asmolov, "Dynamics of a spherical particle in a laminar boundary layer," *Fluid Dynamics,* vol. 25, pp. 886-890, 1990.
[80] J. B. McLaughlin, "Inertial migration of a small sphere in linear shear flows," *Journal of Fluid Mechanics,* vol. 224, pp. 261-274, 1991.
[81] J. B. McLaughlin, "The lift on a small sphere in wall-bounded linear shear flows," *Journal of Fluid Mechanics,* vol. 246, pp. 249-265, 1993.
[82] E. S. Asmolov, "The inertial lift on a spherical particle in a plane Poiseuille flow at large channel Reynolds number," *Journal of Fluid Mechanics,* vol. 381, pp. 63-87, 1999.
[83] D. Di Carlo, J. F. Edd, K. J. Humphry, H. A. Stone, and M. Toner, "Particle Segregation and Dynamics in Confined Flows," *Physical Review Letters,* vol. 102, p. 094503, 2009.
[84] A. A. S. Bhagat, S. S. Kuntaegowdanahalli, and I. Papautsky, "Enhanced particle filtration in straight microchannels using shear-modulated inertial migration," *Physics of Fluids,* vol. 20, pp. 101702-4, 2008.
[85] M. Toner and D. Irimia, "Blood-on-a-chip," *Annual Review of Biomedical Engineering,* vol. 7, pp. 77-103, 2005.
[86] D. Di Carlo, D. Irimia, R. G. Tompkins, and M. Toner, "Continuous inertial focusing, ordering, and separation of particles in microchannels," *Proceedings of the National Academy of Sciences of the United States of America,* vol. 104, pp. 18892-18897, 2007.
[87] D. H. Yoon, J. B. Ha, Y. K. Bahk, T. Arakawa, S. Shoji, and J. S. Go, "Size-selective separation of micro beads by utilizing secondary flow in a curved rectangular microchannel," *Lab on a Chip,* vol. 9, pp. 87-90, 2009.
[88] X. Zhang, J. M. Cooper, P. B. Monaghan, and S. J. Haswell, "Continuous flow separation of particles within an asymmetric microfluidic device," *Lab on a Chip,* vol. 6, pp. 561-566, 2006.
[89] D. Di Carlo, J. F. Edd, D. Irimia, R. G. Tompkins, and M. Toner, "Equilibrium Separation and Filtration of Particles Using Differential Inertial Focusing," *Analytical Chemistry,* vol. 80, pp. 2204-2211, 2008.
[90] D. Di Carlo, "Inertial microfluidics," *Lab on a Chip,* vol. 9, pp. 3038-3046, 2009.
[91] A. A. S. Bhagat, S. S. Kuntaegowdanahalli, N. Kaval, C. J. Seliskar, and I. Papautsky, "Inertial microfluidics for sheath-less high-throughput flow cytometry," *Biomedical Microdevices,* vol. 12, pp. 187-195, 2010.
[92] A. A. S. Bhagat, S. S. Kuntaegowdanahalli, and I. Papautsky, "Continuous particle separation in spiral microchannels using dean flows and differential migration," *Lab on a Chip,* vol. 8, pp. 1906-1914, 2008.
[93] S. S. Kuntaegowdanahalli, A. A. S. Bhagat, G. Kumar, and I. Papautsky, "Inertial microfluidics for continuous particle separation in spiral microchannels," *Lab on a Chip,* vol. 9, pp. 2973-2980, 2009.
[94] R. Aman, K. G. Amit, N. Sunitha, C. Dino Di, F. E. Jon, and T. Mehmet, "Differential inertial focusing of particles in curved low-aspect-ratio microchannels," *New Journal of Physics,* vol. 11, p. 075025, 2009.
[95] H. J. D. Vriend, "Velocity redistribution in curved rectangular channels," *Journal of Fluid Mechanics,* vol. 107, pp. 423-439, 1981.
[96] W. R. Dean, "Fluid Motion in a Curved Channel," *Proceedings of the Royal Society of London. Series A, Containing Papers of a Mathematical and Physical Character,* vol. 121, pp. 402-420, 1928.
[97] D. J. McConalogue and R. S. Srivastava, "Motion of a Fluid in a Curved Tube," *Proceedings of the*

Royal Society of London. Series A, Mathematical and Physical Sciences, vol. 307, pp. 37-53, 1968.
[98] S. A. Berger, L. Talbot, and L. S. Yao, "Flow in curved pipes," *Annual Review of Fluid Mechanics,* vol. 15, pp. 461-512, 1983.
[99] W. H. Reid, "On the Stability of Viscous Flow in a Curved Channel," *Proceedings of the Royal Society of London. Series A. Mathematical and Physical Sciences,* vol. 244, pp. 186-198, March 11, 1958.
[100] D. B. Brewster, P. Grosberg, and A. H. Nissan, "The Stability of Viscous Flow between Horizontal Concentric Cylinders," *Proceedings of the Royal Society of London. Series A. Mathematical and Physical Sciences,* vol. 251, pp. 76-91, May 12, 1959.
[101] S. Sugiyama, T. Hayashi, and K. Yamazaki, "Flow characteristics in the curved rectangular channels (visualization of secondary flow)," *Bulletin of the Jsme-Japan Society of Mechanical Engineers,* vol. 26, pp. 964-969, 1983.
[102] B. Bara, K. Nandakumar, and J. H. Masliyah, "An experimental and numerical study of the Dean problem: flow development towards two-dimensional multiple solutions," *Journal of Fluid Mechanics,* vol. 244, pp. 339-376, 1992.
[103] S. Kim and S. J. Lee, "Measurement of Dean flow in a curved micro-tube using micro digital holographic particle tracking velocimetry," *Experiments in Fluids,* vol. 46, pp. 255-264, 2009.
[104] H. Fellouah, C. Castelain, A. Ould El Moctar, and H. Peerhossaini, "A criterion for detection of the onset of Dean instability in Newtonian fluids," *European Journal of Mechanics - B/Fluids,* vol. 25, pp. 505-531, 2006.
[105] K. C. Cheng, R. C. Lin, and J. W. Ou, "Fully developed laminar-flow in curved rectangular channels," *Journal of Fluids Engineering-Transactions of the Asme,* vol. 98, pp. 41-48, 1976.
[106] T. T. Chandratilleke and Nursubyakto, "Numerical prediction of secondary flow and convective heat transfer in externally heated curved rectangular ducts," *International Journal of Thermal Sciences,* vol. 42, pp. 187-198, 2003.
[107] L. Helin, L. Thais, and G. Mompean, "Numerical simulation of viscoelastic Dean vortices in a curved duct," *Journal of Non-Newtonian Fluid Mechanics,* vol. 156, pp. 84-94, 2009.
[108] M. Boutabaa, L. Helin, G. Mompean, and L. Thais, "Numerical study of Dean vortices in developing Newtonian and viscoelastic flows through a curved duct of square cross-section," *Comptes Rendus Mecanique,* vol. 337, pp. 40-47, 2009.
[109] H. Fellouah, C. Castelain, A. O. E. Moctar, and H. Peerhossaini, "A Numerical Study of Dean Instability in Non-Newtonian Fluids," *Journal of Fluids Engineering,* vol. 128, pp. 34-41, 2006.
[110] H. Fellouah, C. Castelain, A. O. El Moctar, and H. Peerhossaini, "Detection of the onset of Dean instability and effects of the rheological behaviour in non-Newotonian fluids," *Journal of Physics: Conference Series*. vol. 137, pp. 12023-12023. 2008
[111] K. C. Cheng and M. Akiyama, "Laminar forced convection heat transfer in curved rectangular channels," *International Journal of Heat and Mass Transfer,* vol. 13, pp. 471-490, 1970.
[112] H. K. Moffatt, "Viscous and resistive eddies near a sharp corner," *Journal of Fluid Mechanics,* vol. 18, pp. 1-18, 1964.
[113] J. A. Baylis, "Experiments on laminar flow in curved channels of square section," *Journal of Fluid Mechanics,* vol. 48, pp. 417-422, 1971.
[114] Y. Mori, Y. Uchida, and T. Ukon, "Forced convective heat transfer in a curved channel with a square cross section," *International Journal of Heat and Mass Transfer,* vol. 14, pp. 1787-1805, 1971.
[115] J. A. C. Humphrey, A. M. K. Taylor, and J. H. Whitelaw, "Laminar flow in a square duct of strong curvature," *Journal of Fluid Mechanics,* vol. 83, pp. 509-527, 1977.
[116] P. Hille, R. Vehrenkamp, and E. O. Schulz-Dubois, "The development and structure of primary and secondary flow in a curved square duct," *Journal of Fluid Mechanics,* vol. 151, pp. 219-241, 1985.
[117] P. M. Ligrani and R. D. Niver, "Flow visualization of Dean vortices in a curved channel with 40 to 1 aspect ratio," *Physics of Fluids,* vol. 31, pp. 3605-3617, 1988.
[118] B. Joseph, E. P. Smith, and R. J. Adler, "Numerical treatment of laminar flow in helically coiled tubes of square cross section. Part I. Stationary helically coiled tubes," *AIChE Journal,* vol. 21, pp. 965-974, 1975.
[119] S. Thangam and N. Hur, "Laminar secondary flows in curved rectangular ducts," *Journal of Fluid Mechanics,* vol. 217, pp. 421-440, 1990.
[120] M. J. Targett, W. B. Retallick, and S. W. Churchill, "Flow through curved rectangular channels of large aspect ratio," *Aiche Journal,* vol. 41, pp. 1061-1070, 1995.
[121] W. H. Finlay, J. B. Keller, and J. H. Ferziger, "Instability and transition in curved channel flow," *Journal of Fluid Mechanics,* vol. 194, pp. 417-456, 1988.
[122] Y. Zhang and J. M. Reese, "The drag force in two-fluid models of gas-solid flows," *Chemical Engineering Science,* vol. 58, pp. 1641-1644, 2003.
[123] M. Ishii and K. Mishima, "Two-fluid model and hydrodynamic constitutive relations," *Nuclear*

Engineering and Design, vol. 82, pp. 107-126, 1984.
[124] J. K. Dukowicz, "Particle-fluid numerical model for liquid sprays," *Journal Name: J. Comput. Phys.; (United States); Journal Volume: 35:1*, pp. Medium: X; Size: Pages: 229-253, 1980.
[125] C. Meneveau, T. S. Lund, and W. H. Cabot, "A Lagrangian dynamic subgrid-scale model of turbulence," *Journal of Fluid Mechanics*, vol. 319, pp. 353-385, 1996.
[126] B. H. Xu and A. B. Yu, "Numerical simulation of the gas-solid flow in a fluidized bed by combining discrete particle method with computational fluid dynamics," *Chemical Engineering Science*, vol. 52, pp. 2785-2809, 1997.
[127] H. Nirschl, H. A. Dwyer, and V. Denk, "Three-dimensional calculations of the simple shear flow around a single particle between two moving walls," *Journal of Fluid Mechanics*, vol. 283, pp. 273-285, 1995.
[128] F. Brezzi, J.-L. Lions, and O. Pironneau, "Analysis of a Chimera method," *Comptes Rendus de l'Académie des Sciences - Series I - Mathematics*, vol. 332, pp. 655-660, 2001.
[129] H. H. Hu, N. A. Patankar, and M. Y. Zhu, "Direct numerical simulations of fluid - solid systems using the arbitrary Lagrangian–Eulerian technique," *Journal of Computational Physics*, vol. 169, pp. 427-462, 2001.
[130] R. Glowinski, T. W. Pan, T. I. Hesla, and D. D. Joseph, "A distributed Lagrange multiplier/fictitious domain method for particulate flows," *International Journal of Multiphase Flow*, vol. 25, pp. 755-794, 1999.
[131] C. S. Peskin, "The immersed boundary method," *Acta Numerica*, vol. 11, pp. 479-517, 2002.
[132] J. Kim, D. Kim, and H. Choi, "An Immersed-Boundary Finite-Volume Method for Simulations of Flow in Complex Geometries," *Journal of Computational Physics*, vol. 171, pp. 132-150, 2001.
[133] K. Höfler and S. Schwarzer, "Navier-Stokes simulation with constraint forces: Finite-difference method for particle-laden flows and complex geometries," *Physical Review E*, vol. 61, pp. 7146-7160, 2000.
[134] M. R. Maxey and B. K. Patel, "Localized force representations for particles sedimenting in Stokes flow," *International Journal of Multiphase Flow*, vol. 27, pp. 1603-1626, 2001.
[135] G. Houzeaux and R. Codina, "An iteration-by-subdomain overlapping Dirichlet/Robin domain decomposition method for advection - diffusion problems," *Journal of Computational and Applied Mathematics*, vol. 158, pp. 243-276, 2003.
[136] J. H. Ferziger and M. Perić, *Computational methods for fluid dynamics*. Berlin: Springer-Verlag, 2002.
[137] J. Anderson, *Computational fluid dynamics: The Basics with Applications*. New York: McGraw-Hill, 1995.
[138] P. M. Ferziger JH, *Computational methods for fluid dynamics*. New York: Springer-Verlag, 2002.
[139] "CFD-ACE+ V20011.0 User Manual."
[140] V. Kurtcuoglu, D. Poulikakos, and Y. Ventikos, "Computational Modeling of the Mechanical Behaviour of the Cerebrospinal Fluid System," *Journal of Biomechanical Engineering*, vol. 127, pp. 264-269, 2005.
[141] R. Clift, J. R. Grace, and M. E. Weber, *Bubbles, drops, and particles*: Academic Press, 1978.
[142] H. H. Hu, D. D. Joseph, and M. J. Crochet, "Direct simulation of fluid particle motions," *Theoretical and Computational Fluid Dynamics*, vol. 3, pp. 285-306, 1992.
[143] L. S. Fan and C. Zhu, *Principles of gas-solid flows*, 1999.
[144] T. M. Squires and S. R. Quake, "Microfluidics: Fluid physics at the nanoliter scale," *Reviews of Modern Physics*, vol. 77, p. 977, 2005.
[145] R. J. Gibbs, M. D. Matthews, and D. A. Link, "The relationship between sphere size and settling velocity," *Journal of Sedimentary Research*, vol. 41, pp. 7-18, March 1, 1971.
[146] W. Chester, "On Oseen's approximation," *Journal of Fluid Mechanics*, vol. 13, pp. 557-569, 1962.
[147] A. t. Cate, C. H. Nieuwstad, J. J. Derksen, and H. E. A. V. d. Akker, "Particle imaging velocimetry experiments and lattice-Boltzmann simulations on a single sphere settling under gravity," *Physics of Fluids*, vol. 14, pp. 4012-4025, 2002.
[148] A. F. Fortes, D. D. Joseph, and T. S. Lundgren, "Nonlinear mechanics of fluidization of beds of spherical particles," *Journal of Fluid Mechanics*, vol. 177, pp. 467-483, 1987.
[149] J. B. Knight, A. Vishwanath, J. P. Brody, and R. H. Austin, "Hydrodynamic Focusing on a Silicon Chip: Mixing Nanoliters in Microseconds," *Physical Review Letters*, vol. 80, pp. 3863-3866, 1998.

List of Publications & Training

Journal Publications

1. Wang, C., Chou, D. and Ventikos, Y., A Computationally Efficient Multiscale Lagrangian-Eulerian Method for Flows with Arbitrary Sized Particles in Complex Geometries: Application in Microfluidic Channels. Microfluidics and Nanofluidics, Submitted, 2013.
2. Wang, C., and Ventikos, Y., Size-based particle separation by curved microchannels. New Journal of Physics, Submitted, 2013.

Conference Publications

1. Wang, C., and Ventikos, Y., Highly-curved microchannel for particle separation, 6th IEEE EMBS UK & Republic of Ireland Postgraduate Conference on Biomedical Engineering and Medical Physics (Glasgow, UK), 2011.
2. Wang, C., Chou D., Ventikos, Y., Microfluidics in curved channels for particle separation. NanoBio Tech (Montreux, Switzerland), 2012.

Patents

1. Wang, C., and Ventikos, Y., Bioparticle separation, immunomagnetic separation and microfluidic diagnostic (POC) system, to be filed.

Seminars and Training

Demonstrator Training course. Department of Engineering Science. 2009.
Library Skills Training course. Radcliffe Science Library. 2009.
Purely-elastic flow instabilities in extensional flows. Chemical Engineering Seminar. 2009.
Introduction to Tutorial Teaching. Department of Engineering Science. 2009.
Linux (all 3 sessions): Introduction, Using office programs and email, Command line. OUCS. 2010.
E-books searching and reading. OUCS. 2010.
Programming: C++ introduction (all 3 sessions). 2010.
Transnational Entrepreneurship. ISIS. 2010.
Sustainable Energy. Department of Engineering Science. 2010.
Managing Your Dphil. MPLS. 2010.
From model organisms to environmental applications. Chemical Engineering Seminar. 2010.
Introduction to MATLAB and Graphic User Interfaces. OUCS. 2010.
Superparamagnetic Nanoparticles for Drug Delivery. Chemical Engineering Seminar. 2010.
Academic Writing (weekly). Language Centre. 2010-2011.
How I got into the mitochondrion (Sir John Walker). Nobel Prize Seminar. 2011.
Science Innovation Plus Program (one year, completed full program and obtained certificate). Saïd Business School, University of Oxford. 2010-2011.
Developing affordable healthcare technology. The Centre for Affordable Healthcare Technologies. 2012.

Appendix I

Appendix I is not available for consultation until 1st May 2033.